Experimental Quantification of H_2/CH_4 Mixture Relative Permeability

SET: Master End Project

Jeronimo Lira

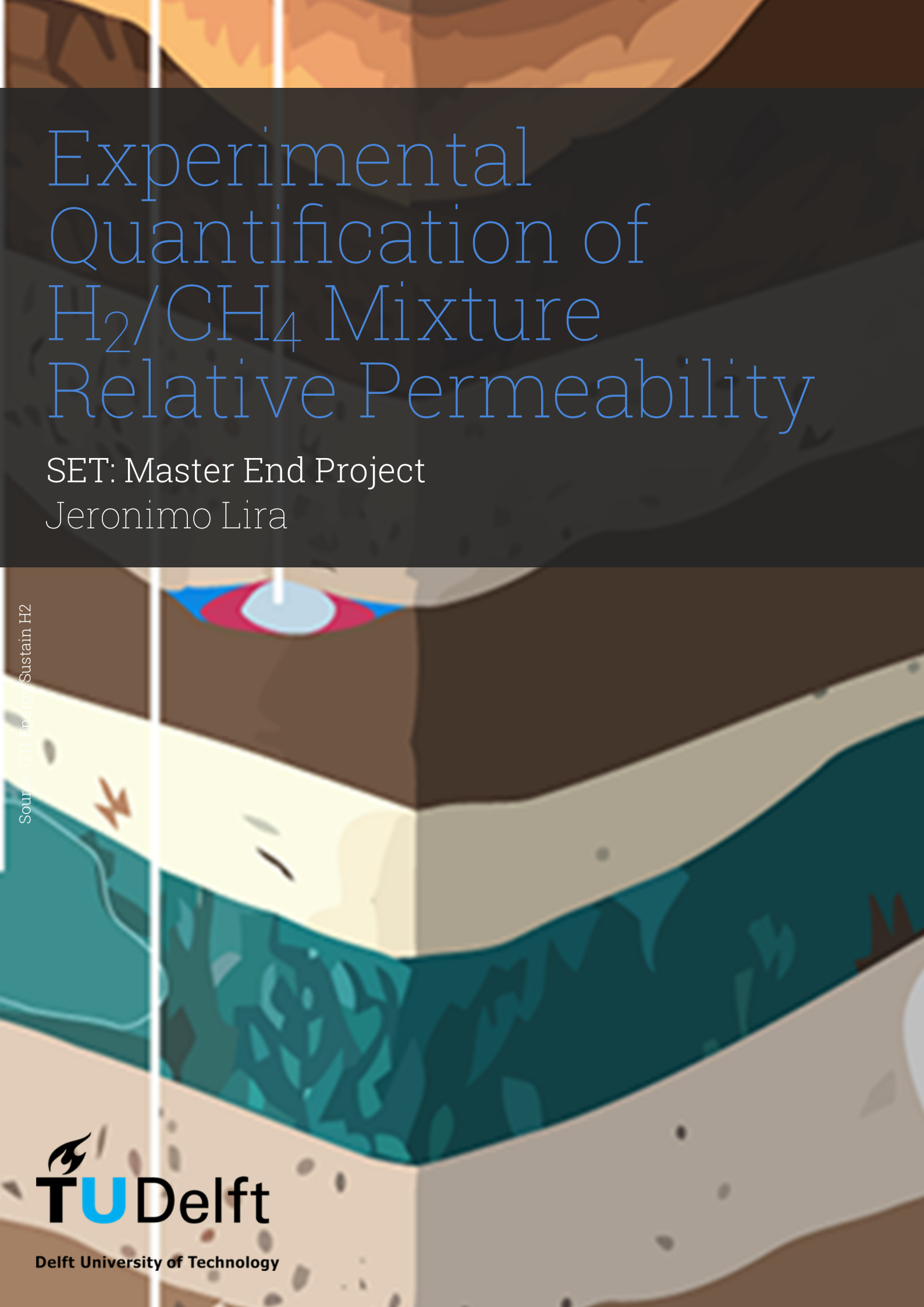

Source: GTI Energy Sustain H2

TU Delft

Delft University of Technology

Experimental Quantification of H_2/CH_4 Mixture Relative Permeability

by

Jeronimo Lira

to obtain the degree of Master of Science
at the Delft University of Technology,
to be defended publicly on 15_{th} January.

Student number:	5302951	
Project duration:	December 2024 - January 2026	
Supervisors:	Willemijn van Rooijen	TU Delft, Daily supervisor
	Dr. M.Naderloo	TU Delft, Daily supervisor
	Dr. S.A.Jones	TU Delft, Technical supervisor
	Michiel Slob	TU Delft, Technical supervisor
	Prof. Dr. H. Hajibeygi	TU Delft, Main supervisor
Advisor:	Dr. C.m. van der Graaf	TU Delft
Thesis Committee:	Prof. Dr. H. Hajibeygi	TU Delft
	Prof. Dr. M. Bloemendal	TU Delft
	Dr. R. Farajzadeh	TU Delft

TU Delft
Delft University of Technology

Preface

This thesis is the conclusion of my master studies in Sustainable Energy Technology, during which I have had the pleasure to work with many talented, kind, and ambitious fellow students. This thesis has proved to be a challenging endeavor, and reminded me once more that simple ideas are often not simple to execute. What started as experimental research to support modeling data, soon became the sole focus of this work. Whether due to hiccups in the lab, lost code, or missing data, there was always a new challenge awaiting me. While I overcame some on my own, I certainly could not have done it without the tremendous team who supported me in every step of the journey, and I would like to express my sincere gratitude to each of you.

Firstly, I would like to thank Willemijn van Rooijen, who never hesitated to reach out and always made time to thoughtfully reply to my problems. Truly dependable, simply knowing you were one message away was extremely reassuring when I was in doubt. I would also like to thank Milad Naderloo, who among many other things guided me throughout the stages leading to the experiment, and visited the lab to check on how things were progressing, ready to lend a hand of help. I would further like to thank Sian Jones and Michiel Slob for their assistance, insight, and practical support during the preparation and execution of the experiment. Michiel your assistance was immeasurable, and Sian, the occasional marshmallows, brownies, and cookies made long days in the lab all the more worth it. I could not move on without thanking Hadi Hajibeygi, who offered me this tremendous opportunity, and provided critical feedback when I needed it most. You have assembled a wonderful team of people, who I have enjoyed learning from and getting to know these past few months. I would also like to thank you for inviting me to the meetings, summer school, and talks, which filled me with insight and optimism into the multifaceted challenge of the energy transition.

Finally, I want to thank my family for their unconditional support, patience, and curiosity in my research. They have helped me in too many ways to express.

Abstract

Underground hydrogen storage (UHS) in porous media is expected to play a key role in enabling large scale, long duration energy storage for renewable energy systems. The feasibility of UHS in depleted gas reservoirs depends strongly on multiphase flow behavior and gas trapping during injection and withdrawal cycles. This study experimentally investigates the co - flow of hydrogen, methane, and a 50–50% molar hydrogen methane mixture with 1 % w.t NaCl brine in a Berea sandstone core under UHS relevant conditions. Steady state horizontal core flooding experiments at 18 °C and 100 bar, combined with medical X-ray CT imaging, were used to determine relative permeability (kr) and capillary pressure (Pc) during drainage and imbibition cycles. The results showed that hydrogen exhibited slightly higher kr than methane during drainage, with near end point kr values of 0.0399 and 0.0233, respectively, at a gas fractional flow (f_g) $f_g = 0.99$, reflecting hydrogen's lower viscosity and higher mobility. During imbibition, both methane and the mixture showed marginally higher kr than hydrogen, indicating improved producibility. The mixture displayed intermediate behavior: at $f_g = 0.8$ the mixture's drainage (kr=0.0022) and imbibition 2 (kr=0.0015) kr values, and Pc (Pc = 0.18–0.41 bar) fell between those of hydrogen (kr = 0.0014 , Pc = 0.22–0.40 bar) and methane (kr = 0.0016, Pc = 0.14–0.33 bar). Hydrogen showed greater hysteresis than either methane or the mixture, with linear trapping coefficients (A) of 0.66–0.459 versus 0.62–0.35 for methane, and 0.15 for the mixture across successive drainage/imbibition cycles. The lower mixture hysteresis suggests higher recovery efficiency than hydrogen gas. The experimentally derived kr and Pc data provide valuable input for UHS modeling, reservoir simulation, and injection/withdrawal optimization. This study concludes that mixtures of hydrogen and methane will not exhibit significantly different kr/Pc under relevant UHS conditions, and simulations may treat the mixed systems similarly to the pure systems. However, experimental errors (including the potential for trapped residue gas from previous gas type experiments in the core) make conclusions from these outcomes problematic and future studies may be required to verify the results.

Contents

Nomenclature

Abbreviations

Abbreviation	Definition
CT	Computed Tomography
GHG	Greenhouse Gas
TWh	Terawatt hour
UHS	Underground Hydrogen Storage
DP	Differential Pressure

Symbols

Symbol	Definition	Unit
A	Cross-sectional area (relative permeability)	[m^2]
A (trapping)	Linear trapping coefficient	[-]
Ca	Capillary number	[-]
f_g	Fractional flow of gas	[-]
M	Viscosity ratio	[-]
K	Absolute permeability	[m^2]
k_r	Relative permeability	[-]
L	Length	[m]
P	Pressure	[Pa]
Pc	Capillary pressure	[Pa]
Q	Flow rate	[m^3/s]
S	Saturation	[-]
S_{gi}	Initial gas saturation	[-]
S_{gr}	Residual gas saturation	[-]
S_w	Water/brine saturation	[-]
S_{wi}	Irreducible water/brine saturation	[-]
CH_4	Methane	
H_2	Hydrogen	
P1	Inlet Pressure	[-]
P2	outlet pressure	[-]
DP3	Differential Pressure transducer measurement at 0 - 21.5 mm	[-]
DP4	Differential Pressure transducer measurement at 21.5 - 147.5 mm	[-]
DP5	Differential Pressure transducer measurement at 147.5 - 170 mm	[-]
μ	Viscosity	[Pa·s]
σ	Interfacial tension	[N/m]
ϕ	Porosity	[-]

List of Figures

List of Tables

1 Introduction

Current global energy systems have caused adverse effects on the environment and accelerated climate change, with 2024 marking the hottest year on record, at approximately 1.55°C above pre-industrial levels [1]. The power sector remains the largest source (26%) of greenhouse gas (GHG) emissions [1], requiring the reduction of conventional energy sources that emit GHG emissions, while increasing the need for sustainable energy systems. Consequently, renewable energy sources are increasingly being adopted worldwide to mitigate the effects of climate change and limit global warming to an average of 1.5° C above pre-industrial levels by 2050 [2, 3] as outlined in the paris agreement. In recent years, renewable energy has become a major electricity source in many European countries [3–5]. However, renewable energy sources (RES), such as solar and wind, are inherently weather dependent and intermittent, leading to fluctuations in supply [3]. These fluctuations cause substantial mismatches between supply and demand, especially due to seasonal variations [6–8]. Thus, large scale implementation of renewable energy systems necessitates effective energy storage solutions [8]. Even so, in a successful future energy market where a significant part of the energy demand is produced by RES, the energy mix will need to consist of a large part of liquid and gaseous energy carriers for transport and storage of energy [9]. Furthermore, energy intensive sectors such as shipping, aviation, and chemical processing, are difficult to electrify, as electricity and battery based energy supply alone is insufficient, requiring alternative technologies to achieve full decarbinization [2, 3]. Hence, it is of societal and economical relevance to find an adequate energy storage medium, in order to create a balanced energy system.

In this context, hydrogen (H_2) has gained significant attention as a clean energy carrier that can support the clean energy transition and reduce dependence on fossil fuels [10–12]. It has a high mass energy density (over 200 times the volumetric energy density of pumped hydro storage, and 50 times that of compressed air), is lightweight, and importantely, can emit zero carbon emissions when used for energy functions [9]. Additionally, hydrogen is versatile across multiple sectors beyond power generation, where it can serve various applications: fuel cells, industrial feedstock, residential heating, power generation, and storage and transport systems [8, 13–15].

Hydrogen can be distinguished based on its conversion process; the most suitable in a climate sense are green and white hydrogen, while the vast majority of the current hydrogen supply is made from gray or black hydrogen, involving methane gas (CH_4) or coal gassification, respectively [16]. Gray an black hydrogen are suboptimal in terms of climate impact, as they emit vasts amounts of GHG (10-19 tons of CO_{2eq} per ton of H_2 and 22-26 kg CO_{2eq} per kg H_2, respectively) [17]. White hydrogen on the other hand is naturally occurring, and generated within the Earth crust through interactions between water molecules and iron rich minerals at high temperatures and pressure [16]. While current estimates suggest that even a small portion of the current estimated underground hydrogen could meet the global hydrogen demand for around 200 years, projects are still in the development phase, and no current technologies exist to extract it [16, 18]. Green hydrogen, involves converting (excess) renewable electricity to hydrogen via electrolysis, which crucially does not emit additional GHG, often by converting excess electrical energy that the grid cannot otherwise support into molecular form [8, 16]. Figure1.3 shows the main conversion pathways. Power-to-gas uses electricity to make hydrogen

or synthetic methane for storage, supporting sector coupling. Gas-to-gas produces hydrogen from natural gas via steam methane reformation with carbon capture and storage, to reduce emissions, while power-to-power specifically stores electrical energy in the form of hydrogen, which is later reconverted to electricity through fuel cells or gas turbines [9].

However, to fully integrate hydrogen into the global energy system, suitable and scalable storage solutions will be essential [19]. In Europe alone, hydrogen storage demand is projected to range between 63 and 180 billion m^3 [20], while global demand may increase from 95 Mt in 2022 to 430 Mt by 2050 [21]. These volumes far exceed the capacity of current surface based hydrogen storage facilities [22].

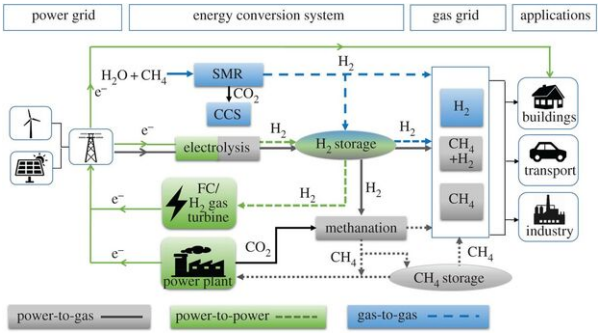

Figure 1.1: Schematic diagram showing the three main energy conversion pathways in a renewable energy integrated energy system. source: Brandon et al. [9]

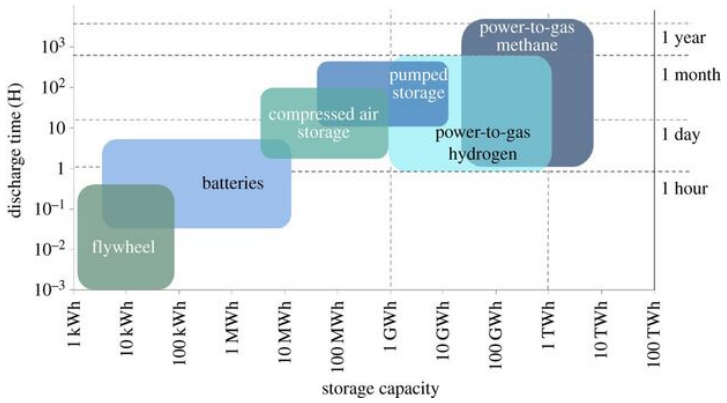

Figure 1.2: Energy storage vs discharge time for different storage types. Source: Brandon et al. [9]

Subsurface geological formations offer the seasonal (TWh scale) storage volumes required to buffer supply fluctuations from renewable energy [8, 23] (see Figure1.2 for a comparison of energy storage capacities of storage technologies). This concept is known as Underground Hydrogen Storage (UHS). UHS can generally be categorized into two types: (i) cavern storage in excavated or solution mined cavities in salt or rock, and (ii) storage in porous media, such as in the pore space of sandstone or carbonate formations [2, 3].

Salt caverns are geographically restricted to evaporitic formations and typically provide smaller storage volumes ranging from 150,000 to 800,000 m^3, making them more suitable for short to medium term storage at the GWh scale [8, 23]. In contrast, porous subsurface formations, such as reservoirs, offer storage capacities several orders of magnitude greater (100 GWH - several TWH), are more geographically widespread, and have successfully stored gases such as methane, air, and carbon dioxide (CO_2) in past operations [8, 23, 24]. Among these, depleted gas reservoirs are particularly promising for UHS, as they satisfy key storage criteria, including (1) large capacity, (2) high permeability, and (3) well defined structural traps [3, 25]. Moreover, depleted gas reservoirs contain residual gas that can serve as cushion gas, and have pre existing surface and subsurface infrastructure, reducing capital costs [8, 26, 27]. According to Sadkhan et al. [25], the capital expenditure per kilogram of H_2 is estimated at \$1.23 in depleted gas reservoirs, compared to \$1.29 in aquifers, \$1.61 in salt caverns, and \$2.77 in hard rock caverns.

In the Netherlands, TNO and EBN [28] investigated underground energy storage potential for hydrogen, finding the technical potential for UHS is large: 43.3 TWh in caverns, and 277 TWh in depleted gas fields. They reported that a total working volume of 93 billion m^3 in onshore, and 60 billion m^3 in offshore gas fields is potentially available for cyclic hydrogen gas storage. 14.5 billion m^3 of hydrogen gas working volume could be available in 321 onshore underground salt caverns. However, the development of this number of salt caverns will most likely be opposed by significant political and social resistance. Hence, the working gas volumes in Dutch salt caverns by 2050 could be closer to 5 billion m^3. At the same time, the report projected the hydrogen storage demand by 2050 (in the Netherlands) to be between 1 and 10 billion m^3, implying that salt caverns alone may be insufficient and storage in depleted gas reservoirs would be required.

Historically, field operations have stored town gas (a mixture of 20–60% hydrogen and 10–33% methane) [29]. Although no aquifer projects currently store pure hydrogen, Underground Gas Storage (UGS) of town gas has been implemented in Ketzin (Germany), Lobodice (Czech Republic), and Beynes (France) [30]. More recently, projects such as HyChico [31], Underground Sun Storage [32], and HyUsPRe [33] have further explored gas storage in depleted reservoirs with mixtures containing up to 10% hydrogen [29]. Experience from these operations has long shown that storage of mild hydrogen and natural gas blends can be safely done without adverse effects to the reservoir, installations and the environment. However, not all hydrogen could be recovered due to processes such as diffusion, dissolution and bacterial conversion to methane [34]. Moreover, many unknowns remain in the context of UHS: the influence of different types of rock formations, fluids and microorganisms in reservoirs on UHS performance, and the associated risks, are still being investigated [34].

Moreover, the operation of UHS differs significantly from traditional UGS due to more frequent and irregular injection/production cycles, dictated by renewable energy availability [13, 24]. Hydrogen's unique properties such as low density, viscosity, and molecular weight, lead to distinct flow behaviors under subsurface conditions (e.g. pressure, temperature, salinity) [3, 8]. Moreover, hysteresis may result in hydrogen trapping, which can degrade system performance [20, 35]. These dynamics involve complex interactions of gravitational, viscous, and capillary forces, yielding flow patterns distinct from those of natural gas or CO_2 storage in which there is more experience [24].

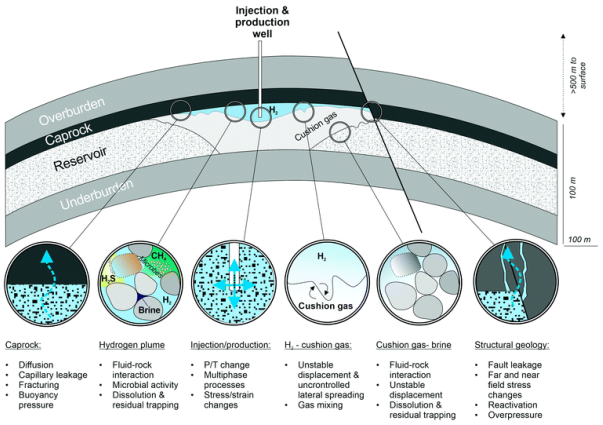

Figure 1.3: Challenges and uncertainties UHS. Source: Heinemann et al. [8]

Many factors can effect UHS, of which a few are presented in Figure1.3. Although these challenges around UHS operations are important to address, this thesis focuses on hydrogen mixing with cushion gas in depleted natural gas reservoirs. Cushion gas is defined as the volume of gas which is not produced and therefore remaining in the storage medium [36], and gases such as N^2, CH^4, or $CO-2$, are required to maintain reservoir pressure as hydrogen is withdrawn [37]. Cushion gas can accompany hydrogen that is being produced from wells, affecting the purity of the resulting hydrogen outflow [38]. Methane, the primary constituent of natural gas, and its abundance in deleted gas reservoirs is considered a viable candidate for cushion gas [2, 37]. Moreover, mixing may effect pertinent parameters in UHS that control the fluid flow, such as viscosity, density, surface tension, and wettability [2, 39–41], as wel as the fact that mixing may lead to an irreversible loss of hydrogen [36]. Thus, understanding the mixing of hydrogen and natural gas and multiphase fluids (the gas mixture and formation brine) is of

importance to designing and understanding UHS systems.

A foundational step in characterizing fluid flow through porous media is to measure key multiphase flow parameters, namely relative permeability (kr) and capillary pressure (Pc), which are essential for reservoir simulations to model UHS operation [42, 43]. While several studies have characterized these parameters for both the methane (CH_4) and hydrogen (H_2) brine/rock system under relevant conditions (1–100 bar, 18–80 ° C) [20, 24, 35, 43–46], there remains limited investigation in literature into the flow behavior of hydrogen/methane mixtures in depleted gas fields, leaving a crucial gap in knowledge relevant to understanding and adequate modeling of UHS in such formations.

Therefore, this study aims to experimentally determine the relative permeability and capillary pressure curves of the hydrogen/methane/brine/rock system under UHS relevant conditions to provide more robust data to support modeling endeavors for optimal reservoir operation. A horizontal core flood experiment is performed on a brine saturated Berea sandstone core (17 cm long, 3.8 cm diameter) at 18 °C and 100 bar, using a medical X-ray computed tomography (CT) scanner to visualize saturation profiles. Measurements are taken at steady state pressure gradients under varying gas saturations by controlling fractional flow.

1.1. Objectives and main Research Question

The objective of this thesis is to contribute to filling the knowledge gap of hydrogen/methane mixtures relative permeability and capillary pressure at conditions relevant to UHS that currently exists in the literature. This may progress development of UHS in depleted gas reservoirs by developing more robust and potentially more accurate data for use in reservoir simulations.

The main research question for this thesis is then:

- How does the composition of hydrogen/methane gas effect the relative permeability and capillary pressure of gas in UHS?

1.1.1. Research Approach

In order for the main research question to be answered in this thesis, a sound research approach is required. A first step is to understand which parameters may influence the relative permeability and capillary pressure, and what is to be expected of the behavior of hydrogen/methane mixtures given literature on the pure hydrogen/methane/brine/rock systems. This leads to the following sub research questions:

- How do external operating conditions (temperature, pressure, and rock mineralogy) influence the relative permeability and capillary pressure of H, CH, and their mixtures?
- How do intrinsic fluid properties (interfacial tension, viscosity, density, diffusivity, solubility) affect the relative permeability and capillary pressure behavior of H, CH, and their mixtures in water/brine saturated porous media?

1.2. Report Outline

Following the introduction, the report presents the theoretical background relevant to relative permeability and capillary pressure, along with an overview of the key factors that directly impact these properties, in section 2. This is followed by a review of previous studies, summarizing existing relevant research on hydrogen and methane relative permeability and capillary pressure in gas/brine/rock systems outlining the implications these findings may have for the behavior of their mixtures at the experimental conditions of this study. The experimental procedure is outlined and explained in section 3. Section 4 presents the results and discusses them in relation to insights from the literature. Finally, the report concludes with a chapter outlining the main findings, identifying sources of uncertainty, and providing recommendations for future work.

2

Literature Review and Theory

Due to the differing physicochemical properties of H_2 compared to CH_4, mixtures may introduce additional complexity compared to traditional storage and UHS in porous media. In this section, an overview of relative permeability and capillary pressure is given, along with a discussion of factors that might significantly effect these multiphase flow parameters, including the wettability, viscosity, mobility, and surface tension. The relevant literature is then evaluated to give potential indications of how the H_2/CH_4 mixture kr an Pc may differ in comparison to pure H_2 and pure CH_4 in porous media under relevant UHS conditions.

2.1. Relative Permeability and Capillary Pressure – Overview

Relative permeability (kr) is the ratio of effective permeability (the permeability of one fluid in the presence of other fluids) to the absolute permeability (intrinsic to the porous media) [47]. It can be described by the extended Darcy's the law:

$$q_i = -\frac{K \cdot k_{ri} \cdot \Delta P}{\mu_i \cdot L} \tag{2.1}$$

Where, q_i is the flow rate of phase i, K is the absolute permeability of the porous media with respect to water, k_{ri} is the relative permeability of phase i, ΔP is the pressure drop across length L in the medium, and μ_i is the viscosity of phase i.

It can also be interpreted as the capacity of one phase to flow in respect to the other normalized by the absolute permeability [47]. While the absolute permeability is usually considered a constant (a function solely determined by the material alone), the relative permeability varies depending on the quantity of the other phase in the material, and is therefore a function of saturation.

The saturation profile across the length of a porous sample may differ due to heterogeneity within the material, and result in different saturations being observed during drainage (reducing the wetting phase saturation) and imbibition (increasing the wetting phase saturation). This can be explained by the fact that different phases move differently through porous media. When one phase forces the other out, the saturation distribution changes in the medium, which effects the phases capacity to flow, resulting in a process that is not precisely reversible [47]. Hence, kr is not only a function of Sw, though also of the previous state of the system. This phenomena, called hysteresis, is crucial to consider in relative permeability tests and UHS simulations [48].

Notably, the practical range of saturations that are attainable never reach one or zero [49]. Rather the range lies between a critical saturation for each phase. In multiphase phase flow, the subscripts n and w can describe the wetting and non-wetting phases respectively. The irreducible (S_{wi}) and the maximum saturation (S_{wmax}) represent the minium and the maximum wetting phase saturation that

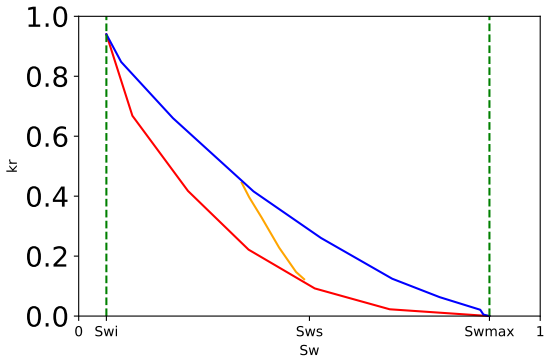

Figure 2.1: Generic Drainage/Imbibition curve for relative permeability. Imbibition (Red), Drainage (Blue), and scanning curve (Orange). The curves go beyond S_{wmax} and the S_{wi} illustrate values the lines would obtain theoretically, if there was no trapping of fluid, adapted from [47]

.

can be obtained, while the residual saturation (Sr) represents the minimum non-wetting saturation after imbibition [49].

Figure2.1 shows a typical drainage/imbibition curve, with respect to the wetting phase saturation for non-wetting phase. The hysteresis between imbibition and drainage is clear from the differing paths of the curves, where the imbibition curve is always lower than the drainage curve, due to the saturation (and the ease of flow) of non -wetting phase decreasing. An intermediate curve, called the scanning curve is obtained when at some saturation (S_{ws}) the direction of saturation change of non-wetting phase is reversed before reaching either the maximum (S_{wmax}) or minimum (S_{wi}) obtainable saturations. In this case the relative permeabilities observed are an intermediate curve between the primary drainage and imbibition curves. The relative permeability will follow this scanning curve until it reaches either the drainage or imbibitions curve, where it will follow the path of the primary curves again. Both S_{wi} and S_{wmax} are shown, with dashed green lines forming the boundary of possible saturations and corresponding kr.

In a system in which H_2/CH_4 and water are present in sandstone, the water is typically the wetting phase and H_2/CH_4 is generally known as the non-wetting phase [2, 44]. In UHS, during drainage, the non-wetting phase displaces the wetting phase, while the opposite occurs during imbibition. Factors such as mineral composition of the surrounding porous rock, and the temperature and pressure at the depth of the reservoir can vary the wettability conditions [50].

Wettability is the tendency of a fluid to spread on the solid porous surface in the presence of another fluid, and is measured by the contact angle, as shown in Figure2.2 [50, 51]. Contact angles well below and above 90° represent wet and non wet conditions with reference to a particular phase, respectively [52]. In the case of the H_2/water/rock system or the CH_4/water/rock system, water occupies the smallest pores and pore throats as it coats the surface, while the non-wetting phase will primarily fill the center of larger pores [24]. This is advantageous result for UHS, as this means that H_2 and its mixtures with CH_4 will preferentially flow through larger pores, resulting in a higher relative permeability, facilitating the injectivity and efficiency of the reservoir [24].

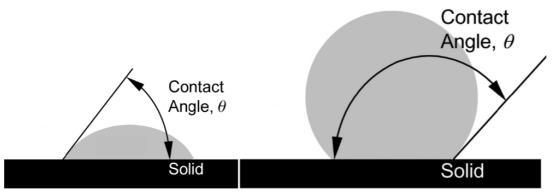

Figure 2.2: Schematic diagram of fluids exhibiting different wettability. Contact angle indicates the degree of wettability. Source; Baruch et al. [47]

This result is related to the capillary pressure (Pc). Pc significantly impacts H_2 behavior in reservoirs, and is important to characterize multiphase flow in geological porous media since it determines pore scale fluid movement, and reservoir scale flow [53]. Moreover, Pc controls the plume migration and trapping capacity of the injected H_2 gas, effecting the recoverability of H_2 from the reservoir [54].

Capillary pressure is the pressure difference between the interface of two immiscible fluids [49]. The pressure difference is expressed in terms of wetting and non-wetting phase pressures and can be expressed by the empirical relation:

$$P_c = P_{\text{nw}} - P_{\text{w}} \tag{2.2}$$

where Pc is the Capillary pressure, Pw is the wetting phase pressure, and Pnw is the non-wetting phase pressure.

This phenomenon of fluids to form an interface under tension arises due to the cohesive forces between like molecules, which are generally stronger than the adhesive forces between dissimilar molecules. As a result, there is a net inward attraction among the molecules of the same fluid, leading the interface to minimize its surface area, effectively behaving as if it were under tension [55]. This interfacial behavior is characterized by two key physical parameters: the interfacial tension (IFT), and the contact angle. Consequently, Pc can be more precisely described by the Young - Laplace equation:

$$P_c = \frac{2\sigma \cos\theta}{r} \tag{2.3}$$

where r is the radius of the pore throat, σ is the interfacial tension and θ is the contact angle between the fluid - solid interface and the fluid - fluid surface [44, 50].

This equation illustrates that capillary pressure is inversely proportional to pore throat radius. Therefore during drainage, greater Pc is required for the non-wetting phase to displace the wetting phase, or in other words, during injection cycles smaller pore throats are more resistant to H_2/CH_4 invasion. In contrast, larger pore throats would facilitate displacement of water by hydrocarbons due to the lower required Pc. As such, capillary forces will contribute to fluid distribution by selectively filling larger pores with hydrocarbons while trapping water in finer pore structures [56]. During drainage, as the non-wetting phase displaces the wetting phase, the saturation of the wetting phase decreases progressively. As the capillary pressure increases due to the increased pressure of the non-wetting phase, the wetting phase becomes confined to smaller pores and pore throats, where it eventually loses connectivity with the main flow paths. This process continues until the capillary pressure reaches a threshold beyond which the wetting phase can no longer be displaced, resulting in an irreducible water saturation (S_{wi}) [56].

The opposite occurs during imbibition, and non-wetting phase becomes trapped. In imbibition, trapping is described by a snap - off mechanism [13]. When the wetting phase infiltrates the corners of non-wetting phase filled pore throats, the non-wetting phase is ultimately disconnected from the solid surface [57]. Once contact is lost, the non-wetting phase becomes unstable and withdraws into the adjacent pore body, while the wetting phase rapidly fills the pore throat center [57]. When all connecting throats to a given pore body have experienced snap - off, the non-wetting phase becomes trapped within that pore body [24, 54], forming disconnected non-wetting phase clusters or ganglia. This phenomenon is a key process in residual trapping, which is often ascribed as the primary mechanism for gas immobilization in porous media, alongside structural trapping [50, 54]. It contributes to the hysteresis observed in kr and Pc functions, and leads to poorer storage ability during subsequent cycles of UHS [24].[23].

In UHS, minimizing residual gas saturation is desirable to maximize gas recoverability and storage efficiency. Notably, unlike within the reservoir itself, high Pc are favorable at the caprock to increase the sealing capacity of the caprock [44]. In UHS, H_2 (driven by gravity segregation) migrates to the top of the reservoir, settling at the caprock, where buoyant and capillary forces act on each other. If the capillary threshold (the minimum pressure needed to overcome the capillary pressure) is exceeded, brine saturating the caprock can be displaced by injected gasses, permitting the undesired migration of fluids, resulting in leakage from the reservoir, environmental contamination, or reservoir depletion [53].

Importantly, the interface between two fluids, including H_2/CH_4 mixtures and water, is stable or unstable depending on the relative magnitudes of the viscous, interfacial and gravitational forces and the direction of movement of the interface [58]. In horizontal flow, instability occurs when the mobility (the ratio of kr to μ) of the displacing fluid is greater than the mobility of the displaced fluidS. Generally, mobility ratios less than 1 are associated with stable displacement, while those larger than 1 indicate instability [58]. This instability can result in the formation of "fingers". Fingering refers to the phenomenon where one fluid displaces another in a non-uniform manner [58]. Hence, fingers can create bypass pathways for the displaced fluid, which may lead to uneven distribution of the gasses. Viscous fingering impacts sweep efficiency, developing into channels at high flow rates [24]. In UHS, this is detrimental to storage efficiency [59]. In experimentation, once channeling occurs, no meaningful relative permeability measurements can be made [24]. Fingering is influenced by several factors, including fluid viscosity, Pc, and the configuration of the pore space in the formation [59].

In two phase displacement, flow behavior, in the absence of gravitational forces, can be characterized by the pore scale capillary number (Ca) and the viscosity ratio (M) [60].

$$\mathrm{Ca} = \frac{\mu_i v}{\sigma} \tag{2.4}$$

Where v is taken as the superficial velocity and μ is the viscosity of phase i. M is defined by:

$$M = \frac{\mu_1}{\mu_2} \tag{2.5}$$

where μ_1 is the viscosity of the displaced phase and μ_2 is the viscosity of the displacing phase [60], and σ is the IFT between the displacing phase and the displaced phase. The capillary number describes the balance of viscous and capillary forces [60]. A higher capillary number represents viscous dominated regime, with Ca > 10^{-5} generally assumed to be the threshold between viscous dominated and capillary dominated fluid flow [44]. The interplay of viscous and capillary forces can lead to three different displacement regimes: viscous fingering, capillary fingering, and stable displacement as described by Guo et al. [60] (represented in Figure2.3). In the capillary dominated regime the formation of viscous fingers is expected to be substantially less.

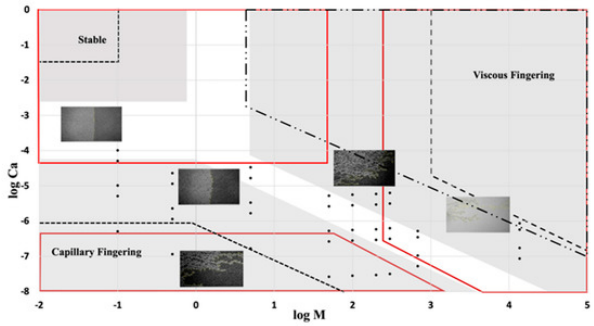

Figure 2.3: Flow phase diagram with boundaries of three flow regimes. Source: guo et al. [60]

When a gas is applied to displace liquid from a porous medium, gravity override occurs due to the high density contrast between the gas and liquid phases, in which the injected gas rises to the top of the formation [2, 59]. Gravity overriding causes the bypassing of the fluids being displaced and results in lower sweep efficiency, and thus lower usage of the available pore space in the host medium [8, 59]. Boon et al. [24] reported gravity segregation when H_2 was used to drain water from a sandstone core in a horizontal configuration. Zhong et al. [2] observed similar behavior, noting that H_2 exhibited a higher degree of gravity overriding in horizontal flow compared to CH_4, as evidenced by earlier breakthrough of the gas.

In order to reduce the effect of gravity override and viscous fingering in experimentation, core flood tests are sometimes conducted on vertically oriented samples for gas water systems as seen in table 2.3. This

orientation utilizes gravity to stabilize the gas liquid interface, and avoid gravity segregation, resulting in a more uniform displacement front [61]. However, while the displacing front is successfully stabilized, the effect of gravity may significantly alter the derived relative permeability from equation (2.1), as the displacement will then be affected by gravity forces as well as by both capillary and viscous forces [61]. Alternately, in horizontal flow, gravity does not effect fingering [62], and if conducted at high flow rates, can reduce the influence of gravity on the displacement front of the gas - fluid system, and increase the dominance of viscous forces that vertical core floods minimize [61]. Such configurations would also better capture the effects of gravity override, and areal sweep efficiency as fluids flow across porous media, as would be the case in large scale reservoirs for UHS. The kr derived from such a horizontal configuration might then more adequately reflect real world phenomena, and provide potentially more realistic kr values.

Generally, both kr and Pc can be experimentally determined through two principal approaches: the steady state and unsteady state methods. The unsteady state method involves the injection of a single phase (commonly the non-wetting phase) at a constant flow rate or constant pressure into a water saturated core. The pressure gradient and flow rate determine the relative permeability as a function of saturation, which can be estimated using mass balance, x-ray imaging, or nuclear magnetic resonance. While this method is considerably faster than steady state, it introduces greater uncertainty in subsequent calculations and provides a relatively narrow saturation range for which kr curves can be obtained [63] [64]. In the steady state approach two fluids (non-wetting and wetting phase) are simultaneously injected into a core sample at controlled fractional flow rates, at constant ratio, until steady state conditions are achieved: pressures stabilize sufficiently allowing the measurement of the Darcy permeability with equation 2.1 [65]. At this point, water saturation, along with the pressure differential between the inlet and outlet of the core, and various points along the core length are measured [24]. Achieving steady state can be time consuming particularly due to the dependence on fluid properties and pore structure, though it enables straightforward calculation of relative permeability. Furthermore, when coupled with steady state techniques, capillary pressures can be easily measured using simple yet effective methodologies such as that by Pini et al. [66], which uses a similar experimental setup as that for many steady state experiments, requiring no additional apparatus [24]. There is substantial uncertainty in literature over whether the results of these two different types of multiphase flow experiments produce the same kr [64]. However, steady state experiments are commonly conducted [20, 24, 45], and Miguel et al. [67] have suggested that for lower capillary number($Ca \ll 10^{-2}$) the difference between steady state and unsteady state relative permeabilities is almost negligible.

In core flood experiments, the capillary end effect is often observed. This involves the noticeable increase in wetting phase saturation at the end of a core, due to accumulation of the wetting phase at the core ends as a result of the sudden change in capillary forces between the interface of the core and the surroundings. To minimize capillary effects on the saturation profile recorded along the length of the core, longer cores are recommended and often used (Table 2.2) [61].

Additionally, the linear trapping coefficient (A), is used to characterize the trapping ability of rock:

$$A = \frac{S_{gr}}{S_{gi}} \tag{2.6}$$

where, S_{gr} is the residual gas saturation at the end of imbibition, and S_{gi} is the initial gas saturation at the start of imbibition. High trapping coefficient indicates high trapping ability. Lower trapping coefficient are favorable in UHS as it aims to recover as much stored gas as possible. The difference between the trapped and produced gas is termed the "working" gas.

2.2. Influencing factors

Numerous parameters could influence the kr and Pc of H_2/CH_4 in the subsurface. Figure2.4 provides an overview of the general parameters, including kr and Pc, that are of particular importance in UHS operations. The following is a review of the relevant fluid - fluid properties to the H_2 and the CH_4 systems respective kr and Pc. The relevant solid and solid - fluid interactions are not described as they have been discussed previously. Note that a a direct discussion on rock structure/mineralogy, salinity, temperature, and pressure are omitted from this discussion as they will be kept constant in the subsequent experiments, and the effects of their variability are interlinked with the changes in other fluid properties discussed below.

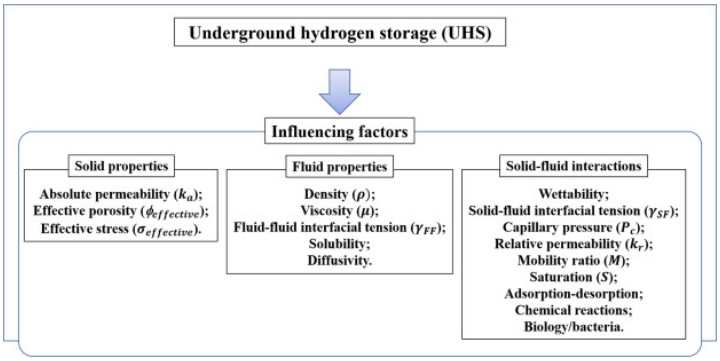

Figure 2.4: Influencing parameters for UHS

Density

The density of H_2 increases with rising pressure and decreases with increasing temperature. When compared to other gases (such as CH_4 and CO_2) H_2 density is significantly lower (see Figure2.5). Both H_2 and CH_4 will decrease substantially with pressure, and more minimally with temperature. From Figure2.5, an increase of 7 kg m^{-3} and 75 kgm^{-3} for both H_2 and CH_4, at pressures from 0 - 10 MPa, are observed respectively. The significantly lower density of H_2 to CH_4 and brine will lead to an increase in gravity override, which significantly impacts sweep efficiency [37, 68]. The mass density ratio of CH_4 to CH_4 - H_2 mixtures serves as an indicator of the relative buoyancy strength of mixtures [59]. Figure2.6 shows the mass ratios of various H_2/CH_4 mixtures with pressure and temperature. Compared to pure H_2 at 25 C and 100 bar, the CH_4 to 50-50% CH_4 - H_2 mass ratio is significantly lower (9.75 for pure H_2, compared to 1.815 for 50-50% CH_4 - H_2 mixture). This indicates that the buoyancy driving gravity override is substantially less in CH_4 - H_2 mixtures. The same trend is seen when comparing the mass ratios of water to CH_4 - H_2 mixtures, with higher temperatures slightly increasing the mass ratio, and higher pressures significantly decreasing it [59]. Consequently, the gravity override effect for CH_4 and H_2 can be expected to diminish with an increased pressure and greater CH_4 fraction in the gas mixture, which would improve sweep efficiency in UHS operations and in core floods.

Viscosity

Fluid viscosity, along with the mobility ratio, plays a significant role in controlling viscous fingering phenomena during the injection of H_2 into the subsurface [68]. Knowledge of viscosity contrasts between H_2/CH_4 and brine is crucial to improve storage efficiencies and understand kr in UHS. Viscous fingering reduces gas storage efficiency and hinders kr measurements by reducing sweep efficiency, where fingers are zones of least resistance and gas flows preferentially through these fingers leaving unswept areas. Viscous fingers bring a larger fraction of the working gas volume in proximity to saturated brine regions in the porous medium, which may potentially increase gas dissolution and diffusion within the brine [39]. This can alter gas mixture compositions and effect subsequent kr measurements of gas H_2/CH_4 mixtures.

Furthermore, viscosity is directly related to kr through equation 2.1, where higher viscosity leads to a higher kr. From Figure2.7 it can be seen that temperature and pressure have a minimal impact on H_2 viscosity when compared to CH_4. The viscosity of CH_4 is higher than H_2 across the range of pressures and temperatures relevant to UHS, though it increases linearly with increasing pressure, and decreases

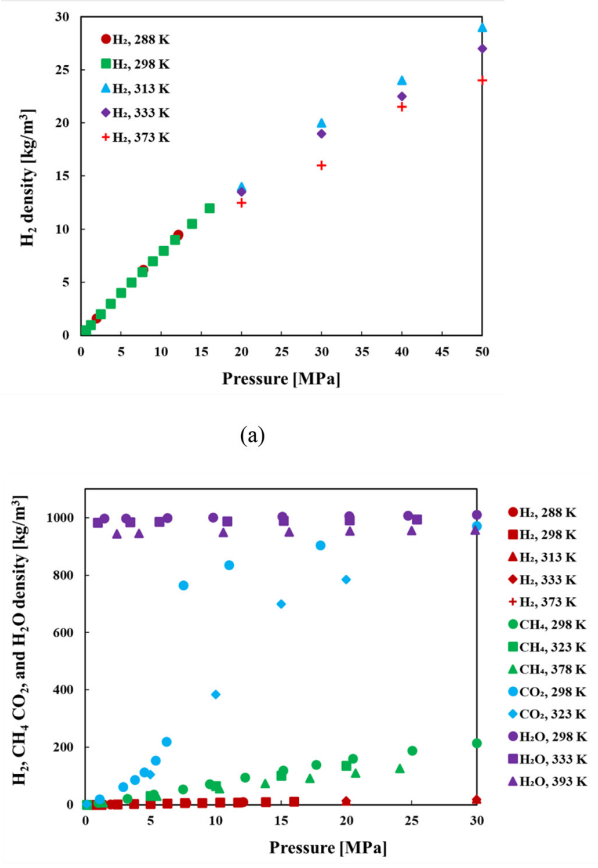

Figure 2.5: Hydrogen, Methane, and Carbon Dioxide density with pressure and temperature. Top: Hydrogen, Bottom: All Gasses. Source [19]

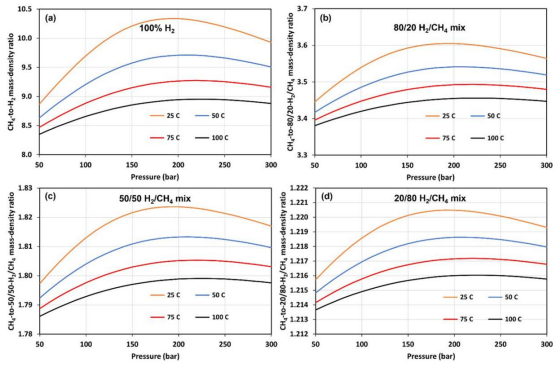

Figure 2.6: CH_4 to mixture mass ratio of different H_2/CH_4 Mixtures. Source [39]

with increasing temperature. This relation is supported by Pan bin et al. [68], who noticed that at 20 MPa $\mu H2$ increased slightly from $9.6 \cdot 10^{-3}$ mPa · s to $10.7 \cdot 10^{-3}$ mPas when temperature increased from 313 K to 373 K, while at 373 K, μH_2 slightly increased from 10.4 10^{-3} mPas to 11.8 $\cdot 10^{-3}$ mPas when pressure increased from 0.1 MPa to 50MPa. In contrast, μCH_4 increased from 13.6 $\cdot 10^{-3}$ mPas to 26 $\cdot$10−3 mPas when pressure increased from 0.1 MPa to 48 MPa at 373 K. This indicates that μCH_4 is similar to μH_2 at lower pressures (<10 Mpa), but more than twice as high as μH_2 at higher pressures.

Notably, the water to H_2/CH_4 dynamic viscosity ratio decreases with pressure and temperature, indicating that at higher depths (higher pressure), viscous fingering could be suppressed as the viscosity contrast is reduced, which would be favorable for experimentation and for any UHS operation.

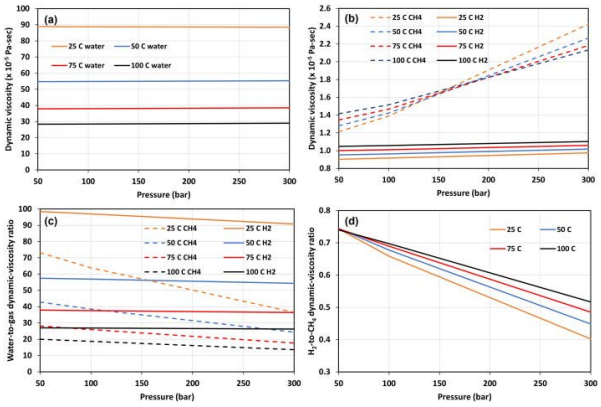

Figure 2.7: Viscosity contrast between H_2, CH_4, and water, plotted as function of temperature and pressure. Viscosity of water (a), dynamic viscosity of H_2 and CH_4 (b), water-to-gas dynamic-viscosity ratio for H_2 and CH_4 (c), and H_2-to-CH_4 dynamic-viscosity ratio (d). Source [39]

Ultimately, H_2 viscosity is greater than CH_4 across the relevant range of pressures and temperatures. Considering the direct impact of viscosity on fluid flow, it can be expected that $_2/Ch_4$ mixtures will have higher kr the higher the H_2 composition within them.

Interfacial Tension

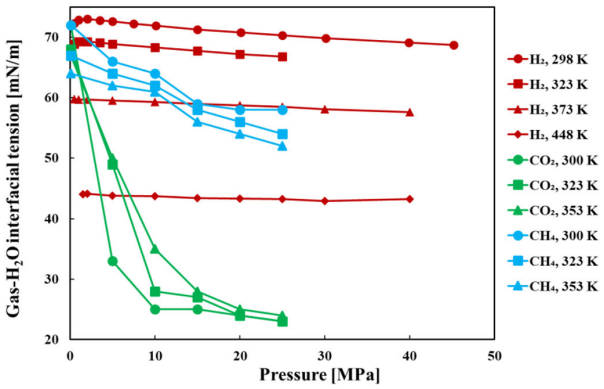

Figure 2.8: H_2, CO_2, and CH_4 interfacial tension plotted as functions of temperature and pressure. Source [68]

IFT is of particular importance in subsurface systems because it directly controls Pc [69] as shown by the Young - Laplace equation (equation 2.4), and influences the degree of fluid–fluid miscibility [70, 71]. A lower IFT will result in a lower Pc, which may result in less trapping of gas during UHS, and reduced hysteresis. IFT is a function of pressure and temperature. The IFT for H_2, CH_4, and CO_2 in water across a range of pressure and temperatures is shown in Figure 2.8. It can be observed that the interfacial tension between H_2 and water is largely insensitive to pressure but decreases significantly with increasing temperature. For example, at 323 K the IFT of the H_2–H_2O system decreases only slightly, from 70 mN m^{-1} at 0.1 MPa to 67 mN m^{-1} at 40 MPa. Conversely, at 10 MPa the IFT declines more strongly, from 72 mN m^{-1} at 298 K to 44 mN m^{-1} at 448 K. This behavior contrasts with that observed for the CH_4–H_2O system, in which the IFT decreases strongly with pressure and only somewhat with temperature. Specifically, at 323 K an increase in pressure from 0.1 MPa to 25 MPa causes the IFT to fall from 67 mN m^{-1} to 54 mN m^{-1}, while at 10 MPa an increase in temperature from 300 K to 353 K causes the CH_4–H_2O IFT to decrease from 64 mN m^{-1} to 61 mN m^{-1}. Buscheck et al. [39] noted that, due to these differences, the IFT of H_2–CH_4 mixtures with water decreases with both increasing temperature and increasing CH_4 fraction. Similarly, Alanazi et al. [72] investigated the IFT of H_2–CH_4/brine mixtures containing 2 wt.% NaCl and 1 wt.% KCl. The experiments were conducted at 323 K and at pressures ranging from 6.89 $\cdot 10^{-3}$ to 110 bar. The variation of CH_4/brine IFT with increasing pressure was more pronounced than that of H_2/brine. In particular, the CH_4/brine IFT decreased rapidly beyond 27.6 bar. The mixture/brine IFT values were found to be intermediate between those of pure H_2, and pure

CH_4. Furthermore, the analysis of Mirchi et al. [69] indicated that H_2/CH_4 mixture/brine IFT declined with increasing CH_4 fraction. It was observed that decreasing the H_2 content in H_2/CH_4 mixtures led to a slight reduction in gas/brine IFT at all temperatures examined. For instance, at a constant temperature of 40°C, the IFT decreased from 67.85mN/m for a mixture containing 80% H_2 and 20% CH_4 to 64.88mN/m for an equal (50–50%) mixture. This reduction in IFT can be attributed to stronger interactions between CH_4 and brine molecules at the fluid-fluid interface [69]. Mirchi et al. [69] further concluded that the CH_4/H_2 ratio in the mixture will have minimal effect on wetting. Other studies have further suggested that IFT of pure H_2 and pure CH_4, and H_2/CH_4 mixtures, will decrease with increasing pressure and temperature at any given salinity, while increasing for an increase in salinity [73, 74].

Solubility

The solubility of gas is an important factor that determines how much of the injected gas can be lost via dissolution into the native brine and how much will remain as a separate gas phase [19]. Significant dissolution effects may aid the development of fingers in core flood experiments, as observed by Boon et al. [24], which hinder kr measurements. Solubility may also reduce or alter the composition of the established mixture, leading to inaccuracies in analysis.

Temperature, pressure, and reservoir salinity exert a significant influence on H_2 solubility under UHS conditions [26, 75]. In general, increasing pressure and decreasing temperature enhances H_2 dissolution, whereas increasing brine salinity reduces H_2 solubility, due to the salting out effect [59]. However, at higher temperatures (≥ 320 K), and high pressures (≥ 100 - 200 bar), increasing temperature reustls in an increase in H_2 solubility. For example, Chabab et al. [75] noted that at 372 K, raising the pressure from 3.3 MPa to 23 MPa increased the H_2 solubility in 3 mol/kg NaCl brine from 2.15×10^{-9} mole fraction to 1.3×10^{-7} mole fraction. Similarly, at 10.1 MPa, increasing the temperature from 323 K to 373 K raised the H_2 solubility in 3 mol/kg NaCl brine from 6.32×10^{-8} mole fraction to 7.03×10^{-8} mole fraction.

The salting out effect reduces solubility of gas as salt ions compete with gas molecules for available space in the liquid phase, thereby reducing the concentration of dissolved gas [26]. The magnitude of this effect depends on the gas and the salt concentration. Furthermore, different salts can exert varying impacts on gas solubility due to differences in ion size and charge [19]. Gholami et al. [76] compared the influence of monovalent ions (Na^+ and K^+) with divalent ions (Ca^{2+} and Mg^{2+}) on H_2 solubility. The study demonstrated that divalent ions exert a stronger effect in reducing the solubility of H_2 compared to monovalent ions. Among monovalent ions, K^+ decreased solubility more than Na^+, while among divalent ions, Ca^{2+} showed a stronger effect than Mg^{2+}. This observation may be attributed to differences in ion size and ionic potential energy in solution.

CH_4 is slightly more soluble in water than H_2, and decreases with temperature and salinity, while increasing with pressure [77]. Duan et al. [78] recorded the CH_4 solubilities in water at different pressures, temperature and salinities in NaCl brine. At a pressure of 100 bar, in pure water, CH_4 solubility decreased from 0.1623 $molkg^{-1}$ at 273 k to 0.0949 $molkg^{-1}$ at 303 K. Similarly, at 303 K and 100 bar pressure, the solubility of CH_4 decreased from 0.0762 $molkg^{-1}$ at 1 $molkg^{-1}$ salinity to 0.062 $molkg^{-1}$ at 2 $molkg^{-1}$ salinity. Contrastingly, the increase with pressure was more significant, at 303 K in pure water, the solubility increased from 0.0023 $molkg^{-1}$ at 1 bar pressure, to 0.00949 $molkg^{-1}$ at 100 bar.

Tawil et al. [79] investigated the solubilities of varying H_2/CH_4 mixtures. Very similar curves were obtained for all mixtures, which closely matched the solubilities of pure H_2 and pure CH_4. The study further found that mixtures dissolve more easily in brine when the fraction of H_2 in the mixture is lower. This is in agreement with literature, as pure CH_4 is known to be more soluble than pure H_2 in water [80]. Tawil et al. [79] further observed that salinity was not significant and the effect of temperature was limited when compared to pressure, which corresponds to the observations made by Chabab et al. [75] and Bottger et al. [77].

Despite the low solubility of both CH_4, H_2 , and their mixtures, literature has shown 0.4% of injected H_2 can be lost due to the dissolution of H_2 into formation brine during the first drainage/imbibition cycle [3]. Dissolution may have a simar effect in core flood experiments. Furthermore, in experiments that aim to minimize this effect through equilibration between water and gas phases, slight differences between inlet and down core pressure may result in exsolution of gas down core, hindering flow and the corresponding measured kr of the fluids [13, 81].

Diffusivity

Diffusivity describes the amount of gas that diffuses across a rock surface, and is a function of temperature, pressure, and salinity [68]. Diffusion can cause the gas phase to reaccommodate in the pore space such as through Ostwald ripening, freeing trapped gasses from small and more capillary bound pores overtime, enhancing producibility of gas and the kr as a result [13]. In aqueous systems, H_2 diffusivity increases with temperature and pressure [82]. Notably, the diffusivity of H_2 in water is nearly three times that of CH_4 [83]. Therefore, it can be expected that on a shorter time scale, more H_2 will be able to reaccommodate/dissolve into water than CH_4, and potentially lead to less hysteresis between drainage/imbibition in the H_2 brine/rock system. However, diffusivity is minimal on the time scales needed for a typical core flood experiment [81]. For any meaningful reaccommodation to occur, daily timescales are often required [13]. In other words, the impact of diffusivity is likely to be negligible on the measured kr in this study.

Considerations

In all, while all the aforementioned factors can lead to distinct fluid flow between the H_2/CH_4 systems, the most influential to kr and Pc appear to be their respective viscosity and IFT, due to their substantial differences at the conditions relevant to UHS and their direct impact on both kr and Pc as shown by equations 2.1 and 2.3, and on other factors such as wettability (a function of IFT). Solubility and diffusivity can be important when considering the composition of gas mixtures, though the low solubility and diffusivity of each gas suggest they will pose a minimal influence to fluid flow. Overall, due to these property contrasts, H_2 can be expected to show higher kr and higher Pc than CH_4 under comparable conditions, resulting in more significant hysteresis between drainage/imbibition cycles in the H_2 system. Their mixtures, however, may potentially exhibit intermediate properties between those of the pure gases.

2.3. Previous studies on relative permeability and capillary pressure

To the extent of the authors knowledge there is no literature or published data on experimentally derived kr and Pc for H_2/CH_4 mixtures in brine/rock systems. Nevertheless, various studies have been conducted on the pure H_2 and CH_4 brine/rock systems that can facilitate comparisons and give insight to $H_2/\ CH_4$ mixture flow.

Recently, various studies have been conducted on the CH_4 and H_2/brine/rock systems [2, 44–46, 48, 73, 84]. In short, these studies have shown that the CH_4/brine/rock system is comparable to the H_2/brine/rock system in terms of wettability, contact angle, IFT, and their response to varying pressure and temperature [19, 37, 40, 73, 84].

H_2 kr and Pc was first experimentally investigated by Yekta et al [45], though in recent years, the number of studies investigating this has increased [24, 44, 46, 48, 84]. In these studies, numerous reservoir parameters such as temperature and pressure have been used to represent varying storage depths, with low temperature and pressure representing shallow reservoirs and high temperature and pressure representing deep reservoirs. A comparison of these studies is complex, notably due to rock heterogeneity and sample type between the samples used. Differences in a rock's pore structure can lead to varying capillary forces, diffusivity, and permeabilities, which significantly impact fluid flow [45, 85]. Indeed, rock type and structure has been suggested to have the most influence on H_2 kr [46]. In fact, numerous studies performed on different rock types highlight the significant influence of mineralogy on fluid behavior in subsurface formations, influencing wettability, IFT, and adsorption [19, 86–89], emphasizing the need to perform studies on similar rock types for meaningful comparisons.

Yekta et al. [45] measured H_2/water drainage kr and the Pc in a vertically positioned lower Triassic Vosges sandstone core by running two steady state drainage experiments, one simulating a shallow aquifer (20 °C, 55 bar) and one a deeper aquifer (45 °C, 100 bar). Each test was repeated at different flow rates with a total combined injection rate of 1 $mLmin^{-1}$. Their results show that the H_2/water system operates under a capillary dominated regime, and that in the range of pressures (0 - 100 bar) and temperatures (< 100°C), H_2 kr will not largely vary. The relative permeability curves for H_2 differed only by at most 10 % between both configurations. This was attributed in part to a capillary dominated regime, where viscous forces were negligible, clearly seen by the nearly constant viscosity of H_2 over this range (Figure 2.7). Similarly, interfacial tensions and contact angles showed the same insensitivity to pressure and temperature, suggesting that reservoir depth may not significantly impact kr and Pc as opposed to the rock properties itself.

However, Higgs et al [44] challenges this hypothesis, suggesting that the interfacial tension of H_2 should lower at higher pressure and temperature, reducing capillary resistance, and permitting the H_2 to flow more easily throughout the pore space, increasing kr. In contrast, Rezaei et al [46] found a pressure dependence of H_2 kr with higher pressures leading to higher H_2 viscosity, reducing mobility, and the kr as a result. However, they observed higher H_2 kr at higher pressures and lower gas saturations. They reasoned that at lower gas saturations, the capillary forces dominate over viscous forces, so the lower IFT at higher pressures causes the H_2 to more easily overcome capillary barriers and enter the pore space, increasing the H_2 kr with pressure, similar to the reasoning by Higgs et al.

This behavior introduces a more complex relation between pressure and kr. The effect of pressure on kr is not fixed (as suggested by Yekta et al), though rather depends on the saturation level of the gas, suggesting that in the early stages of injection (low gas saturation), pressure can help flow (via lowering IFT), however in later stages (high gas saturation), pressure may hinder flow (via higher viscosity).

Rezaei et al. further observed that at ambient pressure (1 bar) kr was highest, while at higher pressures (100 - 200 bar) the kr curves did not appear to change. This suggests that beyond a certain pressure, the impact of pressure on H_2 kr becomes less prominent. It should be mentioned that at higher temperature and pressure (45°C/100 bar) Yekta et al observed lower gas fractional flows, when compared to lower pressure and temperature (25°C/55 bar). In other words, H_2 becomes less effective at pushing water out of the rock for higher temperature and pressure, even though its ability to flow (relative permeability) does not seem to change by a significant degree. Thus, Yekta et al's conclusion may agree with Rezaei et al's findings, though only at higher pressures, where they reveal similar pressure dependent behavior.

To continue, the behavior of CH_4 systems does not seem to be significantly dissimilar to the H_2 system across a range of temperatures and pressures. Higgs et al [84] performed steady state relative permeability experiments at 2.13 MPa and 298 K on Bentheimer sandstone using H_2, CH_4, and N_2/water/rock systems under identical capillary numbers ($2.92 \cdot 10^{-7}$), combined with 3D micro CT imaging to measure saturation and in situ contact angles. Their results show that the contact angles for CH_4 and H_2 were on average 44°, and 46°, respectively, with contact angles ranging predominantly from 20 - 40° for CH_4, and 20 - 30° for H_2. Similar ranges were found by Hashemi et al. [40], with H_2, CH_4, and their mixtures contact angles ranging from 25° - 45°, at a range of temperature (30 - 50° C), pressure (20 - 100 bar), and salinity (0 - 5000 ppm). Adding on, this falls within the range of contact angles found by Muhammed et al. [37] and Gbadmosi et al. n[19], between 25° - 40° (at 34.5 - 207 bar, 30 - 70° C, and 2 - 20 wt% brine).

Notably, the higher the CH_4 fraction in the mixture, the less water wet the system becomes. The more weakly water wet rock surfaces could be advantageous for recovery of H_2 from depleted gas reservoirs as the greatest recovery of H_2 occurs when the rock surface is intermediate wet [48]. Furthermore, due to the CH_4 being slightly more wetting than H_2 in the brine/sandstone system [2, 40, 84], the recovery of gas from the produced H_2 stream in the presence of this cushion gas could be more facilitated, albeit with less purity.

These results seem to suggest that the Pc, as a function of IFT and wettability, may be significantly altered when adding higher CH_4 fractions to the H_2 phase, affecting the trapping and overall flow pattern of the gas mixture in porous rock. However, Higgs et al. [84] points out that most prior studies use inconsistent flow conditions, often under capillary limited regimes, which exaggerate differences. Higgs et al. [84] suggests that for the derived values of kr and Pc to be truly representative (i.e., intrinsic and suitable for reservoir scale modeling) core flood experiments must be conducted at high capillary numbers where viscous forces dominate and the influence of small scale heterogeneities is minimized [44, 90]. Under capillary limited conditions fluid properties such as viscosity and IFT, as well as rock heterogeneity, can profoundly alter mobility and fluid distribution [91], as observed in both CO_2/brine [66, 90, 91] and H_2/brine experiments [20, 24], which operated at lower capillary numbers ($9.1 \cdot 10^9$ - 10^8). To investigate this, Higgs et al. [84] performed steady state core floods of H_2, CH_4, and N_2 at the same capillary number ($2.097 \cdot 10^{-7}$) and reported nearly identical capillary pressure saturation relationships (end point Pc=9.51 kPa for H_2 vs. 9.36 kPa for CH_4), end point kr (0.049 vs. 0.045), and residual gas saturation (S_w = 0.25 and 0.24 for H_2 and the CH_4 respectively). The study showed that given identical capillary numbers, the H_2/CH_4/water systems should display the same intrinsic relative permeability curves and produce equivalent flow properties under conditions relevant for UHS. Higgs et al. [84] went further to suggest that if scaled by capillary number, the results of other core flood experiments (Lyssy et al. [20] and Reynolds et al. [90]) would be comparable. Higgs et al. [84] highlights the correlation between capillary number and the relative permeability saturation relationship. As the capillary number increases the relative permeability curves shift toward lower water saturations due to flow dynamics approaching the viscous limit, reducing the influence of heterogeneity and fluid properties such as IFT on the relative permeability. This is in agreement with Reynolds et al. [90], who demonstrated that core floods conducted near the viscous limit yield converging relative permeability curves.

Manoorkar et al. [92] investigated the relative permeability for H_2 and CH_4, in carbonate rocks at 100 bar and 22 ° C. Their results reveal that H_2 exhibits similar relative permeability curves to CH_4, with similar end point wetting phase saturations (0.6) and end point kr of 0.007 and 0.0055, for H_2 and CH_4, respectively, consistent with previous literature. Manoorkar et al. [92] further noticed that at higher wetting phase saturations the CH_4 kr is slightly higher than the H_2 kr. They attributed this to the higher capillary number at higher wetting phase saturation, and the higher viscosity ratio of CH_4 (0.016) compared to H_2 (0.01). The higher viscosity ratio facilitates connectivity in the CH_4 front, resulting in higher gas permeability. However, as wetting phase saturation decreases, capillary forces begin to dominate the flow and the kr values for CH_4 and H_2 converge.

Rezaei et al. [46] observed a similar relation, except while CH_4 kr was consistently higher than H_2 kr, H_2 had a higher maximum kr (0.36), as it was able to reach higher end point saturations (0.44 compared to 0.36, for H_2 and CH_4, respectively). Unlike Manoorkar et al, Rezaei justified the observations by explaining that H_2 has a higher IFT than CH_4, which causes H_2 to invade fewer, and only larger pores, and that the effect of interfacial forces (i.e Capillary forces), are higher than viscous forces at higher

water saturations. The apparent discrepancy between their reasoning can be explained by considering that capillary forces dominate hydrogen flow in UHS both at high water saturation by limiting gas invasion through capillary entry pressures and at low water saturation by controlling the pore scale phase configuration and endpoint relative permeability. The discrepancy in reasoning aside, they both attributed the higher end point H_2 kr to its lower viscosity. The lower viscosity would result in a higher mobility for H_2, and thus increased flow. Rezaei et al. noted that this behavior is favorable for UHS, as at higher water saturation the lower H_2 kr would reduce the risk of viscous fingering, improving overall sweep efficiency, while at lower wetting phase saturations, the higher H_2 kr will help it achieve better recovery rates. They concluded by stating that due to this, H_2 will have more favorable flow behavior than CH_4 during both drainage and imbibition stages, implying that, despite the similar kr curves for CH_4 and H_2, mixing of the two gases will lead to unfavorable flow characteristics, and will hinder the productivity of reservoirs where significant mixing occurs. Notably, the end point kr of H_2 in Rezaei et al is an order of magnitude higher than other kr studies for the H_2/brine/rock system (see table 2.1). While strange, they did not couple their experiments with imaging, so one can not tell whether the higher end point kr observed is a result of channeling at the end of their experiment.

An overview of published core flooding experiments can be found below, along with a few of the physicochemical properties of H_2, CH_4, and their 50-50% molar mixture, and water at the experimental conditions that will be used for this study (100 bar and 18 ° C).

Considerations

Taken together, literature surmises that the kr and the Pc of the pure H_2/pure CH_4 brine/rock system should be similar. Despite this, a complex interaction of gravitational, capillary, and viscous forces should be expected for H_2/CH_4 mixtures, owing to the stark differences of both gases physicochemical properties. Moreover, it is clear from literature that it is imperative to conduct experiments under similar conditions and methodologies to facilitate and provide more meaningful comparisons. Hence, this study emulates the methodology of Boon et al. [24], that allowed the analysis of the complex flow behavior of H_2 through a Berea sandstone core during multiple drainage and imbibition cycles, and extends it to the pure H_2, pure CH_4 and 50-50% CH_4/H_2 mixture systems. In this way, this study aims to eliminate experimental discrepancies that would otherwise raise additional uncertainties.

Study	Lithology	Core Size [cm (D/L)]	Temp. [°C]	Pressure [bar]	Porosity [%]	Permeability [mD]
Yekta et al., 2018 [45]	Vosges Sandstone	1.5/6.1	20–45	55–100	19	44
Jha et al., 2021 [93]	Gosford Sandstone	0.5/1.5	20	1	18	–
Al-Yaseri et al., 2022 [43]	Fontainebleau Sandstone	3.9/5.5	25	4	10	190
Rezaei et al., 2022 [46]	Sandstone & Carbonate	3.8/8.9–9.5	80	1–206.8	10.5–16.4	3–34
Boon & Hajibeygi, 2022 [24]	Berea Sandstone	3.8/17	18	100	20	203
Lysyy et al., 2022 [94]	Berea Sandstone	3.8/27.6	30	30	18	107
Thaysen et al., 2023 [95]	Clashach Sandstone	0.5/5.4–5.7	20	20–70	13–14	–
Jangda et al., 2023 [96]	Bentheimer Sandstone	0.6/2.7	50	100	23	2900
Goodarzi et al., 2024 [97]	Bentheimer Sandstone	1.3/6.0	25	10	22.6	1400
Higgs et al., 2024 [44]	Bentheimer Sandstone	0.6/1.3	25	21.3	23	653
Raadmaker et al., 2024 [13]	Berea Sandstone	1.0/17	25	50	18.3	104
This study	Berea Sandstone	3.8/17	18	100	16	80

Table 2.1: Summary of core flood experimental conditions from various studies. This table is based on data gathered by Higgs et al. [44] and has been extended

Study	Capillary Number Range [-]	Initial Gas Saturation [-]	Residual Gas Saturation [-]	H_2 End-point Rel. Perm. [-]
Yekta et al., 2018 [45]	$1.17 - 1.25 \times 10^{-8*}$	0.59–0.60	–	0.035–0.044
Jha et al., 2021 [93]	$2.49\times10^{-10} - 3.68\times10^{-8\wedge}$	$0.65^{\triangle}$	$0.41^{\triangle}$	–
Al-Yaseri et al., 2022 [43]	$3.54 \times 10^{-8*}$	$0.04^{\triangle}$	$0.02^{\triangle}$	–
Rezaei et al., 2022 [46]	–	0.22–0.28	–	0.260–0.360
Boon & Hajibeygi, 2022 [24]	$9.1 \times 10^{-9} - 1.1 \times 10^{-6*}$	$0.36^{\square}$	$0.24–0.17^{\square}$	0.019
Lysyy et al., 2022 [94]	$1.88 \times 10^{-9} - 1.74 \times 10^{-7*}$	$0.41^{\square}$	$0.36^{\square}$	0.037–0.083
Thaysen et al., 2023 [95]	$1.2 \times 10^{-8} - 9.5 \times 10^{-6\wedge}$	0.50–0.53	0.1–0.21	–
Jangda et al., 2023 [96]	$4.2 \times 10^{-9} - 2.3 \times 10^{-6*}$	$0.36^{\triangle}$ - $0.36^{\square}$	$0.20^{\triangle}$ - $0.25^{\square}$	–
Goodarzi et al., 2024 [97]	$1.93 \times 10^{-7} - 5.79 \times 10^{-9*}$	$0.30^{\triangle}$	$0.10^{\triangle}$	–
Higgs et al., 2024 [44]	$2.92 \times 10^{-7} - 2.92 \times 10^{-5*}$	$0.76^{\triangle}$	$0.40^{\triangle}$	0.049
Tim Raadmaker et al., 2024 [13]	$1.3 \times 10^{-8} - 1.3 \times 10^{-6*}$	$0.44^{\square}$	$0.32^{\square}$	0.043

Table 2.2: Results from previous relative permeability and residual trapping studies. Empty fields indicate that the data was either not determined in the study or not provided by the authors. This table is based on data gathered by Higgs et al [44] and has been extended

. *: Determined with Darcy velocity; ∧ : Determined with Interstitial velocity ; △ Determined with non-equilibrated brine; □ :Determined with H_2 equilibrated brine

Study	Displacement Methodology	Flow Orientation	Imaging Technique
Yekta et al., 2018 [45]	steady state	Vertical	None
Jha et al., 2021 [93]	Unsteady state	Vertical	Micro-CT
Al-Yaseri et al., 2022 [43]	Unsteady state	Vertical	NMR
Rezaei et al., 2022 [46]	Unsteady state	Vertical	No
Boon and Hajibeygi, 2022 [24]	steady state	Horizontal	Medical -CT
Lysyy et al., 2022 [94]	Unsteady state	Vertical	Micro-CT
Thaysen et al., 2023 [95]	Unsteady state	Vertical	Micro-CT
Jangda et al., 2023 [96]	steady state	Vertical	–
Goodarzi et al., 2024 [97]	Unsteady state	Vertical	Micro-CT
Higgs et al., 2024 [44]	steady state	Vertical	Micro-CT
Tim Rademaker et al., 2024 [13]	steady state	Vertical	Medical CT

Table 2.3: Experimental methods of previous relative permeability and residual trapping studies. Empty fields indicate that the data was either not determined in the study or not provided by the authors. This table is based on data gathered by Higgs et al [44] and has been extended.
D = Drainage; I = Imbibition.

Properties	H_2	CH_4	Mixture	Water
Molecular Weight (g /mole)	2.02 [98]	16.04 [98]	9.03 [99]	18.02 [98]
Density (kg/m^3)	7.85 [98]	79.31 [98]	61.56 [99]	1003.1 [98]
Viscosity (Pa s)	8.88×10^{-6} [98]	1.37×10^{-5} [98]	1.03×10^{-5} [99]	$1.05 \cdot 10^{-3}$ [98]
Interfacial Tension with water (Nm^{-1})	71.9×10^{-3} [69]	61×10^{-3} [59]	67×10^{-3} [69]	–
Solubility in 1% brine (mol kg^{-1} H_2O)	7.56×10^{-2} [100]	11×10^{-2} [77]	9.247×10^{-2} * [79]	–
Diffusion coefficient in pure water (m^2/s)	$4.18 \cdot 10^{-9}$ [101]	$1.39 \cdot 10^{-9}$ [101]	$4.1750 \cdot 10^{-9}$	–

Table 2.4: Physical properties of H_2,CH_4, their 50 - 50% mixture, and water. Adapted from [3]
* Tawil et al. [79] at 90 bar pressure and 45 C.

3

Methodology

The main objective for this research is to understand the disparity in relative permeability and capillary pressure between H_2/CH_4 mixtures in conditions relevant to UHS. In order to answer the research questions in this study, a carefully designed experiment based on the work of Boon et al. [24] is conducted. A core flood test for drainage and imbibition is carried out on an initially brine saturated Berea sandstone core (17 cm length and 3.8 cm in diameter), at 18 ° C and 100 bar, using a medical X - ray CT scanner to observe the gas/brine/rock system. In this section, the sample preparation and experimental procedure are explained.

3.1. Sample Preparation

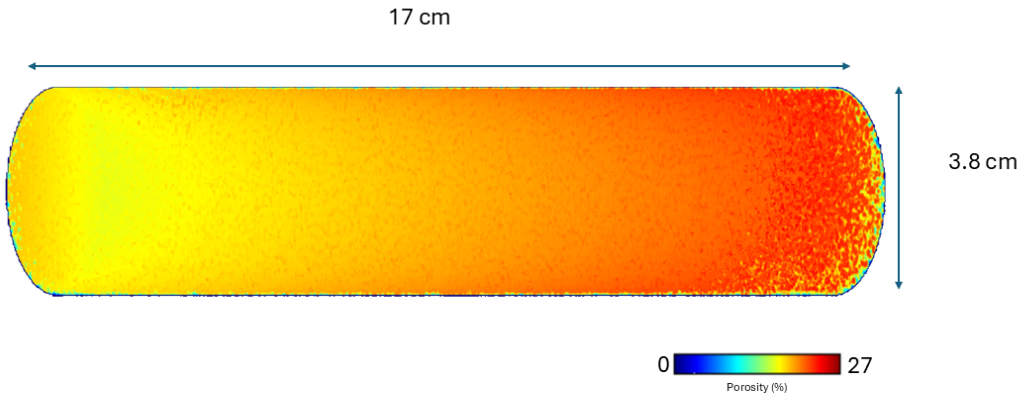

Figure 3.1: 3D porosity map of the core viewed from the outer surface of the core. Inlet left and outlet right end

An untreated Berea sandstone core, with a length of 17 cm and diameter of 3.8 cm is used in this experiment. The untreated sample is covered in a viscous mixture of adhesive (Rencast CW 47) and hardener (RWEN HY 33), and left to dry in a mold for 48 hours. This initial epoxy mixture acts as a barrier to prevent penetration of the second layer of resin applied later on to fix the core to the core holder. From CT imaging, it is observed that the resin only slightly penetrates the core. The diameter of the core was assumed to be 3.6 cm (rather than 3.8 cm) for the Kr calculations. The core is cut to 17 cm length using a water saw, after which the core is left in an oven for 6 hours to remove any water that could have seeped in. Once oven dried, two shower end caps are attached to PEEK (Polyetheretherketone) inlet and outlet tubing (high performance thermoplastic polymer which is stable in high temperature and high pressure environments), and glued onto the inlet and outlet of the core. Once the resin glue is dry, the core is placed in the core holder, and epoxy resin (L20) and hardener (EPH 161) are injected into

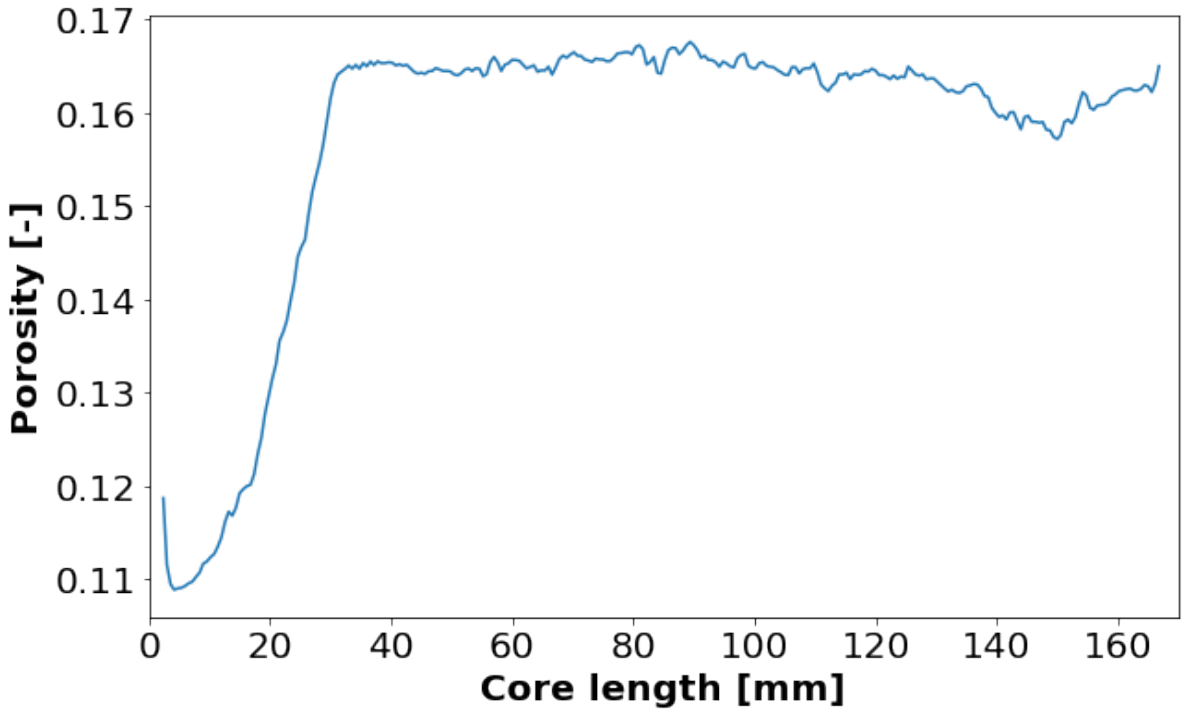

Figure 3.2: Slice average core porosity vs distance from inlet

the voids to seclude and attach the core with the PEEK core holder. Three holes are drilled into the core at a distance of 2.15, 8.5, and 14.75 cm from one end of the core (now called the inlet). The holes are vacuumed to remove any loose particles that may impede measurements.

3.2. Materials and Experimental Conditions

The experiments are carried out at 18 ° C and a pressure of 100 bar. Brine (1% w.t NaCl), H_2 gas, CH_4 gas, and a Berea sandstone rock core are used in the experiments. The H_2 and CH_4 gas are each of 99.99 mol% purity, and are supplied by the Linde gas Company. The absolute permeability (k) of the sample with respect to water is 83.2 mD ($8.32 \cdot 10^{-14}$ m^2) when considering the entire core length, and the porosity is 15.7%, corresponding to a pore volume of 30 ml. The porosity of the core is determined by using the slice mean average equation 3.1:

$$\phi = \frac{CT_{brine} - CT_{dry}}{I_{brine} - I_{air}} \tag{3.1}$$

Here, CT_{brine} and CT_{dry} are the voxel level CT numbers in houndsfield units (HU) for the brine and dry core, respectively, and I_{brine} and I_{air} are the CT values that would have been obtained if water and air alone were scanned [42]. From Figure 3.2 it is clear that towards the inlet of the core, there is a lower porosity zone, where porosity reaches as low as 11% compared to the remaining length of the core (16.3 %). This low porosity zone is clearly visible in Figure 3.1. The absolute permeability of the core with respect to water was measured with a pure water core flood at 100 bar pressure, injecting water at varying flow rates (5, 10 and 15 mlmin^{-1}), and calculated using Darcy's law for single phase flow of brine:

$$Q = \frac{Ak}{\mu} \cdot \frac{\Delta P}{L} \tag{3.2}$$

where Q is the injected flow rate (m3/s), A is the cross-sectional area of the core (m^2), K is the absolute permeability (m^2), μ is the viscosity of the fluid (Pa s) and ΔP is the pressure drop (Pa) over length

L (m). In this case, ΔP and L, were taken from the middle region of the core (21.5 mm - 147.5 mm) to calculate K. K was calculated using the pressure drop measured by the middle section differential pressure transducer (DP4), while L was 12.6 cm. This resulted in a K of 75.3 mD used for relative permeability calculations. This is distinct the total absolute permeability reported earlier a a different pressure drop and length are considered. The total injection rate of fluids is 5 mlmin^{-1}, corresponding to a superficial velocity (v) of $7.35 \cdot 10^{-5}$ ms^{-1} when taking the cross sectional core area as $\pi * (3.8/2) m^2$ and the flow rate as 0.000005 $m^3 min^{-1}$

At the experimental conditions, H_2, CH_4, their mixture, and water have differing properties as summarized in table 2.4. A complex interplay of viscous, capillary and gravitational forces is expected for the gas/water/rock system [24]. As discussed in section 2, the two-phase displacement behavior can lead to different flow regimes depending on the balance of these forces. In two phase displacement, flow behavior, in the absence of gravitational forces, can be characterized by the capillary number (Ca) and the viscosity ratio (M) [60].The capillary number and viscosity ratio for both drainage ($Ca_{drainage}$ and $M_{drainage}$), and imbibition 1 and 2 ($Ca_{imbibition}$ and $M_{imbibition}$), for each gas composition (see equations 2.4 and 2.5), are shown in table 3.1.

Based the work of Guo and Aryana [60], a capillary dominated regime will occur at values below Log Ca -6 and Log M 3, while viscous flow can occur at log Ca > -8, and log M > 2 - 3 (Figure 2.3). Hence, for both drainage and imbibition, given the range of Ca and M from table 3.1 the capillary fingering displacement regime can be expected for all gas compositions across the experiment. The capillary numbers were selected to be similar to previous studies (see table 2.1) to facilitate meaningful comparisons.

Gas	Capillary Number	Viscosity Ratio
Drainage		
Hydrogen	$9.0796 \cdot 10^{-9}$	118
Methane	$1.4728 \cdot 10^{-8}$	76.8
Mixture	$1.3387 \cdot 10^{-8}$	85.8
Imbibition 1/2		
Hydrogen	$1.0726 \cdot 10^{-6}$	0.0085
Methane	$1.2642 \cdot 10^{-6}$	0.0130
Mixture	$1.1510 \cdot 10^{-6}$	0.0116

Table 3.1: Capillary number and viscosity ratio for different gas compositions in the drainage and the imbibition stages. The imbibition values are the same for imbibition 1/2 as the only difference between them is the initial saturation (i.e total flow rate, viscosity and interfacial tension of the phases remains the same). The superficial velocity (5 mlmin^{-1}) was used to calculate capillary number

3.3. Experimental Apparatus

The experimental setup used in this study is based on the configuration described by Boon et al. [24]. A schematic representation of the setup is shown in Figure 3.3. Water and gas saturations within the core were quantified using an X-ray CT scanner. The scanner produced images with a slice thickness of 0.6 mm, and 0.19 mm in the other two dimensions, resulting in a voxel resolution of 0.19 x 0.19 x 0.6 mm^3. Scanning was performed at a voltage of 140 kV and a current of 250 mA. The mean average slice CT values are used in calculations to reduce random error in the CT number.

The set up forms a closed loop system to minimize risk of introducing nonequilibrated brine into the core. Pressure measurements were conducted at five locations along the length of the sandstone core to capture the pressure distribution during fluid injection. Two absolute pressure transducers (UNIK 5000 series) were installed at the inlet and outlet of the core holder, denoted as P1 and P2, respectively. These transducers measured the absolute pressure at the inlet and outlet of the core, respectively, and the total pressure drop across the core. To resolve the pressure gradient within the core, three differential pressure (DP) sensors (Deltabar S PMD75, Endress+Hauser) were installed at intermediate locations. These were positioned at 2.15 cm from the inlet (DP1), 14.5 cm from the inlet (DP4), and 2.25 cm from the outlet (DP5). This configuration enabled a high resolution assessment of the pressure

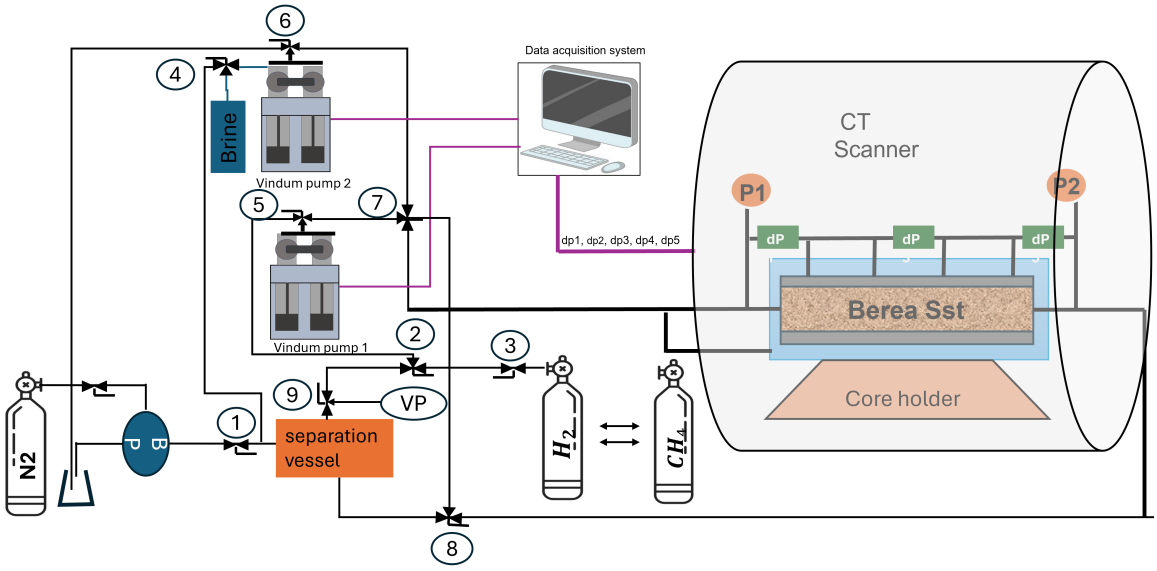

Figure 3.3: Experimental set up schematic diagram

gradient and facilitated the detection of potential heterogeneities within the porous medium. All sensors were calibrated prior to the experiments to ensure measurement accuracy and reliability. To ensure continuous and pulse free injection of fluids, two high precision Vindum pumps were used in paired rate delivery (PRD) mode; one for gas connected to a gas cylinder and one for 1% NaCl brine connected to a brine container. These pumps offer a flow accuracy of 0.1% [102], and a total volume of 20 ml (10 ml per piston) The core inlet and outlet were equipped with shower head end caps to promote uniform gas distribution across the core ends. The effluent was collected in a 150 mL separation vessel. The top of this vessel was connected to the gas pump, allowing for gas recirculation and the establishment of a closed loop system. The bottom of the vessel was connected to a back pressure regulator, which maintained the system pressure at 100 bar via a nitrogen gas cylinder. The system volume, comprised of the tubing (3.5 ml), separation vessel (150 ml), pumps (20 ml), and the pore volume of the sandstone core (31 ml), is 204 ml. Upon completion of an experiment, the effluent brine was collected in a separate bottle connected to the bottom of the separation vessel.

Safety protocols were strictly followed throughout the experiment. A gas monitor was installed in the CT room to detect any gas leakage. The H_2/CH_4 gas cylinder remained closed at all times except during the filling of the gas pump. The experiment was conducted in a well ventilated room. When depressurizing the system after each experiment, the gas was released to a fume hood, ensuring safe discharge of H_2.

3.4. Experimental procedure

The steady state technique was used in this experiment, where both the wetting and non-wetting phases were coinjected into the core sample at differing fractional flow rates. Steady state was considered achieved when the differential pressure between the inlet and outlet of the core remained constant. Once steady state was reached, scans of the core were taken using the X-ray CT scanner. The experiment was repeated for pure H_2, pure CH_4, and a 50-50% molar H_2/CH_4 mixture. As detailed below, the experimental procedure consisted of four main stages: (1) background scans and absolute permeability test, (2) drainage relative permeability measurements, (3) drainage capillary pressure measurements, and (4) imbibition relative permeability measurements.

Reference Scans and Absolute Permeability Test

To begin the experiment, background scans were taken of the dry core saturated with air at ambient pressure. The core was then connected to a vacuum pump to evacuate the air. Once under vacuum, the core was saturated with H_2 at 100 bar. This was achieved by injecting H_2 while slowly increasing the back pressure to the experimental pressure of 100 bar. Once the desired pressure was reached, a background scan of the H_2 saturated core was taken. Afterwards, the pressure was reduced to ambient conditions, and the H_2 was vented into the fume hood. The system was then flushed with CO_2 to ensure the H_2 had been flushed from the core. Brine (1% NaCl) was injected at the inlet, while the outlet remained connected to the vacuum pump. When water reached the outlet, the outlet lines were connected to the back pressure regulator, and the pressure was slowly increased to 100 bar. Background scans of the brine saturated core were taken. At least 5 pore volumes (PV) of brine were injected to ensure full saturation.

The flow rate of water was then increased from 1 mlmin^{-1}, to 5 mlmin^{-1}, and then 15 mlmin^{-1}, for 5 minutes at a time, and then step wise brought to 5 mlmin^{-1}, then 1 mlmin^{-1}. The pressure across the core was recorded and used in equation 3.2 with the corresponding flow rates, which were averaged to find the absolute permeability.

Following this, the core was bypassed by closing valves 7 and 8, while valves 2 and 4 were directed to the separation vessel to allow fluid recirculation. Gas and brine were co-injected using both pumps at a total flow rate of 10 mlmin^{-1} for 40 minutes to pre-equilibrate the phases. Subsequently, valves 7 and 8 were opened , and the gas pump switched off, so that the equilibrated brine could be injected into the core. The total circulated fluid volume (400 mL) was significantly larger than the system volume (204 mL), ensuring the core was fully saturated. A background scan was taken of the equilibrated brine msaturated core. This scan served as the baseline for the first drainage relative permeability measurement, corresponding to 0% gas and 100% brine saturation.

Relative Permeability and Imbibition Tests

After all background scans were taken, a total flow rate of 5 mlmin^{-1} was established, with the fractional flow of gas stepwise increased from 0 to 100%. Once steady state was reached ($\Delta P_{\text{core}} = 0$), CT scans of the core were taken (approximately 2 hours after setting the new flow rate). The steady state relative permeability of both phases was calculated using the extended Darcy's law (Equation 2.1). The near final steady state point of the drainage process marked the endpoint relative permeability ($K_{r,\text{end}}$) at a gas fractions flow rate of 0.99. This was due to channeling observed in the last drainage step. The final drainage point however (fractional flow of 1) served as the first capillary pressure measurement. Relative permeability curves are typically plotted as a function of wetting phase (brine) saturation (S_w). Saturation was determined using equation 3.3:

$$S_w = \frac{CT_{\text{exp}} - CT_{\text{gas}}}{CT_{eqbrine} - CT_{\text{gas}}} \tag{3.3}$$

where CT_{exp} represents voxel level CT number (HU) from the current experimental step, and CT_{gas} and $CT_{eqbrine}$ represent the CT numbers of the gas saturated and the equilibrated brine saturated cores, respectively. Fractional flows and experimental conditions used during drainage measurements are reported in tables 3.2, 3.3 3.4. Since saturation and pressures varied across the core in different experiments (see Figures 4.1 4.2, and 4.3), the average S_w values in the central region of the core (21.5 - 147.5 mm), where saturation is more uniform, were used. This also reduced the effect of end effects, which would lead to inaccuracies in the calculated relative permeabilities [103]. Pressure drops recorded by the middle pressure differential transducer (DP4) are used for relative permeability calculations as they correspond to this range (21.5 - 147.5 mm).

Capillary Pressure Measurements

The capillary pressure measurement method followed the approach described by Pini et al [66]. In this approach it is noted that once steady state is assumed there is no more net water production from the end of the core, so water pressure throughout the core can be assumed to be constant. The latter is true if the water forms a continuous phase across the core, which is a reasonable assumption for a (strongly) water wet core [66]. The pressure gradient in the core is maintained by the non-wetting phase and at each point in the core the pressure difference between the wetting and the non-wetting phase equals

the capillary pressure as in equation 2.2. The pressure of the wetting phase is assumed continuous at the outlet, while the non-wetting phase may not be continuous, allowing the assumption that at the outlet, the outlet pressure equals the water pressure. Hence, regardless of the value of the capillary pressure at the outlet, the pressure drop from any point in the core to the outlet corresponds to the capillary pressure at that location along the core. Figure 3.4 illustrates the situation. By increasing the non-wetting phase flow rate s capillary pressure measurement at various wetting phase saturations can be obtained.

In this experiment, the water pressure is measured at the outlet, and the gas pressure at the inlet and the three intermediate pressure taps located at 2.25, 8.5, and 14.45 cm from the core inlet. Following the final drainage relative permeability test, the gas flow rate was increased in steps from 5 mlmin^{-1} to 7, 10, 20, and 30 mlmin^{-1} for the H_2 and CH_4 experiments, and 5, 10, and 30 mlmin^{-1} for the mixture experiments. As in the relative permeability tests, once steady state was achieved at each step, the average slice saturation of the core at that step in the experiment was calculated using equation 3.3. The final capillary pressure measurement at a flow rate of 30 mlmin^{-1} corresponds to the irreducible brine saturation (S_{wi}). Ultimately, the pressure drop between 147.5 - 170 mm away from the core inlet was used for capillary measurements. This was to facilitate comparison with Boon et al. [24]), who used a similar region.

The capillary pressures obtained by following this method vary depending on where measurements are made. The pressure transducers along the core reveal that the change in pressure is not linear, with average pressures near the inlet being lower than the middle of the core (21.5 - 147.5 mm) and much higher towards the outlet (147.5 - 170 mm). The substantially higher pressure recorded at the outlet are attributed to capillary end effects, which can lead to substantial inaccuracies in results [103]. Due to this the measurements obtained by DP5 (which recorded the pressure drop across the 147.5 - 170 mm region of the core), was not used for capillary pressure measurements at the outlet. The capillary pressure was instead measured by subtracting the average pressure drop recorded by DP3 and DP4 pressure transducers from the absolute inlet pressure (P1), and subtracting the outlet pressure (P2) from this result. For more detail on the exact pressures obtained when using different regions of the core, refer to Appendix C.

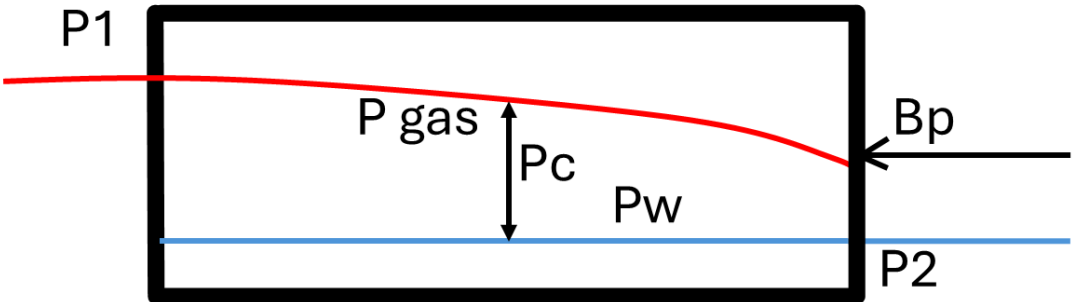

Figure 3.4: Graphical representation of the technique used to measure capillary pressure in this study. P_{gas} is the partial pressure of the gas phase, P_w is the partial pressure of the water phase, P1 and P2 are the inlet and outlet pressure, respectively, and Bp is the back pressure. Adapted from [66]

Imbibition Relative Permeability Experiments

The imbibition experiments followed a similar procedure to the drainage experiments but started from 100% gas fractional flow. Two sets of imbibition measurements were performed to obtain data from different initial gas saturations. In the first set (Imbibition 1), the last point of the drainage capillary pressure measurements served as the starting point for imbibition. For the second set (Imbibition 2), 100% gas was injected into the brine saturated core following the final imbibition step from Imbibition 1 (i.e fractional brine flow of 100%) at 5 mlmin^{-1} until steady state was reached. This resulted in a lower initial gas saturation (S_{gi}) for the second imbibition phase compared to the first.

Similar to the drainage tests, once steady state was achieved, the relative permeability was calculated

using Equation 2.1, and saturation was calculated using Equation 3.3. The fractional flow of brine was increased stepwise until 100% brine flow was reached, achieving a range of saturations. Experimental conditions and fractional flows used in the imbibition tests are also reported in tables 3.2 3.3 3.4.

Gas type was changed by replacing the gas cylinders and controlling the volume of residual gas in the system of the previous experiment through depressurizing the system. The gas type procedure, along with some notable experimental errors are described in Appendix A. Furthermore, discussion on the confidence that the gas mixture achieved was a 50-50% molar mix of H_2 and CH_4 is provided on Appendix B

Step	Q [ml/ min]	f_{H_2}	f_w	q_{H_2} [ml/ min]	q_{brine} [ml/ min]	K_{rBrine}	$K_{r_{H_2}}$	$S_{w,\text{avg}}$	ΔP_{mid} [bar]	ΔP_{total} [bar]	P_c [bar]	S_w (Pc)
Drainage – Hydrogen												
1	5	0	1	0	5	–	–	1	–	–	–	–
2	5	0.2	0.8	1	4	0.81*	0.0018*	0.733	1.20	2.17	–	–
3	5	0.3	0.7	1.5	3.5	0.7525*	0.0029*	0.731	1.15	1.96	–	–
4	5	0.4	0.6	2	3	0.0977	0.0006	0.753	7.59	11.3	–	–
5	5	0.5	0.5	2.5	2.5	0.0802	0.0007	0.746	7.71	11.4	–	–
6	5	0.7	0.3	3.5	1.5	0.0759	0.0016	0.731	4.90	8.11	–	–
7	5	0.8	0.2	4	1	0.0638	0.0023	0.718	3.73	6.10	–	–
8	5	0.9	0.1	4.5	0.5	0.0806	0.0064	0.719	1.53	2.90	–	–
9	5	0.95	0.05	4.75	0.25	0.105	0.0177	0.708	0.594	1.66	–	–
10	5	0.99	0.01	4.95	0.005	0.0454	0.0399	0.673	0.276	0.638	–	–
11	5	1	0	5	0	0	0.134	0.606	0.084	0.385	–	–
Capillary Pressure - Hydrogen												
1	5	1	0	5	0	0	0.134	0.606	0.084	0.385	0.405	0.606
2	7	1	0	7	0	0	0.1936	0.598	0.082	0.220	0.221	0.598
3	10	1	0	10	0	0	0.2564	0.584	0.091	0.239	0.238	0.581
4	15	1	0	15	0	0	0.275	0.571	0.122	0.296	0.287	0.571
5	20	1	0	20	0	0	0.3252	0.571	0.135	0.286	0.291	0.572
6	30	1	0	30	0	0	0.3854	0.534	0.173	0.356	0.346	0.534
Imbibition - Hydrogen												
1	30	1	0	30	0	0	0.0642	0.534	0.173	0.356	–	–
2	5	0.99	0.01	4.95	0.05	0.0309	0.0272	0.645	0.405	0.597	–	–
3	5	0.95	0.05	4.75	0.25	0.0341	0.0058	0.646	1.72	2.36	–	–
4	5	0.9	0.1	4	1	0.0373	0.003	0.672	3.29	4.20	–	–
5	5	0.8	0.2	3.5	1.5	0.0405	0.0014	0.678	6.07	7.87	–	–
6	5	0.7	0.3	2.5	2.5	0.0408	0.0008	0.683	9.11	12.0	–	–
7	5	0.5	0.5	1.5	3.5	0.0386	0.0003	0.683	15.8	20.1	–	–
8	5	0.3	0.7	1	4	0.0448	0.0002	0.688	19.3	24.6	–	–
9	5	0.2	0.8	0	5	0.0507	0.0001	0.692	19.9	24.9	–	–
Imbibition - 2 - Hydrogen												
1	5	1	0	5	0	0	0.28	0.548	0.037	0.171	–	–
2	5	0.99	0.01	4.95	0.05	0.0205	0.018	0.610	0.606	0.679	–	–
3	5	0.95	0.05	4.75	0.25	0.0283	0.0048	0.636	2.23	2.83	–	–
4	5	0.9	0.1	4.5	0.5	0.0302	0.0024	0.647	4.10	5.153	–	–
5	5	0.8	0.2	4	1	0.0295	0.001	0.655	8.23	10.1	–	–
6	5	0.7	0.3	3.5	1.5	0.037	0.0008	0.661	9.60	12.0	–	–
7	5	0.5	0.5	2.5	2.5	0.04	0.0004	0.680	15.1	19.0	–	–
8	5	0.3	0.7	1.5	3.5	0.0439	0.0002	0.690	19.3	24.4	–	–
9	5	0.2	0.8	1	4	–	–	0.691	–	–	–	–
10	5	0	1	0	5	0.2502	0	0.786	5.05	8.53	–	–

Table 3.2: Experimental steps with fractional flow parameters: relative permeability, saturation, and capillary pressure for Hydrogen. The saturations shown are the average saturations of the middle region (21.5 - 147.5 mm) of the core. ΔP_{mid} is the pressure drop across the middle of the core (21.5 - 147.5 mm). * The kr values corresponding to drainage at f_g = 0.2 and f_g0.3 exceeded the original pressure transducer pressure range (6 bar). The pressure drops for these kr values were instead calculated by realizing that the pressure drop (P1 - P2) should be the same as the sum of the DP transducers along the core (DP3 + DP5 + DP4), and rearranging to solve for the DP4. The explanation of the error is given in Appendix A .

Step	Q [ml/ min]	f_{H_2}	f_w	q_{H_2} [ml/ min]	q_{brine} [ml/ min]	K_{rBrine}	$K\_r_{CH_4}$	$S_{w,\{avg}$	DP_{mid} [bar]	ΔP_{total} [bar]	P_c [bar]	S_w (Pc)
Drainage - Methane												
1	5	0	1	0	5	0.8498	0	1	1.31	2.15	–	–
2	5	0.2	0.8	1	4	0.0797	0.0003	0.755	12.5	17.3	–	–
3	5	0.3	0.7	1.5	3.5	0.0739	0.0004	0.746	11.7	16.3	–	–
4	5	0.4	0.6	2	3	0.0669	0.0006	0.737	11.1	15.0	–	–
5	5	0.5	0.5	2.5	2.5	0.0557	0.0007	0.722	11.1	15.0	–	–
6	5	0.7	0.3	3.5	1.5	0.0454	0.0014	0.709	8.56	11.6	–	–
7	5	0.8	0.2	4	1	0.0406	0.0022	0.698	6.21	8.42	–	–
8	5	0.9	0.1	4.5	0.5	0.0371	0.0046	0.683	3.37	4.70	–	–
9	5	0.95	0.05	4.75	0.25	0.0355	0.0092	0.67	1.76	2.46	–	–
10	5	0.99	0.01	4.95	0.05	0.0265	0.034	0.64	0.584	0.903	–	–
11	5	1	0	5	0	0	0.316	0.570	0.054	0.202	–	–
Capillary Pressure – Methane												
1	5	1	0	5	0	0	0.3147	0.570	0.054	0.202	0.139	0.57
2	7	1	0	7	0	0	0.3188	0.561	0.077	0.233	0.222	0.561
3	10	1	0	10	0	0	0.7243	0.513	0.050	0.196	0.187	0.513
4	15	1	0	15	0	0	0.6176	0.507	0.084	0.290	0.238	0.507
5	20	1	0	20	0	0	0.6308	0.500	0.116	0.300	0.269	0.500
6	30	1	0	30	0	0	0.6056	0.495	0.171	0.369	0.334	0.495
Imbibition – Methane												
1	5	1	0	5	0	0	0.1006	0.495	0.171	25.4	–	–
2	5	0.99	0.01	4.95	0.05	0.023	0.0312	0.621	0.544	25.5	–	–
3	5	0.95	0.05	4.75	0.25	0.0256	0.0067	0.63	2.37	21.9	–	–
4	5	0.9	0.1	4.5	0.5	0.0279	0.0034	0.651	4.48	16.9	–	–
5	5	0.8	0.2	4	1	0.0297	0.0016	0.664	8.19	10.7	–	–
6	5	0.7	0.3	3.5	1.5	0.0281	0.0009	0.663	12.7	5.95	–	–
7	5	0.5	0.5	2.5	2.5	0.0376	0.0005	0.677	16.6	3.20	–	–
8	5	0.3	0.7	1.5	3.5	0.0513	0.0003	0.683	17.0	0.792	–	–
9	5	0.2	0.8	1	4	0.0586	0.0002	0.689	17.0	0.370	–	–
Imbibition - 2 – Methane												
1	5	1	0	5	0	0	0.1315 *	0.498	0.131	0.150	–	–
2	5	0.99	0.01	4.95	0.05	0.0233	0.6197	0.659	0.532	0.838	–	–
3	5	0.95	0.05	4.75	0.25	0.0234	0.6331	0.659	2.65	3.52	–	–
4	5	0.9	0.1	4.5	0.5	0.028	0.0034	0.645	4.46	5.94	–	–
5	5	0.8	0.2	4	1	0.0252	0.0014	0.649	9.88	12.8	–	–
6	5	0.7	0.3	3.5	1.5	0.0295	0.0009	0.659	12.7	15.8	–	–
7	5	0.5	0.5	2.5	2.5	0.0364	0.0005	0.670	16.8	21.7	–	–
8	5	0.3	0.7	1.5	3.5	0.0411	0.0002	0.679	21.0	26.8	–	–
9	5	0.2	0.8	1	4	0.048	0.0001	0.687	21.0	26.3	–	–
10	5	0	1	0	5	0.2994	0	0.822	4.17	7.47	–	–

Table 3.3: Experimental steps with fractional flow parameters: relative permeability, saturation, and capillary pressure for pure methane. The saturations shown are the average saturations of the middle region (21.5 - 147.5 mm) of the core. ΔP_{mid} is the pressure drop across the middle of the core (21.5 - 147.5 mm). * The pressure drop recorded by DP4 for this measurement resulted in a negative kr value. The pressure drop was instead calculated by realizing that the pressure drop (P1 - P2) should be the same (if not similar due to error) as the sum of the DP transducers along the core (DP3 + DP5 + DP4), and rearranging to solve for the DP4.

Step	Q [ml/ min]	$f_{mixture}$	f_{brine}	$q_{mixture}$ [ml/ min]	q_{brine} [ml/ min]	K_{rBrine}	$K_{r_{mixture}}$	$S_{w,\text{avg}}$	ΔP_{mid} [bar]	ΔP_{total} [bar]	P_c [bar]	S_w (Pc)
Drainage – Mixture												
1	5	0	1	0	5	0.38	0	0.868	3.34	6.54	–	–
2	5	0.2	0.8	1	4	0.0909	0.0002	0.775	10.9	16.1	–	–
3	5	0.5	0.5	2.5	2.5	0.064	0.0007	0.743	9.70	13.7	–	–
4	5	0.8	0.2	4	1	0.0523	0.0022	0.721	4.71	6.80	–	–
5	5	1	0	5	0	0	0.356	0.543	0.046	0.167	–	–
Capillary Pressure – Mixture												
1	5	1	0	5	0	0	0.356	0.543	0.046	0.167	0.180	0.543
2	10	1	0	10	0	0	0.1166	0.538	0.221	0.235	0.202	0.538
3	30	1	0	30	0	0	0.4287	0.53	0.178	0.469	0.415	0.530
Imbibition – Mixture												
1	30	1	0	30	0	0	0.4287	0.530	0.178	0.469	–	–
2	5	0.8	0.2	4	1	0.0371	0.0015	0.674	6.58	9.11	–	–
3	5	0.5	0.5	2.5	2.5	0.0422	0.0004	0.694	14.7	19.69	–	–
4	5	0.2	0.8	1	4	0.0586	0.0002	0.692	17.0	27.7	–	–
5	5	0	1	0	5	0.6909	0	0.927	3.35	4.32	–	–

Table 3.4: Experimental steps with fractional flow parameters: relative permeability, saturation, and capillary pressure for the $H2/CH_4$ mixture. The saturations shown are the average saturations of the middle region (21.5–147.5 mm) of the core. ΔP_{mid} is the pressure drop across the middle of the core (21.5 - 147.5 mm).

4

Results and Discussion

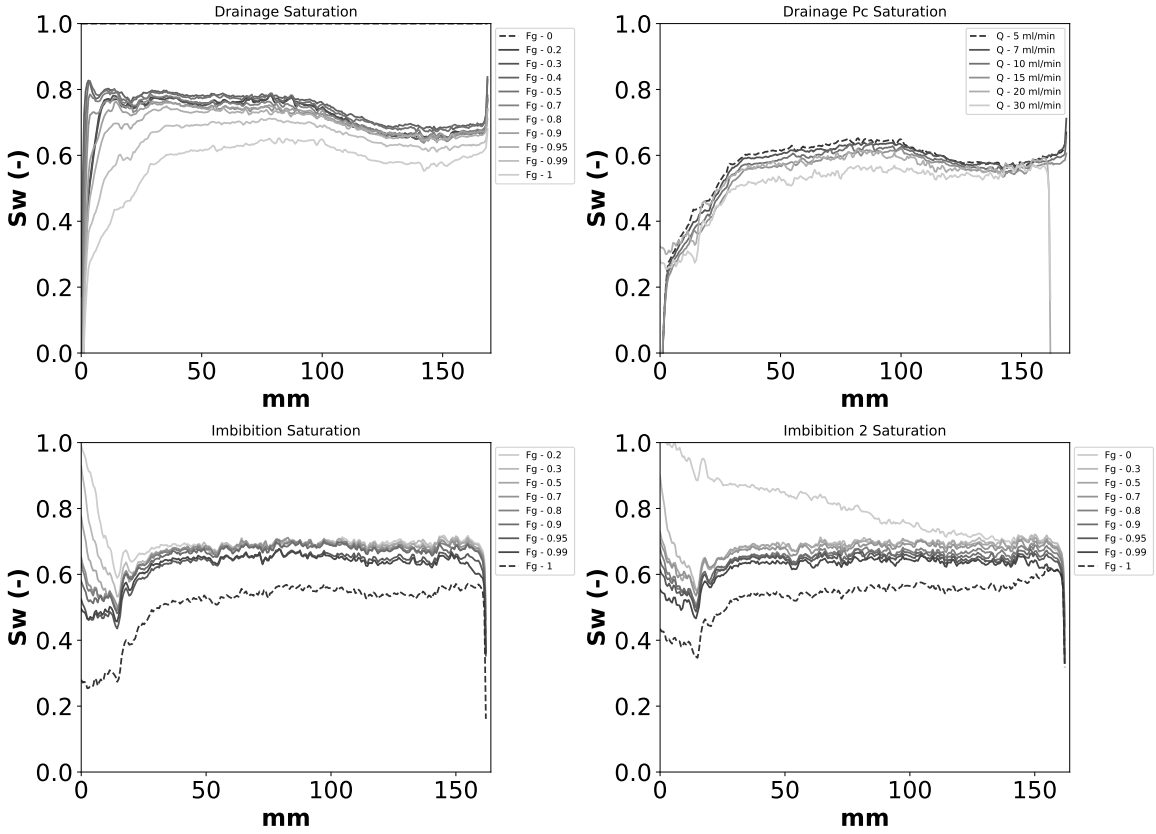

Figure 4.1: steady state saturation profiles along the length of the core for the hydrogen gas experiment. Each subplot indicates a different stage of the experiment. Top left Drainage relative permeability measurements. Top right: Drainage capillary pressure measurements. Bottom left/right: Imbibition relative permeability measurements for Imbibition 1 and Imbibition 2, respectively. The dotted line in each subplot indicates the starting point saturation for that experiment. Numbers in the legend refer to gas fractional flow rate ($F_g - 0.2$ is 20% H_2 flow and 80% brine flow)

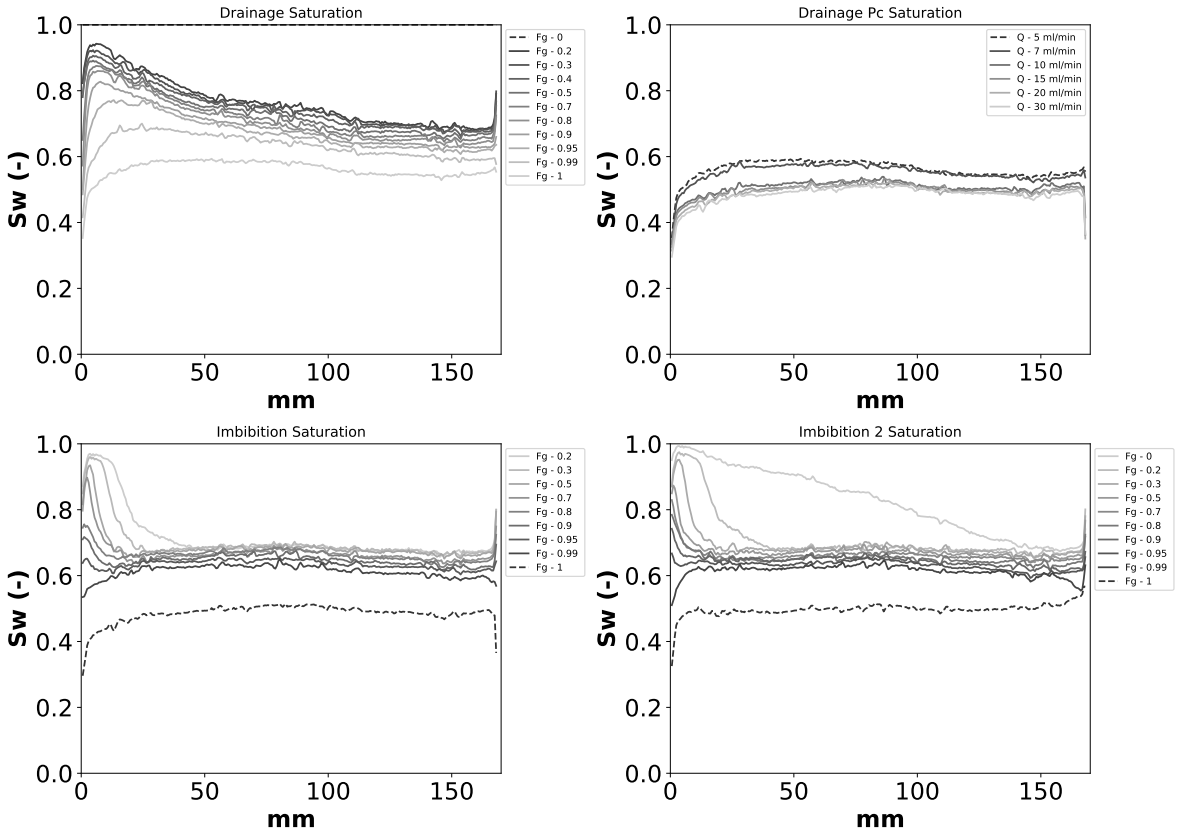

Figure 4.2: steady state saturation profiles along the length of the core for the pure methane gas experiment.Each subplot indicates a different stage of the experiment. Top left Drainage relative permeability measurements. Top right: Drainage capillary pressure measurements. Bottom left/right: Imbibition relative permeability measurements for Imbibition 1 and Imbibition 2, respectively. The dotted line in each subplot indicates the starting point saturation for that experiment. Numbers in the legend refer to gas fractional flow rate ($F_g - 0.2$ is 20% CH_4 flow and 80% brine flow).

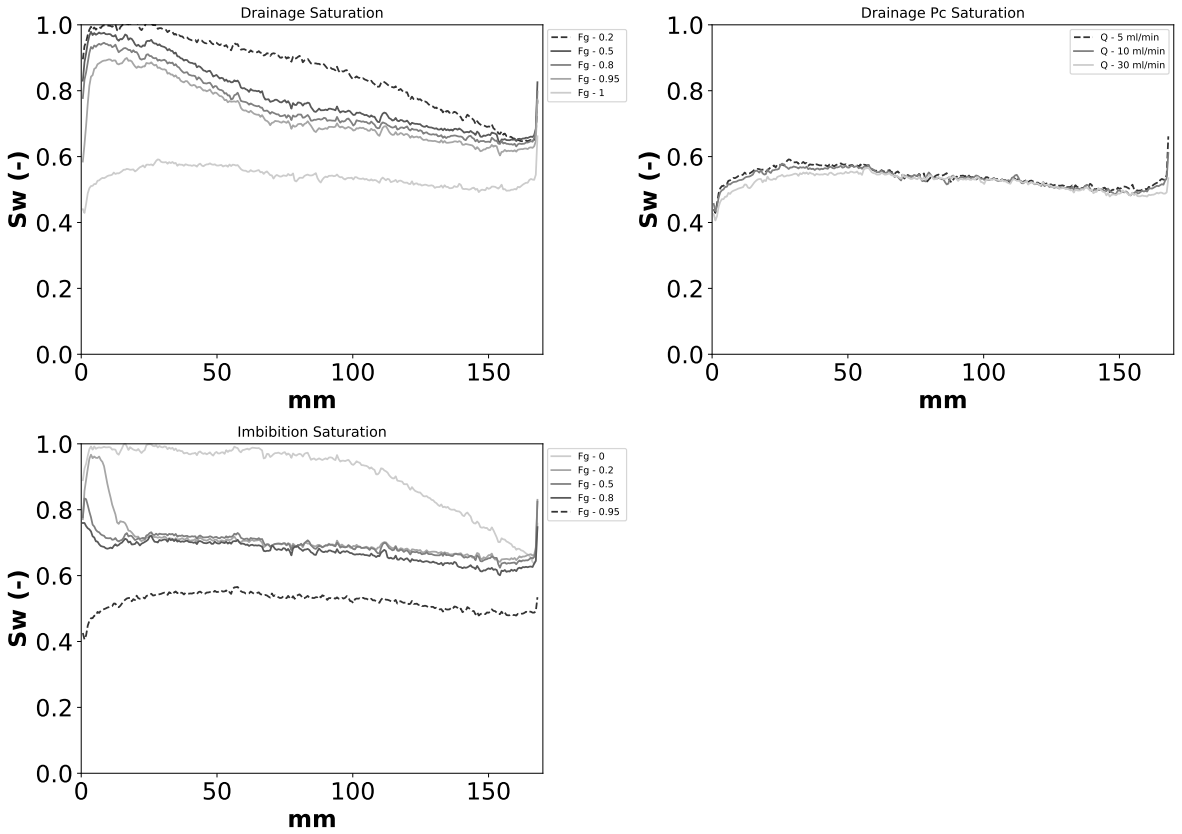

Figure 4.3: steady state saturation profiles along the length of the core for the 50-50 % hydrogen/methane mixture. Each subplot indicates a different stage of the experiment. Top left Drainage relative permeability measurements. Top right: Drainage capillary pressure measurements. Bottom left: Imbibition relative permeability measurements for Imbibition 1. Imbibition 2 was not conducted for the mixture. The dotted line in each subplot indicates the starting point saturation for that experiment. Numbers in the legend refer to gas fractional flow rate (F_g − 0.2 is 20% gas flow and 80% brine flow)

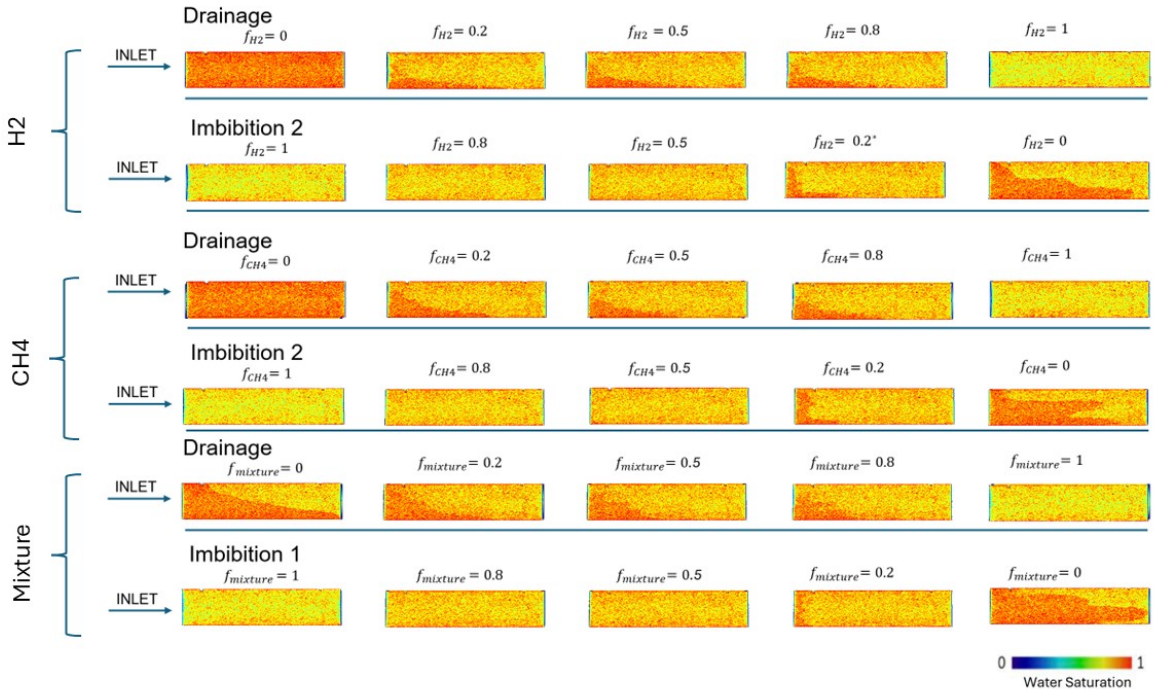

Figure 4.4: Steady state 3D saturation maps for various steps during drainage and imbibition 2 for Hydrogen (Top), methane (Middle), and the mixture (Bottom), represented as cross sectional views from the middle of the core along the inlet to outlet dimension. Note $f_{H2} = 0.2$ is missing in imbibition 2 as the gas pump had exceeded the safety pressure and turned off before steady state was reached. The corresponding image at $f_{H2} = 0.2$ during the imbibition 1 stage of hydrogen was shown in its place. f_{H2} , f_{CH4} , and $f_{Mixture}$ represent the fractional flows of Hydrogen, Methane, and the 50-50% mixture, respectively.

4.1. Saturation and flow behavior

The steady state slice averaged saturation profiles for H_2, CH_4 and their mixture measured along the core length during the drainage, Pc drainage, first imbibition, and second imbibition stages are shown in Figures 4.1, 4.2, and 4.3. As the gas fractional flow (f_g) increases, the slice average brine saturation (S_w) decreases across the sample for all gases. For H_2 and CH_4, S_w varies between 0.53 and 1, and 0.49 and 1, respectively. Brine saturations varied from 0.87 to 0.53 for the mixture. The lower initial brine saturation for the mixture is the result of gas initially in place during the first drainage step corresponding to $f_g = 0$. Despite the brine pump being left to saturate the core for over 23 hours at a flow rate of 5 ml/min (228 PV), image visualization showed that residual CH_4 from the previous experiment was present in the core. This is clearly seen in Figure 4.3 where the drainage saturation profile for $f_g = 0$ is substantially lower than 1 at lengths greater than 40 mm.

The first brine saturated core scan in drainage served as the equilibrated brine scan used in equation 3.3 for each gas composition. As a result of the residual gas in place in the core during the initial mixture drainage step, the mixture equilibrated brine scan was taken as the CH_4 equilibrated brine scan. When comparing the H_2, CH_4 and mixture CT equilibrated scans, the CT voxel values were similar (within 6 HU), so the resulting difference in the calculated S_w values is expected to be minimal.

S_w tends to be elevated near the inlet (within the first 30 mm from the inlet) and gradually decreases down core across drainage experiments. This could be the result of gas dissolution and rock structure. Despite extensive recirculation outside the core to pre-equilibrate the brine and gas phases, a mismatch between the pre-equilibration pressure (100 bar) and the inlet pressure during drainage would create a pressure gradient across the core [13]. According to Henry's Law, gas solubility is proportional to its partial pressure; as this pressure drops, dissolved gas may come out of solution forming disconnected ganglia that displace brine, lowering S_w further down core [13]. Furthermore, this effect may be amplified by ripening dynamics. As described by Gao et al. [81], despite pre - equilibration of brine with the gas at experimental conditions, once in the core, gasses will experience locally higher pressure at the pore scale than the bulk due to varying Pc. This means that unlike the bulk of the fluid, within small pores with comparatively elevated pressures, the brine may be undersaturated with gas, allowing more gas to dissolve than expected from the set experimental conditions. In parallel, as illustrated by Figure 3.1, the rock porosity increases from 11% near the inlet to 16.3% at 30 mm down core. This could suggest an increase in pore size, in which case the Pc would decrease and allow gas to come out of solution. A combination of these factors may have lead to the sloping saturation profiles observed throughout drainage experiments and across all gas types.

Perplexingly, the saturation profiles for both the CH_4 and the mixture near the inlet (within 30 mm of the inlet) show an even higher S_w than for H_2. Both CH_4 and the mixture are denser and exhibit lower IFT with the brine/rock system compared to H_2. This should, in theory, allow them to more effectively displace brine as they require lower Pc to enter the same pore space. While the Pc measured for H_2 (0.61 bar at 5 ml/min) is slightly higher than that of CH_4 (0.57 bar at 5 ml/ min), CH_4 is more soluble in brine than H_2 across a range of pressures [79]. This means that near the inlet, where porosity is lower and local pore pressures are likely higher than the bulk pressure of the core, more CH_4 than H_2 would dissolve in the brine, increasing the apparent S_w. The effect is noticeably more pronounced in the mixture, with S_w reaching > 0.9 within the first 10 mm of the inlet for f_g > 0.5. This may be a result of the higher Pc measured for the mixture (ranging from 0.18 - 0.41 bar at $f_g = 1$ and flow rates $Q = 5$ ml/min to 30 ml/min), though the exact values of these capillary pressures are subject of the location in the core they are measured and experimental errors (see Appendices A and C). As dissolved gas travels down core, the bulk pressure of the core decreases permitting the gas to exsolve, lowering S_w down core.

Focusing on the 3D saturation maps in Figure 4.4, during the last step of imbibition $f_g = 0$, the brine and gas phases are noticeably segregated for all gasses, though slightly less for CH_4 and the mixture compared to H_2. This is a direct result of the large density difference between H_2 (7.85 kg/m^3), CH_4 (79.31 kg/m^3), the mixture (61.56 kg/m^3)), and brine (1003.1kg/m^3). Nevertheless, at $f_g \leq 1$ there does not appear to be significant gas brine segregation throughout the bulk of the core, from which the kr measurements are made, indicating that representative flow parameters of the multiphase system can be derived [24].

Looking at Figure 4.4 more closely, there is a sudden increase in S_w for all gases at $f_g = 0.2$ to $f_g = 0$ during imbibition. At $f_g = 0.2$ the formation of fingers can be observed as areas of higher water saturation across the height of the inlet of the core. Dissolution of gas would contribute to the formation of highly water saturated fingers [24]. However, fingers are not observed in the scans at $f_g > 0.2$, indicating dissolution was minimal, possibly because the brine and gas were already well equilibrated. More likely, the fingers are a result of changing flow regime. When the fractional brine flow (f_w) is higher, capillary number becomes much larger, and as a result flow becomes more viscous dominated, and the mobility ratio much higher [92]. This, in conjunction with a potentially decreasing homogeneous permeability field for the brine dispersive front at each step of imbibition due to partial dissolution of gas into brine, adds to the likelihood of an unstable displacement front to form, where the formation of fingers is promoted [24, 104]. When the brine fractional flow increases further, the kr of brine increases in these fingers, resulting in the eventual formation of channels as seen in Figure 4.4 at imbibition 2 $f_g = 0$. This is similar to the behavior observed by Boon et al. [24]. Here water is now preferentially flowing through the channel rather than across the entire pore space, and meaningful multiphase parameters can not be derived at this point. Consequently, the kr for both gas phase and the brine phase can not be considered valid during the last stage of both imbibition 1 and imbibition 2.

Furthermore, Figure 4.4 shows that a substantial volume of gas was present in the bulk of the core during the first mixture drainage step ($f_g = 0$). This can be explained through experimental error. The gas pump was left open during the last imbibition step of the CH_4 experiment (imbibition - 2 $f_g = 0$). Due to this CH_4 was able to migrate from the pump into the core, leaving excess gas in the core by the end of CH_4 imbibition 2. Notably, CH_4 may have had a higher end point S_w if additional gas had not been continuously flooding into the core during this step. The excess gas may also explain why the highest imbibition S_w for CH_4 was merely 0.82, while for the mixture it was 0.92, despite CH_4 having properties that would indicate higher efficiency when sweeping the core, such as lower IFT, and higher viscosity and density.

4.2. Relative permeability and capillary pressure

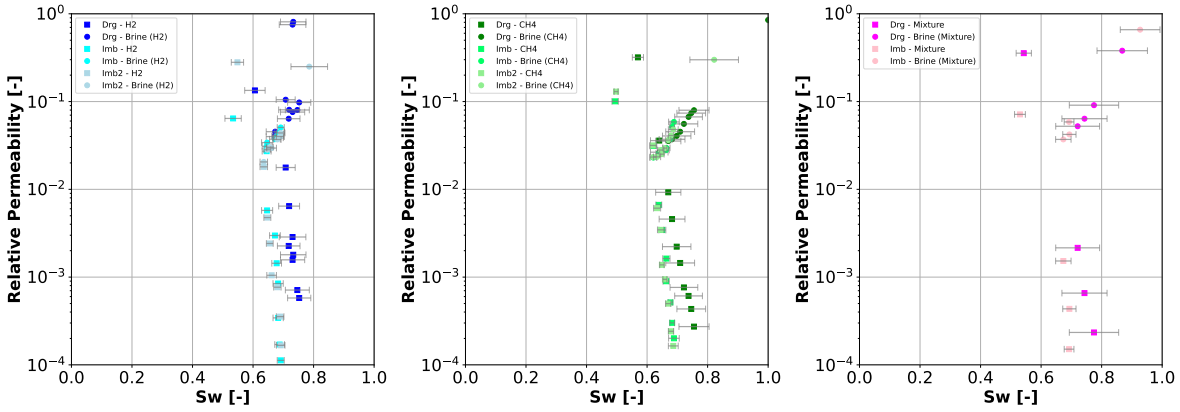

Figure 4.5: Relative permeability curves for drainage, first imbibition, and second imbibition. Circles: Water relative permeability points, squares: Gas relative permeability points. Each graph represents a different experiment: (Left) hydrogen, (Middle) methane, and (Right) the mixture. Error bars represent the absolute error

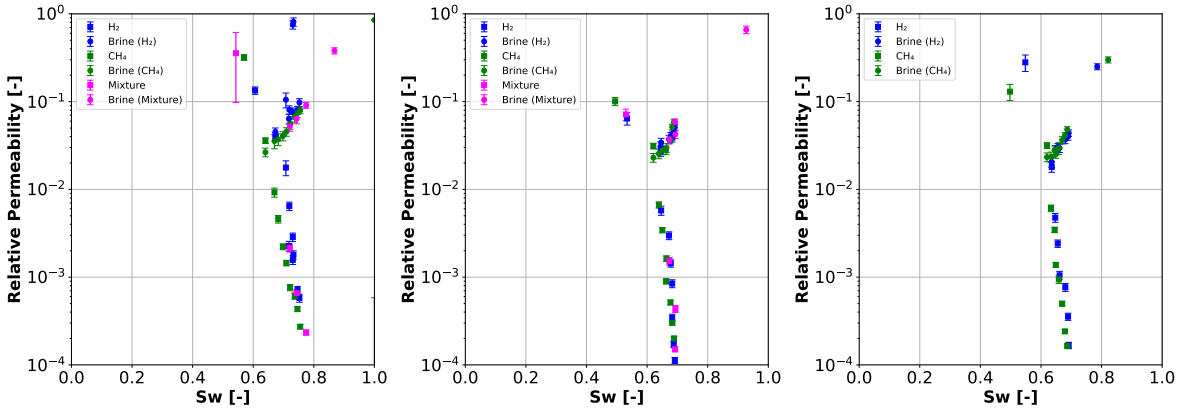

Figure 4.6: Relative Permeability curves for drainage and imbibition. Circles: Water relative permeability points, squares; Gas phase relative permeability. Each subplot corresponds to a different stage in the experiment: Drainage (Left), Imbibition (Right), and Imbibition 2 (Middle). Error bars represent the absolute error

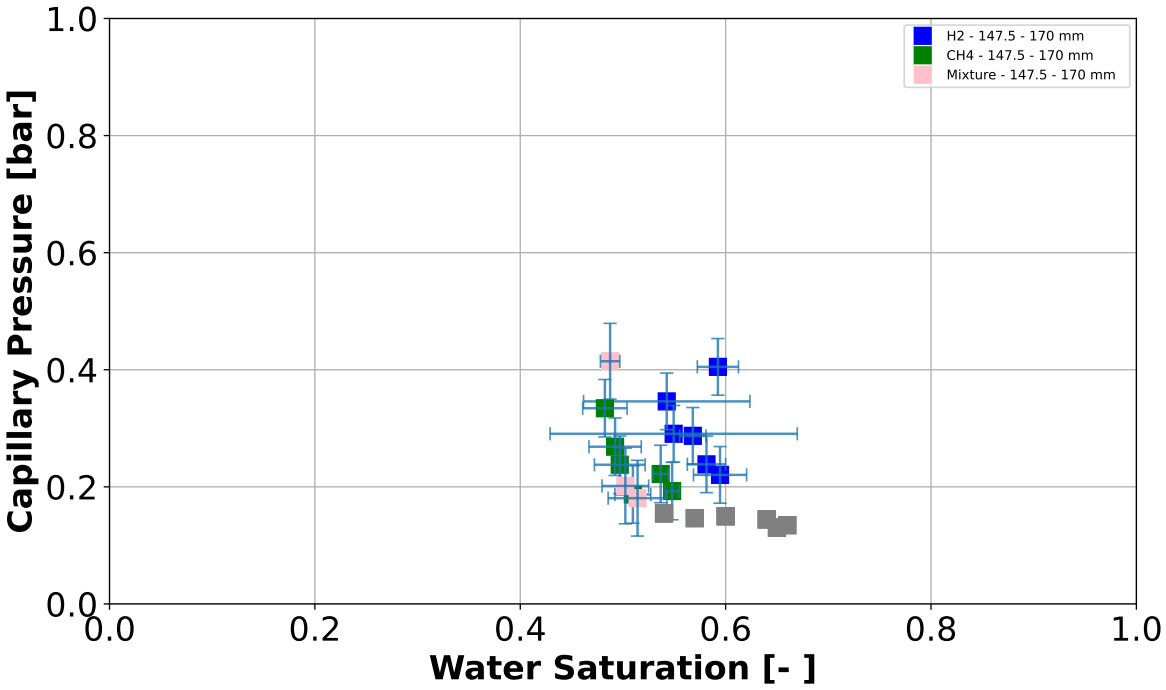

Figure 4.7: Drainage capillary pressure curve. Each color represent a specific experiment: hydrogen (blue), methane (green), and the mixture (pink). Error bars represent absolute error

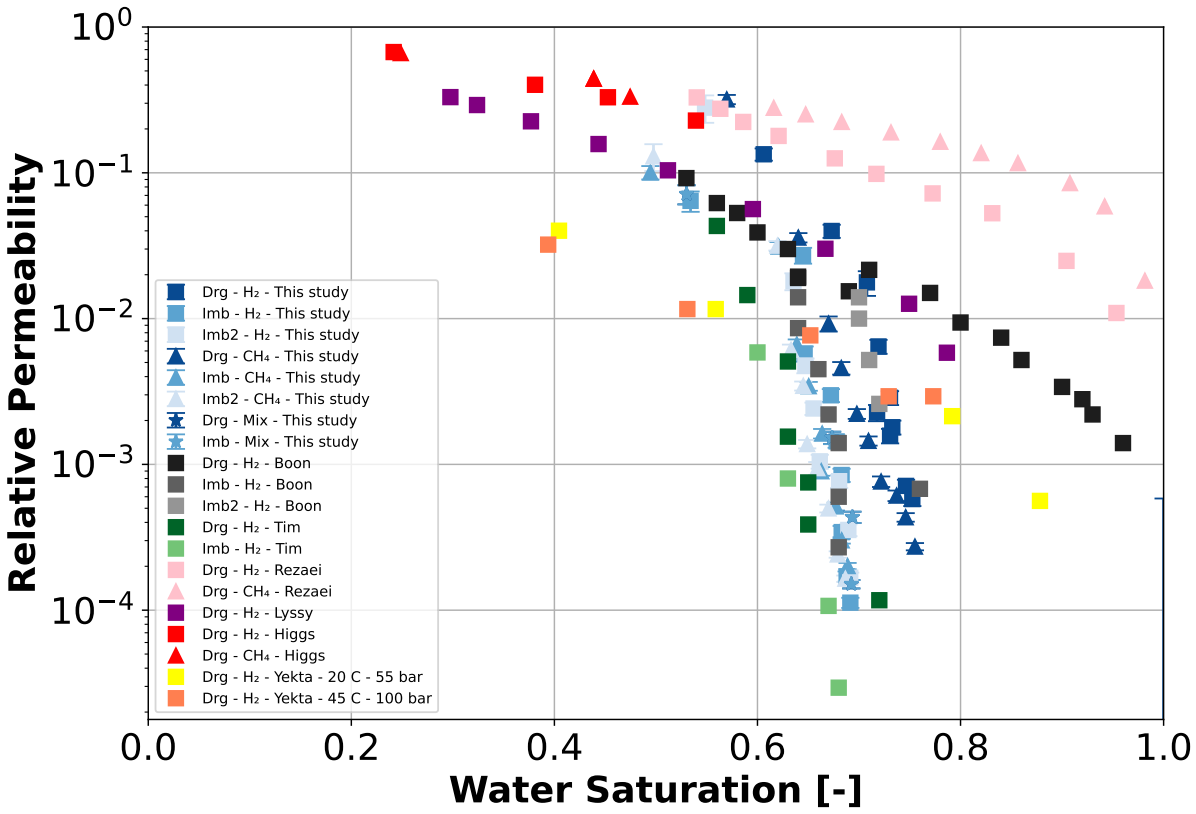

Figure 4.8: Comparison between hydrogen and methane/brine/rock systems for different drainage steady state relative permeability experiments. For an overview of experimental conditions see tables 2.1, 2.2 , and 2.3

Figure 4.5 shows the relative permeability curves for each gas composition, across drainage/imbibition cycles. Notably, all gas compositions exhibit simar relative permeability across the range of saturations achieved. The height of the crossover point for the brine and gas curves for all gas compositions are similar (between 0.01 - 0.1). The low value of the cross over points indicates a high degree of interference between the phases, resulting in lower relative permeabilities. These results are consistent with observations from previous experiments [24, 45, 84, 94] for the H_2/brine system and the CH_4/brine system [46, 84]. The cross over points for all gas mixtures in this study occurred at higher water saturations (0.6 - 0.7) than for Higgs et al. [84] (0.2 - 0.3), suggesting that the system is very water wet. Contact angle measurements were not preformed in this study, however given the similarity of the core sample used in this study to Boon et al. [24], it can be concluded that the contact angle and wettability of this system with respect to H_2 will be similar. Boon et al. [24] found a receding contact angle of 45 °. Hashemi et al. [40] found that CH_4/H_2 mixtures will have similar contact angles in porous sandstone across a range of pressures, temperature, and salinity, indicating that similarly strong wetting conditions can be assumed for the CH_4/brine (and by extension the mixture/brine) systems. This would explain the similar cross over points observed for the CH_4 and the mixture, at similar saturations to those of the H_2/brine system. The higher saturation cross over points could also be a result of the lower capillary number in this experiment during drainage (10^{-9} - 10^{-8}) compared to the higher one used by Higgs et al. [84] ($2.92 \cdot 10^{-7}$ - 10^{-5}). As Higgs et al. [84] suggest, this higher capillary number acts to shift the relative permeability curve to lower saturation due to flow dynamics approaching the viscous limit which would reduce the influence of rock heterogeneity and fluid properties such as IFT on the relative permeability. Increasing capillary number would also result in a higher contact angle between the H_2/brine phases, leading to a less water wet system that would promote the shift of kr values to lower S_w [105], a result also observed by Higgs et al. [84]. This implies that the lower capillary number used in this experiment means the kr curves naturally coincide with higher S_w.

Noticeably, while hysteresis is a property of the multiphase system, kr hysteresis during drainage/imbibition in the brine phase is negligible. This result is consistent with literature [13, 24, 45, 94]. Similarly, gas phase kr hysteresis between imbibition stages is minimal across all gas types. This is attributable to snap - off related capillary trapping, which is the governing mechanism of trapping in natural sands [106]. After the first drainage/imbibition cycle, fewer pores will be available in subsequent cycles for snap - off trapping to occur. This limits the total working volume of gas in the next drainage/imbibition cycle, while simultaneously reducing the trapping ability of the core in subsequent cycles. Other trapping mechanisms related to solubility, mineralization, and adsorption are likely negligible here for the following reasons: 1) The Berea sandstone in this study was clean and lacks the mineral components to significantly mineralize or adsorb H_2 [107]. 2) the solubility of H_2 and CH_4 in water is very small, and even less so in brine (see table 2.4), suggesting dissolution trapping mechanisms, along with the others, are likely to have had minimal influence on gas flow. H_2 experienced the most hysteresis, with H_2 kr reducing from 0.0023 during drainage, to 0.0014, and 0.001 in imbibition 1 and 2, respectively at a fractional flow fg = 0.8. At the same fractional flow, CH_4 gas kr reduced from 0.0022, to 0.0016, and 0.0015 in drainage, imbibition 1 and 2 respectively, while for the mixture, the kr decreased from 0.0022 to 0.0015 for drainage and imbibition, respectively.

The resolution of the CT scans ($190\mu m$) would not be sufficient to detect any ganglia that formed in the core, which the depressurization to atmospheric pressure alone could not remove. In other words, (considering the already established potential for gas to remain in the core across gas type experiments) the lower CH_4 kr hysteresis may be due to the presence of H_2 in the core at the start of the CH_4 drainage stage. Ganglia would obstruct flow, lowering kr, and hindering the ability of brine to trap CH_4, as much of the pore space would be occupied [13]. The drainage and imbibition mixture kr is higher than CH_4, potentially due to the more mobile H_2 it contains. It also experiences relatively less hysteresis than H_2, likely due to residue gas (which was not sufficiently removed before the start of the mixture experiment) obstructing trapping by occupying smaller pores.

To continue, linear trapping coefficients (A) suggest greater H_2 trapping in the initial drainage/imbibition cycle compared to either CH_4 or the mixture (see table 4.1). The first imbibition for H_2 and CH_4 was only allowed to run until fg = 0.2, as opposed to fg = 0 in the mixture experiment. This was due to safety, in which the build up of pressure in the system at these flow rates was approaching the safety pressure (130 bar). In attempts to observe the flow behavior at these lower flow rates, the experiments were allowed to run to $f_g = 0$ in the imbibition - 2 stage, though this did result in safety pressure being

Gas type/Experiment stage	1st cycle	2nd cycle
H2	0.66	0.46
CH4	0.62	0.35
Mixture	0.62	–

Table 4.1: Trapping capacity as defined by the linear trapping coefficient oo for different gas types at different drainage/imbibition cycles

exceeded during the H_2 experiment, preventing reasonable kr measurements (see table 3.2 at imbibition - 2 for $f_g = 0.2$). Evidently, if imbibition is allowed to extend to $f_g = 0$, trapping is substantially reduced, as shown by the much lower second cycle trapping. The trapping coefficients suggest that mixtures of H2/CH4 will exhibit less trapping than the pure H_2 system, which may be favorable for productivity in UHS reservoirs. However, producing this gas would come at the expense of the produced H_2 purity [39].

Comparing the drainage and imbibition stage for each gas as seen in Figure 4.6, the difference between H_2, CH_4, and mixture kr is more noticeable. During the drainage phase, H_2 kr is consistently higher than CH_4 kr and only slightly higher than the mixture kr, across a range of saturations. This could be due to the higher mobility of H_2, permitting it to flow with more ease through porous media - a direct result of its significantly lower viscosity [39]. It could also be related to the higher IFT of H_2 in the system, which would prevent it from invading smaller, more numerous pores, compared to CH_4, increasing the relative flow rate through the reduced pathways available, as a consequence, increasing kr [46]. Moreover, variation in the local saturation throughout the core would influence local pressure gradients, and ultimately relative permeabilities [84], which may further explain the difference. However this would require investigation on smaller scales than used in this experiment.

The drainage H_2 and CH_4 kr appear to converge as S_w decreases, which is a result consistent with previous studies [44, 46]. If interfacial forces are higher than viscous forces at higher water saturations, as suggested by Rezaei et al. [46] (i.e capillary dominated flow), this would explain, in part, the larger discrepancy in kr between the two systems during the first steps of drainage (higher S_w). The range of drainage capillary number for every gas suggests that flow is capillary dominated (see table 3.1) [108]. H_2 has a higher IFT than CH_4, which causes it to invade fewer, larger pores initially, where Pc is lower, and there is significantly decreased resistance to flow [46, 106]. With fewer paths available, H_2 flow becomes more concentrated in more larger pores, increasing kr [109]. However, at higher flow rates, capillary number increases, and viscous forces dominate, allowing fluids to utilize more of the available pore space as displacement processes are not limited to percolation through pores of least resistance, reducing the influence of heterogeneity and fluid properties such as IFT on the relative permeability [84, 109]. Gas phases will then flow similarly through the core, and reach an intrinsic permeability [84]. This intrinsic permeability is not observed in this study as flow rates were not adjusted to observe this, though the effect is seen by the converging H_2 and CH_4 kr curves.

Intriguingly, compared to drainage the situation is reversed in imbibition, with both CH_4 and the mixture obtaining a higher kr (0.0014, 0.0016 , 0.0015 for H_2, CH_4 and the mixture, respectively, at fg = 0.8 during imbibition - 1, and 0.001, 0.0016 at $f_g = 0.8$ during imbibition - 2 for the H_2 and CH_4, respectively). This indicates that the H_2 system will perform slightly worse under imbibition than CH_4, which is reasonable considering the lower capillary pressure required to mobilize CH_4 from smaller pores. This suggests that mixtures may be more favorably produced from the reservoir compared to pure H_2, though the difference is minimal.

Figure 4.8, shows the relative permeabilities for the H_2/brine/sandstone system across studies. Most strikingly, H_2 kr in this experiment is substantially lower than that found in other experiments [46, 84, 94], with the highest recorded H_2 kr in this study being an order of magnitude lower than in studies by Rezaei et al. [46], and Higgs et al. [84]. Furthermore, while this study observes higher H_2 kr than CH_4 during drainage, Rezaei et al. [46], and Higgs et al. [44] observed higher CH_4 kr across a range of saturations during drainage. The difference could be attributed to a number of reasons. The most likely is the difference in methodology and experimental conditions between the studies. Different cores, with different properties, varying pressures, orientations , and temperatures can all effect the outcome. Oddly, Higgs et al. [84] and Rezaei et al. [46] conducted their core experiment at 20 bar/18

C, and 200 bar/80 ° pressure/temperature, respectively, yet reveal similar kr - saturation H_2 curves, indicating that rock properties, rather than experimental conditions, are the primary reason for the observed differences between the studies. This is consistent with Rezaei et al. [46] and Yekta et al. [45], who suggest that rock properties exert a greater influence on gas kr in porous media than other pertinent factors.

Higgs et al. [84] use Bentheimer sandstone, which has been shown to achieve higher gas relative permeabilities than Berea at $S_w > 0.50$, while at lower water saturations their kr curves become similar [110]. This may explain why the kr curve of Higgs is higher at lower S_w, though the difference between Higgs' kr curve and the one in this study becomes appreciably smaller as S_w increases ($S_w > 0.5$). Furthermore, it has been observed that Berea sandstone achieves a higher residual brine saturation, and a lower range of mobile saturation compared to Bentheiemer [110]. This suggests the comparatively lower saturation range achieved by the Berea core in this study (0.8 - 0.5), which is similar to that obtained by Rademaker et al. [13], is likely a result of the differing rock type rather than differences in the experimental method. The Bentheiemer sandstone used by Higgs had a permeability of 655 mD, over 8 times the permeability of the Berea sandstone in this study (75 mD). As the permeability of a rock is strongly connected with the porosity, which itself is connected with relative permeability [46, 110, 111], this may explain the substantially higher kr observed for H_2 in Higgs experiment. However, permeability and porosity alone may not explain the differences between the kr curve of this study and that obtained by Rezaei et al. [46]. The sandstone used by Rezaei only had a porosity of 10.52 % , while the permeability was merely 11.18 mD. The difference here could be attributed to rock structure and tortuosity, or mineralogy of the samples. While clay content in Berea sandstone is known to be small (7 %), they are the predominant minerals at pore surfaces represented, mainly, by kaolinite and illite [111]. Clays can inhibit H_2 flow, through swelling, wettability alterations, and adsorption trapping, which is more pronounced in clays than in quartz [112]. Rezaei et al. reported only 0.2% illite concentration and 0% kaolinite in their sample, which is much less than typical Berea sandstone [111], indicating that the effects of clay on H_2 flow was likely negligible in their rock sample. The difference could reside in the pore size distribution of the samples used by Rezaei et al. [46] (0.1 - 3 μ m)). With more numerous larger pores, H_2 kr might be intrinsically higher in their core compared to the one in this study despite the lower permeability and porosity of their core.

To continue, this study observed that the H_2 kr decrease from 0.0177 to 0.0058 at $f_g = 0.99$ during drainage and imbibition is similar to that observed by Boon et al. [24] who observed a decrease in H_2 kr from 0.015 to 0.0086 at the same gas fractional flows. Moreover while the drainage curves are strikingly dissimilar, the kr imbibition curves of both studies are comparable, potentially due to trapped gas in their core inhibiting gas flow - similar to this study. Noticeable differences in Pc from both experiments are clear from Figure 4.7. Pc for the H_2 phase in this experiment were higher, with the highest Pc measurement by Boon et al. [24] (0.15 bar) being 32% smaller than the smallest recorded H_2 Pc in this study (0.22 bar). Due to the similarities in experimental conditions between these experiments, this difference may be attributed to differences in rock properties. The permeability and porosity between the rock core used in the study by Boon et al. [24] (20 % and 200 mD) and this study (15.3% and 75 mD) highlights the significant discrepancy in the rock cores, despite being of the same type. Pore size is a potential explanation for the differences. Smaller pores are more resistive to flow, while they will also contain the bulk of the wetting phase [109]. Hence, an increase in H_2 flow will primarily be through larger pores, though would only displace a minimal amount of the total brine in those sections of the core, while leading to a substantially higher kr. However, if pore sizes are generally larger in a sample, then the bulk of the brine phase will reside in pores that will be relatively more easily invaded by H_2. Hence, an increase in H_2 flow would also lead to a more substantial decrease in S_w, while the kr itself may not increase as substantially as if flow were through even larger pores. While the pore size distribution of the core in Boon et al. and in this study is unknown, the lower entry Pc measured by Boon et al. may be indicative of there being larger pore diameters, supporting the reasoning above.

The dominant influence of rock properties on fluid flow is further supported by the similarity in kr curves of this study to those of Rademaker et al. [13]. Despite being conducted at lower pressure (50 Bar), slightly higher temperature (25 °), lower flow rates (0.5 ml/min), and in a vertical orientation, Rademaker et al. [13] used a Berea sandstone core with similar porosity and permeability (18.3 and 104 mD), and obtained comparable results. Rademaker et al. [13] observed similarly steep sloping kr curves across a narrow saturation range. However, this result was attributed to the exsolution of gas due to

pressure differences across the core, similar to the discussion in section 4.1. Appendix D shows the pressure drops at different fractional H_2 flows across the core between this study, Boon et al. [24], and Rademaker et al. [13]. The pressure drops in both this study and Rademaker et al. [13], are two orders of magnitude higher than those in the experiment by Boon et al. [24]. This may explain the discrepancy between saturation profiles and saturation range. Due to the smaller pressure difference across the core, the gas exsolution effect down core may have been irrelevant in the study by Boon et al. [24].

Overall, the lack of measurements or data outside of kr and Pc make it difficult to exactly attribute the causes behind the differences in results between this study and literature. Nevertheless, the results suggest that H_2/CH_4 mixtures will behave intermediately to the pure gas systems with respect to their kr and PC across a range of saturations and flow rates. This result supports conclusions that UHS operation in depleted gas fields will not be severely hindered by the presence of residual natural gas, and models may need only minor adjustments to accurately predict UHS performance [2, 27, 37, 40, 84, 113]

5

Conclusions, Recommendations, and Reflections

This study experimentally investigated the multiphase flow behavior of H_2, CH_4, and a 50–50% molar H_2–CH_4 mixture in a 1% w.t NaCl brine saturated Berea sandstone core under conditions relevant to underground H_2 storage (UHS). Using steady state horizontal core flooding experiments at 18°C and 100 bar, combined with medical X-ray CT imaging, relative permeability and capillary pressure data were determined for each gas system during drainage and imbibition cycles. The study specifically focused on characterizing the H_2/CH_4 mixture relative permeability and capillary pressure relative to the pure components, providing crucial experimental data to address the limited availability of mixture specific relative permeability information in literature, which may provide more robust modeling data for UHS operations in depleted gas reservoirs.

This study summarizes three key findings relevant to H_2/CH_4 mixtures during storage in depleted gas reservoirs

1) The H_2/CH_4 mixture displayed intermediate kr and Pc between the pure H_2 and CH_4 systems. There is minimal difference between the CH_4 and H_2 kr and Pc curves, with H_2 obtaining slightly higher kr and Pc than CH_4 across a range of saturations. H_2 obtained a higher end point kr (0.0399) than CH_4 (0.0233) at f_g = 0.99, attributable to lower H_2 viscosity and higher mobility.

2) There is strong indication that mixture kr and Pc is composition dependent. The 50-50% mixture kr falls nearly exactly between the drainage kr of both H_2 and CH_4 at the same gas fractional flows, and suggests mixture kr may be an average of the constituent gases. Moreover, the mixture capillary pressures ranged from 0.03 to 0.17 bar, lying between the values observed for H_2 (0.22–0.35 bar) and CH_4 (0.14 – 0.33 bar).

3) Mixtures of H_2 and CH_4 may be more efficiently produced in UHS applications than pure H_2, leading to significant implications to the H_2 purity. H_2 experienced greater hysteresis across drainage – imbibition cycles (A = 0.66 - 0.459 in cycle 1 and 2), compared to CH_4 (0.62 - 0.35, in cycle 1 and 2) respectively. Mixtures appear to exhibit less trapping, obtain higher imbibition kr values, and lower hysteresis compared to H_2.

Considering the challenges in establishing the various gas compositions, and the potential of trapped residue gas being present in the core from previous gas experiments, these conclusions will need to be verified by subsequent experiments. While experimental errors may limit the results to a mere provisional indicator of the expected behavior of H_2/CH_4 mixtures during UHS operation, the kr and Pc observations agree with what can be inferred from the relevant literature, providing stronger confidence for at least the overarching finding of conclusion 1.

Future research should expand experimental conditions to more comprehensively characterize H_2/CH_4 mixture flow. Exploring additional gas compositions would support the development of predictive

models for mixtures beyond the 50–50% molar ratio. Higher resolution imaging, such as micro CT, would enable direct observation of pore scale flow, residual trapping, and preferential pathways, potentially validating the inferences made from macroscopic data over rock structure effects on the observed flow behavior. Furthermore, researching microbial and geochemical interactions with H_2/CH_4 mixtures could reveal further insight into how the gas deviates from expected behavior in the presence of species pertinent to UHS operation in reservoirs, while studies at higher temperatures and varying pressures would provide more insight into how fluid properties may effect relative permeability and capillary pressure. These findings would allow more decisive trends in kr and Pc to be derived for a range of mixtures at a range of conditions, improving modeling accuracy and UHS operation.

Reflections

Limitations

Errors were prevalent during the experiment. Despite extensive equilibration, dissolution of gas into brine may have supported the development of fingers, which later resulted in channeling, preventing accurate kr and Pc measurements at some stages of the experiment. Furthermore, differences in the core bulk and inlet pressure, resulted in exsolution of gas down core. This caused unusually low brine saturations ($S_w \leq 0.8$) at low fractional flow rates $f_g = 0.2$. Experiments were performed under steady-state conditions. At system level, this implies that transient effects during fast ramping remain obscure. However, for seasonal storage applications with relatively slow cycling, the presented data remains highly relevant.

Literature Context

Intriguingly, the kr curve of this study aligns more closely with that of Rademaker et al. [13], than Boon et al. [24], despite Rademaker et al. conducting experiments on a vertically oriented core, and at different pressure (50 bar) and temperature (20 ° C) conditions. This supports results that suggest pressure and temperature are not the determining factors on gas kr [45, 46]. The lack of data collection outside of pressure, temperature and imaging measurements directly relevant to kr and Pc make comparison and understanding the causes behind the differences with literature more challenging. Despite these limitations, the trends identified are consistent with expectations from multiphase flow theory and should still provide meaningful insights for UHS.

System Level Implications

From a system integration perspective, UHS in depleted gas reservoirs enables the decoupling of renewable energy production from end use demand, supporting higher penetration of variable renewable energy sources such as wind and solar. The ability to store hydrogen cyclically at the TWh scale is critical for balancing seasonal mismatches and providing dispatchable energy to hard to electrify sectors. The results of this study contribute to improving confidence in the operational feasibility of such storage systems. To that end, while this study does not directly quantify costs or policy outcomes, it provides essential physical input parameters required for techno-economic and policy analyses. By improving understanding of underrepresented and neglected parameters on UHS performance, such research can enhance the economic viability of UHS projects by making a direct contribution to reducing technical uncertainty, which in turn reduces investment risk.

Overall, these findings have direct implications for UHS design. The results provide crucial initial data on H_2/CH_4 mixture flow that can enhance the accuracy of reservoir simulations, and support the design of efficient and scalable H_2 storage operations in depleted gas reservoirs. Moreover, this work contributes to bridging the gap between laboratory scale experimentation and system level energy planning, supporting the integration of UHS within future sustainable energy systems.

References

[1] United Nations Department of Economic and Social Affairs. "The Sustainable Development Goals Report". In: *United Nations* (2025). ISSN: 2518-3915.

[2] Lirong Zhong et al. "Hydrogen, Methane, Brine Flow Behavior, and Saturation in Sandstone Cores During H2 and CH4 Injection and Displacement". In: *Energies* 17.22 (Nov. 2024). ISSN: 19961073. DOI: 10.3390/en17225800.

[3] Davood Zivar, Sunil Kumar, and Jalal Foroozesh. "Underground hydrogen storage: A comprehensive review". In: *International Journal of Hydrogen Energy* 46.45 (July 2021), pp. 23436–23462. ISSN: 03603199. DOI: 10.1016/j.ijhydene.2020.08.138.

[4] European Commission. *EU energy in figures - Statistical Pocketbook 2013*. Tech. rep. 2013.

[5] Tomaso Duso, Jo Seldeslachts, and Florian Szücs. *The impact of competition policy enforcement on the functioning of EU energy markets*. 2019. DOI: 10.5547/01956574.40.5.tdus.

[6] Seunghwan Baek et al. *Choose an item. Enhancing Site Screening for Underground Hydrogen Storage: Qualitative Site Quality Assessment SHASTA: Subsurface Hydrogen Assessment, Storage, and Technology Acceleration Project Pacific Northwest National Laboratory*. Tech. rep. 2024.

[7] Angela Goodman et al. *Choose an item. Subsurface Hydrogen and Natural Gas Storage: State of Knowledge and Research Recommendations Report SHASTA: Subsurface Hydrogen Assessment, Storage, and Technology Acceleration Project*. Tech. rep. 2022.

[8] Niklas Heinemann et al. *Enabling large-scale hydrogen storage in porous media-the scientific challenges*. Feb. 2021. DOI: 10.1039/d0ee03536j.

[9] N. P. Brandon and Z. Kurban. "Clean energy and the hydrogen economy". In: *Philosophical Transactions of the Royal Society A: Mathematical, Physical and Engineering Sciences* 375.2098 (July 2017). ISSN: 1364503X. DOI: 10.1098/RSTA.2016.0400. URL: /doi/pdf/10.1098/rsta.2016.0400.

[10] Aliakbar Hassanpouryouzband et al. *Offshore Geological Storage of Hydrogen: Is This Our Best Option to Achieve Net-Zero?* 2021. DOI: 10.1021/acsenergylett.1c00845.

[11] Sebastian Bauer et al. "Impacts of the use of the geological subsurface for energy storage: An investigation concept". In: *Environmental Earth Sciences* 70.8 (Dec. 2013), pp. 3935–3943. ISSN: 18666280. DOI: 10.1007/s12665-013-2883-0.

[12] Seung Kwon Seo, Dong Yeol Yun, and Chul Jin Lee. "Design and optimization of a hydrogen supply chain using a centralized storage model". In: *Applied Energy* 262 (Mar. 2020). ISSN: 03062619. DOI: 10.1016/j.apenergy.2019.114452.

[13] Tim Rademaker. *A Techno-Economic Assessment of Underground Hydrogen Storage with Investigation of H-Brine Multiphase Flow in Porous Rock at Micro-Scale*. Tech. rep. URL: http://repository.tudelft.nl/..

[14] *Novel Hydrogen Carriers | Department of Energy*. URL: https://www.energy.gov/eere/fuelcells/novel-hydrogen-carriers.

[15] Joakim Andersson and Stefan Grönkvist. "Large-scale storage of hydrogen". In: *International Journal of Hydrogen Energy* 44.23 (May 2019), pp. 11901–11919. ISSN: 0360-3199. DOI: 10.1016/J.IJHYDENE.2019.03.063.

[16] Chloe Farand. *The precious 'white gold' fuel buried in the Earth*. English. 2025. URL: https://www.bbc.com/future/article/20250723-the-worlds-race-to-drill-for-natural-white-hydrogen.

[17] Nicola De Blassio. *The Colors of Hydrogen | The Belfer Center for Science and International Affairs*. 2024. URL: https://www.belfercenter.org/research-analysis/colors-hydrogen.

[18] Geoffrey S. Ellis and Sarah E. Gelman. "Model predictions of global geologic hydrogen resources". In: *Science Advances* 10.50 (Dec. 2024). ISSN: 23752548. DOI: 10.1126/SCIADV.ADO0955.

[19] Afeez O. Gbadamosi et al. *Underground hydrogen storage: A critical assessment of fluid-fluid and fluid-rock interactions*. Nov. 2023. DOI: 10.1016/j.est.2023.108473.

[20] Maksim Lysyy, Martin A. Fernø, and Geir Ersland. "Effect of relative permeability hysteresis on reservoir simulation of underground hydrogen storage in an offshore aquifer". In: *Journal of Energy Storage* 64 (Aug. 2023). ISSN: 2352152X. DOI: 10.1016/j.est.2023.107229.

[21] *Hydrogen – Analysis - IEA*. URL: https://www.iea.org/reports/hydrogen-2156.

[22] Christopher Schaber, Patrick Mazza, and Roel Hammerschlag. "Utility-scale storage of renewable energy". In: *Electricity Journal* 17.6 (2004). ISSN: 10406190. DOI: 10.1016/j.tej.2004.05.005.

[23] Radoslaw Tarkowski. *Underground hydrogen storage: Characteristics and prospects*. May 2019. DOI: 10.1016/j.rser.2019.01.051.

[24] Maartje Boon and Hadi Hajibeygi. "Experimental characterization of H 2 /water multiphase flow in heterogeneous sandstone rock at the core scale relevant for underground hydrogen storage (UHS)". In: *Scientific Reports* 12.1 (Dec. 2022). ISSN: 20452322. DOI: 10.1038/s41598-022-18759-8.

[25] Rawaa A. Sadkhan and Watheq J. Al-Mudhafar. "Key aspects of underground hydrogen storage in depleted hydrocarbon reservoirs and saline aquifers: A review and understanding". In: *Energy Geoscience* 5.4 (Oct. 2024), p. 100339. ISSN: 2666-7592. DOI: 10.1016/J.ENGEOS.2024.100339. URL: https://www.sciencedirect.com/science/article/pii/S2666759224000544#sec4.

[26] Nasiru Salahu Muhammed et al. "A review on underground hydrogen storage: Insight into geological sites, influencing factors and future outlook". In: *Energy Reports* 8 (Nov. 2022), pp. 461–499. ISSN: 2352-4847. DOI: 10.1016/J.EGYR.2021.12.002.

[27] Nasiru Salahu Muhammed et al. *Hydrogen storage in depleted gas reservoirs: A comprehensive review*. Apr. 2023. DOI: 10.1016/j.fuel.2022.127032.

[28] S Lamboo and M Weeda. "Hydrogen use in Dutch industry Inventory of small-and medium-sized users in the context of the RFNBO industry obligation in the REDIII TNO Public TNO Public Title TNO Public Report text TNO Public Number of pages 23 (excl. front and back cover) Number of appendices 0 Sponsor Ministry of Climate Policy and Green Growth Kleine waterstofgebruikers industrie". In: (2024). URL: www.tno.nl.

[29] Mohamed L. Malki et al. *A critical review of underground hydrogen storage: From fundamentals to applications, unveiling future frontiers in energy storage*. Aug. 2024. DOI: 10.1016/j.ijhydene.2024.07.076.

[30] Axel Liebscher, Jürgen Wackerl, and Martin Streibel. "Geologic Storage of Hydrogen – Fundamentals, Processing, and Projects". In: *Hydrogen Science and Engineering: Materials, Processes, Systems and Technology* 2 (Apr. 2016), pp. 629–658. DOI: 10.1002/9783527674268.CH26. URL: /doi/pdf/10.1002/9783527674268.ch26%20https://onlinelibrary.wiley.com/doi/abs/10.1002/9783527674268.ch26%20https://onlinelibrary.wiley.com/doi/10.1002/9783527674268.ch26.

[31] "Hychico S.A. Green Hydrogen-Argentina". In: ().

[32] *Underground Sun Storage*. URL: https://www.underground-sun-storage.at/en/.

[33] *About – HyUSPRe*. URL: https://www.hyuspre.eu/index.php/about/.

[34] Remco Groenenberg et al. "Large-Scale Energy Storage in Salt Caverns and Depleted Fields (LSES)-Project Findings". In: (2020).

[35] Zhenkai Bo et al. "Impact of experimentally measured relative permeability hysteresis on reservoir-scale performance of underground hydrogen storage (UHS)". In: *International Journal of Hydrogen Energy* 48.36 (Apr. 2023), pp. 13527–13542. ISSN: 03603199. DOI: 10.1016/j.ijhydene.2022.12.270.

[36] Robin Johannes Terstappen and H Hajibeygi. *ANALYSIS OF MIXING DURING HYDROGEN STORAGE IN GAS RESERVOIRS A RESERVOIR SIMULATION STUDY*. Tech. rep. 2021. URL: http://repository.tudelft.nl/..

[37] Nasiru Salahu Muhammed, Bashirul Haq, and Dhafer Al Shehri. "Role of methane as a cushion gas for hydrogen storage in depleted gas reservoirs". In: *International Journal of Hydrogen Energy* 48.76 (Sept. 2023), pp. 29663–29681. ISSN: 03603199. DOI: 10.1016/j.ijhydene.2023.04.173.

[38] Mahdi Kanaani, Behnam Sedaee, and Mojtaba Asadian-Pakfar. "Role of Cushion Gas on Underground Hydrogen Storage in Depleted Oil Reservoirs". In: *Journal of Energy Storage* 45 (Jan. 2022). ISSN: 2352152X. DOI: 10.1016/j.est.2021.103783.

[39] Thomas A. Buscheck et al. "Underground storage of hydrogen and hydrogen/methane mixtures in porous reservoirs: Influence of reservoir factors and engineering choices on deliverability and storage operations". In: *International Journal of Hydrogen Energy* 49 (Jan. 2024), pp. 1088–1107. ISSN: 03603199. DOI: 10.1016/j.ijhydene.2023.07.073.

[40] Leila Hashemi et al. "A comparative study for H2–CH4 mixture wettability in sandstone porous rocks relevant to underground hydrogen storage". In: *Advances in Water Resources* 163 (May 2022). ISSN: 03091708. DOI: 10.1016/j.advwatres.2022.104165.

[41] Wenjia Ou et al. "Measurement of methane solubility in pure water in equilibrium with hydrate by using high–pressure optical capillary cell". In: *Marine Chemistry* 212 (May 2019), pp. 74–82. ISSN: 0304-4203. DOI: 10.1016/J.MARCHEM.2019.04.003.

[42] Samuel C.M. Krevor et al. "Relative permeability and trapping of CO 2 and water in sandstone rocks at reservoir conditions". In: *Water Resources Research* 48.2 (2012). ISSN: 00431397. DOI: 10.1029/2011WR010859.

[43] Ahmed Al-Yaseri et al. "Initial and residual trapping of hydrogen and nitrogen in Fontainebleau sandstone using nuclear magnetic resonance core flooding". In: *International Journal of Hydrogen Energy* 47.53 (June 2022), pp. 22482–22494. ISSN: 03603199. DOI: 10.1016/j.ijhydene.2022.05.059.

[44] Scott Higgs et al. "Direct measurement of hydrogen relative permeability hysteresis for underground hydrogen storage". In: *International Journal of Hydrogen Energy* 50 (Jan. 2024), pp. 524–541. ISSN: 03603199. DOI: 10.1016/j.ijhydene.2023.07.270.

[45] A. E. Yekta et al. "Determination of Hydrogen–Water Relative Permeability and Capillary Pressure in Sandstone: Application to Underground Hydrogen Injection in Sedimentary Formations". In: *Transport in Porous Media* 122.2 (Mar. 2018), pp. 333–356. ISSN: 15731634. DOI: 10.1007/s11242-018-1004-7.

[46] Amin Rezaei et al. "Relative Permeability of Hydrogen and Aqueous Brines in Sandstones and Carbonates at Reservoir Conditions". In: *Geophysical Research Letters* 49.12 (June 2022). ISSN: 19448007. DOI: 10.1029/2022GL099433.

[47] Eric Baruch and Gutierrez Castillo. *Relative Permeability Hysteresis in Porous Media*. Tech. rep.

[48] Leila Hashemi, Martin Blunt, and Hadi Hajibeygi. "Pore-scale modelling and sensitivity analyses of hydrogen-brine multiphase flow in geological porous media". In: *Scientific Reports* 11.1 (Dec. 2021). ISSN: 20452322. DOI: 10.1038/s41598-021-87490-7.

[49] Paul Glover. *Petrophysics MSc Course Notes Fluid Saturation and Capillary Pressure 4. FLUID SATURATION AND CAPILLARY PRESSURE 4.1 Fluid Saturations*. Tech. rep.

[50] Arshad Raza et al. *A holistic overview of underground hydrogen storage: Influencing factors, current understanding, and outlook*. Dec. 2022. DOI: 10.1016/j.fuel.2022.125636.

[51] Leila Hashemi et al. "Contact angle measurement for hydrogen/brine/sandstone system using captive-bubble method relevant for underground hydrogen storage". In: *Advances in Water Resources* 154 (Aug. 2021). ISSN: 03091708. DOI: 10.1016/j.advwatres.2021.103964.

[52] Stefan Iglauer et al. "CO2 wettability of caprocks: Implications for structural storage capacity and containment security". In: *Geophysical Research Letters* 42.21 (Nov. 2015), pp. 9279–9284. ISSN: 1944-8007. DOI: 10.1002/2015GL065787. URL: /doi/pdf/10.1002/2015GL065787%20https://onlinelibrary.wiley.com/doi/abs/10.1002/2015GL065787%20https://agupubs.onlinelibrary.wiley.com/doi/10.1002/2015GL065787.

[53] Lingping Zeng et al. “Hydrogen Storage Performance During Underground Hydrogen Storage in Depleted Gas Reservoirs: A Review”. In: *Engineering* 40 (Sept. 2024), pp. 211–225. ISSN: 2095-8099. DOI: 10.1016/J.ENG.2024.03.011. URL: https://www.sciencedirect.com/science/article/pii/S2095809924002285.

[54] Stefan Iglauer. “Optimum geological storage depths for structural H2 geo-storage”. In: *This Journal Article is posted Journal of Petroleum Science and Engineering* 212 (2022), p. 109498. DOI: 10.1016/j.petrol.2021.109498. URL: https://doi.org/10.1016/j.petrol.2021.109498.

[55] Mathias. “ANNEX A2 CO 2 Storage Liabilities in the North Sea-An Assessment of Risks and Financial Consequences”. In: ().

[56] Roger M. Slatt. “Geologic Controls on Reservoir Quality”. In: *Developments in Petroleum Science* 61 (Jan. 2013), pp. 229–281. ISSN: 0376-7361. DOI: 10.1016/B978-0-444-56365-1.00006-7. URL: https://www.sciencedirect.com/science/article/pii/B9780444563651000067#ab0010.

[57] Samuel Krevor et al. “Capillary trapping for geologic carbon dioxide storage – From pore scale physics to field scale implications”. In: *International Journal of Greenhouse Gas Control* 40 (Sept. 2015), pp. 221–237. ISSN: 1750-5836. DOI: 10.1016/J.IJGGC.2015.04.006. URL: https://www.sciencedirect.com/science/article/pii/S1750583615001486.

[58] P O Carden and L Paterson. *PHYSICAL, CHEMICAL AND ENERGY ASPECTS OF UNDERGROUND HYDROGEN STORAGE*. Tech. rep., pp. 559–569.

[59] Chiradip Bagchi et al. “A Critical Review on Parameters Affecting the Feasibility of Underground Hydrogen Storage”. In: *ACS Omega* 10.12 (Apr. 2025), pp. 11658–11696. ISSN: 24701343. DOI: 10.1021/ACSOMEGA.4C10442/ASSET/IMAGES/LARGE/AO4C10442{_}0046.JPEG. URL: /doi/pdf/10.1021/acsomega.4c10442?ref=article_openPDF.

[60] Feng Guo and Saman A. Aryana. “An Experimental Investigation of Flow Regimes in Imbibition and Drainage Using a Microfluidic Platform”. In: *Energies 2019, Vol. 12, Page 1390* 12.7 (Apr. 2019), p. 1390. ISSN: 1996-1073. DOI: 10.3390/EN12071390. URL: https://www.mdpi.com/1996-1073/12/7/1390/htm%20https://www.mdpi.com/1996-1073/12/7/1390.

[61] Gang Wang et al. “Inherent Errors in Current Core-Flooding Relative Permeability Data for Modelling Underground Hydrogen Storage”. In: *InterPore Journal* 2.1 (Feb. 2025), pp. 260225–6. ISSN: 3007-410X. DOI: 10.69631/ipj.v2i1nr42. URL: https://ipjournal.interpore.org/index.php/interpore/article/view/42.

[62] G M Homsy. “Viscous Fingering in Porous Media”. In: *Annual Review of Fluid Mechanics* 19.Volume 19, 1987 (Jan. 1987), pp. 271–311. ISSN: 0066-4189. DOI: 10.1146/ANNUREV.FL.19.010187.001415. URL: https://www.annualreviews.org/doi/10.1146/annurev.fl.19.010187.001415.

[63] M. Hanarpour and S. M. Mahmood. “Relative-Permeability Measurements: An Overview”. In: *Journal of Petroleum Technology* 40.08 (Aug. 1988), pp. 963–966. ISSN: 0149-2136. DOI: 10.2118/18565-PA. URL: https://dx.doi.org/10.2118/18565-PA.

[64] Bashir Alkhazmi et al. *SCA2024-1028 An Experimental Investigation of Oil Recovery Mechanisms and Relative Permeability Curves Obtained by Steady-State versus Unsteady-State Displacement*. Tech. rep.

[65] Bijay K C et al. “Laboratory study of cyclic underground hydrogen storage in porous media with evidence of a dry near-well zone and evaporation induced salt precipitation”. In: *International Journal of Hydrogen Energy* 71 (June 2024), pp. 515–527. ISSN: 0360-3199. DOI: 10.1016/J.IJHYDENE.2024.05.234. URL: https://www.sciencedirect.com/science/article/pii/S0360319924019311#bib11.

[66] Ronny Pini, Samuel C.M. Krevor, and Sally M. Benson. “Capillary pressure and heterogeneity for the CO2/water system in sandstone rocks at reservoir conditions”. In: *Advances in Water Resources* 38 (Mar. 2012), pp. 48–59. ISSN: 0309-1708. DOI: 10.1016/J.ADVWATRES.2011.12.007. URL: https://www.sciencedirect.com/science/article/pii/S0309170811002363?via%3Dihub#aep-abstract-id22.

[67] Miguel A Aleman ’
, Tumkur R Ramamohan, and John C Slattery. *The Difference Between Steady-State and Unsteady-State Relative Permeabilities*. Tech. rep. 1989, p. 449.

[68] Bin Pan et al. *Underground hydrogen storage: Influencing parameters and future outlook*. Aug. 2021. DOI: 10.1016/j.cis.2021.102473.

[69] Vahideh Mirchi, Morteza Dejam, and Vladimir Alvarado. "Interfacial tension and contact angle measurements for hydrogen-methane mixtures/brine/oil-wet rocks at reservoir conditions". In: *International Journal of Hydrogen Energy* 47.82 (Sept. 2022), pp. 34963–34975. ISSN: 0360-3199. DOI: 10.1016/J.IJHYDENE.2022.08.056. URL: https://www.sciencedirect.com/science/article/pii/S0360319922035133.

[70] Abdolhossein Hemmati-Sarapardeh et al. "Experimental Determination of Interfacial Tension and Miscibility of the CO2–Crude Oil System; Temperature, Pressure, and Composition Effects". In: *Journal of Chemical and Engineering Data* 59.1 (Jan. 2013), pp. 61–69. ISSN: 00219568. DOI: 10.1021/JE400811H. URL: https://pubs.acs.org/doi/abs/10.1021/je400811h.

[71] Ali Zolghadr, Mehdi Escrochi, and Shahab Ayatollahi. "Temperature and Composition Effect on CO2 Miscibility by Interfacial Tension Measurement". In: *Journal of Chemical and Engineering Data* 58.5 (May 2013), pp. 1168–1175. ISSN: 00219568. DOI: 10.1021/JE301283E. URL: https://pubs.acs.org/doi/abs/10.1021/je301283e.

[72] Amer Alanazi et al. "Influence of organics and gas mixing on hydrogen/brine and methane/brine wettability using Jordanian oil shale rocks: Implications for hydrogen geological storage". In: *Journal of Energy Storage* 62 (June 2023). ISSN: 2352152X. DOI: 10.1016/j.est.2023.106865.

[73] Mirhasan Hosseini et al. "H2brine interfacial tension as a function of salinity, temperature, and pressure; implications for hydrogen geo-storage". In: *Journal of Petroleum Science and Engineering* 213 (June 2022), p. 110441. ISSN: 0920-4105. DOI: 10.1016/J.PETROL.2022.110441. URL: https://www.sciencedirect.com/science/article/abs/pii/S0920410522003278?via%3Dihub.

[74] Scott Higgs et al. "In-situ hydrogen wettability characterisation for underground hydrogen storage". In: *International Journal of Hydrogen Energy* 47.26 (Mar. 2022), pp. 13062–13075. ISSN: 0360-3199. DOI: 10.1016/J.IJHYDENE.2022.02.022. URL: https://www.sciencedirect.com/science/article/pii/S0360319922005456?casa_token=R4XDoerLfB8AAAAA:-zR-0J9w_fl0b8tf21129oYYVuizAcvUe-dMK3gZOKD1qVdkg_30AtXXu7X6EaPQxzRIEC37h2yr.

[75] Salaheddine Chabab et al. "Solubility of H2 in water and NaCl brine under subsurface storage conditions: Measurements and thermodynamic modeling". In: *International Journal of Hydrogen Energy* 50 (Jan. 2024), pp. 648–658. ISSN: 03603199. DOI: 10.1016/j.ijhydene.2023.10.290.

[76] Raoof Gholami. "Hydrogen storage in geological porous media: Solubility, mineral trapping, H2S generation and salt precipitation". In: *Journal of Energy Storage* 59 (Mar. 2023), p. 106576. ISSN: 2352-152X. DOI: 10.1016/J.EST.2022.106576. URL: https://www.sciencedirect.com/science/article/pii/S2352152X22025658?via=ihub#f0010.

[77] Arne Böttger, Álvaro Pérez-Salado Kamps, and Gerd Maurer. "An experimental investigation of the phase equilibrium of the binary system (methane + water) at low temperatures: Solubility of methane in water and three-phase (vapour + liquid + hydrate) equilibrium". In: *Fluid Phase Equilibria* 407 (Jan. 2016), pp. 209–216. ISSN: 0378-3812. DOI: 10.1016/J.FLUID.2015.03.041. URL: https://www.sciencedirect.com/science/article/pii/S037838121500179X.

[78] Zhenhao Duan et al. *The prediction of methane solubility in natural waters to high ionic strength from 0 to 250°C and from 0 to 1600 bar*. Tech. rep. 1992, pp. 1451–1460.

[79] Michel Tawil et al. "Solubility of H2-CH4 mixtures in brine at underground hydrogen storage thermodynamic conditions". In: *Frontiers in Energy Research* 12 (Apr. 2024), p. 1356491. ISSN: 2296598X. DOI: 10.3389/FENRG.2024.1356491/BIBTEX.

[80] *Tables of Physical and Chemical Constants : G.W.C Kaye,T.H Laby : Free Download, Borrow, and Streaming : Internet Archive*. URL: https://archive.org/details/tablesofphysical004093mbp.

[81] Ying Gao et al. "Advanced Digital-SCAL Measurements of Gas Trapped in Sandstone1". In: *Petrophysics* 64.3 (June 2023), pp. 368–383. ISSN: 15299074. DOI: 10.30632/PJV64N3-2023A4. URL: https://www.researchgate.net/publication/371242304_Advanced_Digital-SCAL_Measurements_of_Gas_Trapped_in_Sandstone.

[82] Xiao Zhao and Hui Jin. "Investigation of hydrogen diffusion in supercritical water: A molecular dynamics simulation study". In: *International Journal of Heat and Mass Transfer* 133 (Apr. 2019), pp. 718–728. ISSN: 0017-9310. DOI: 10.1016/J.IJHEATMASSTRANSFER.2018.12.164. URL: https://www.sciencedirect.com/science/article/abs/pii/S0017931018347422.

[83] *Gases dissolved in Water - Diffusion Coefficients*. URL: https://www.engineeringtoolbox.com/diffusion-coefficients-d_1404.html.

[84] Scott Higgs et al. "Comparative analysis of hydrogen, methane and nitrogen relative permeability: Implications for Underground Hydrogen Storage". In: *Journal of Energy Storage* 73 (Dec. 2023). ISSN: 2352152X. DOI: 10.1016/j.est.2023.108827.

[85] Vladislav Arekhov et al. "Measurement of Effective Hydrogen-Methane Gas Diffusion Coefficients in Reservoir Rocks". In: *SPE Reservoir Evaluation & Engineering* 26.04 (Nov. 2023), pp. 1242–1257. ISSN: 1094-6470. DOI: 10.2118/214451-PA. URL: https://dx.doi.org/10.2118/214451-PA.

[86] Jinjian Hou et al. "Salinity, temperature and pressure effect on hydrogen wettability of carbonate rocks". In: *International Journal of Hydrogen Energy* 48.30 (Apr. 2023), pp. 11303–11311. ISSN: 0360-3199. DOI: 10.1016/J.IJHYDENE.2022.05.274. URL: https://www.sciencedirect.com/science/article/pii/S0360319922024764?via%3Dihub.

[87] Muhammad Ali et al. "Influence of pressure, temperature and organic surface concentration on hydrogen wettability of caprock; implications for hydrogen geo-storage". In: *Energy Reports* 7 (Nov. 2021), pp. 5988–5996. ISSN: 2352-4847. DOI: 10.1016/J.EGYR.2021.09.016. URL: https://www.sciencedirect.com/science/article/pii/S2352484721008210?via%3Dihub.

[88] Bin Pan, Xia Yin, and Stefan Iglauer. "Rock-fluid interfacial tension at subsurface conditions: Implications for H2, CO2 and natural gas geo-storage". In: *International Journal of Hydrogen Energy* 46.50 (July 2021), pp. 25578–25585. ISSN: 0360-3199. DOI: 10.1016/J.IJHYDENE.2021.05.067. URL: https://www.sciencedirect.com/science/article/pii/S0360319921018218?via%3Dihub.

[89] Hamid Esfandyari et al. "Assessment of the interfacial properties of various mineral/hydrogen/water systems". In: *Journal of Energy Storage* 60 (Apr. 2023). ISSN: 2352152X. DOI: 10.1016/j.est.2023.106637.

[90] C. A. Reynolds and S. Krevor. "Characterizing flow behavior for gas injection: Relative permeability of CO2-brine and N2-water in heterogeneous rocks". In: *Water Resources Research* 51.12 (Dec. 2015), pp. 9464–9489. ISSN: 19447973. DOI: 10.1002/2015WR018046;PAGE:STRING:ARTICLE/CHAPTER. URL: /doi/pdf/10.1002/2015WR018046%20https://onlinelibrary.wiley.com/doi/abs/10.1002/2015WR018046%20https://agupubs.onlinelibrary.wiley.com/doi/10.1002/2015WR018046.

[91] Stefan Bachu and Brant Bennion. "Effects of in-situ conditions on relative permeability characteristics of CO2-brine systems". In: *SpringerS Bachu, B BennionEnvironmental Geology, 2008•Springer* 54.8 (June 2008), pp. 1707–1722. ISSN: 09430105. DOI: 10.1007/S00254-007-0946-9. URL: https://idp.springer.com/authorize/casa?redirect_uri=https://link.springer.com/article/10.1007/s00254-007-0946-9&casa_token=v83VQVVu2D8AAAAA:oH9AT3v-FXIaVuqHwf5CsuH1jDX4_BWgbpc4KJMVq9TRBsCdbypiuNVCc7sQu1kxDZBVgYx0mTsFbWadR54.

[92] Sojwal Manoorkar et al. "From underground natural gas to hydrogen storage in fractured reservoir rock : comparing relative permeabilities for hydrogen versus methane and nitrogen". In: (Nov. 2024). URL: https://arxiv.org/pdf/2411.14122v1.

[93] Nilesh Kumar Jha et al. "Pore scale investigation of hydrogen injection in sandstone via X-ray micro-tomography". In: *International Journal of Hydrogen Energy* 46.70 (Oct. 2021), pp. 34822–34829. ISSN: 03603199. DOI: 10.1016/J.IJHYDENE.2021.08.042.

[94] Maksim Lysyy et al. "Hydrogen Relative Permeability Hysteresis in Underground Storage". In: *Geophysical Research Letters* 49.17 (Sept. 2022), e2022GL100364. ISSN: 19448007. DOI: 10.1029/2022GL100364;WGROUP:STRING:PUBLICATION. URL: /doi/pdf/10.1029/2022GL100364%20https://onlinelibrary.wiley.com/doi/abs/10.1029/2022GL100364%20https://agupubs.onlinelibrary.wiley.com/doi/10.1029/2022GL100364.

[95] Eike M. Thaysen et al. "Pore-scale imaging of hydrogen displacement and trapping in porous media". In: *International Journal of Hydrogen Energy* 48.8 (Jan. 2023), pp. 3091–3106. ISSN: 0360-3199. DOI: 10.1016/J.IJHYDENE.2022.10.153. URL: https://www.sciencedirect.com/science/article/pii/S0360319922048480.

[96] Zaid Jangda et al. "Pore-scale visualization of hydrogen storage in a sandstone at subsurface pressure and temperature conditions: Trapping, dissolution and wettability". In: *Journal of Colloid and Interface Science* 629 (Jan. 2023), pp. 316–325. ISSN: 0021-9797. DOI: 10.1016/J.JCIS.2022.09.082. URL: https://www.sciencedirect.com/science/article/pii/S0021979722016678.

[97] Sepideh Goodarzi et al. "Trapping, hysteresis and Ostwald ripening in hydrogen storage: A pore-scale imaging study". In: *International Journal of Hydrogen Energy* 56 (Feb. 2024), pp. 1139–1151. ISSN: 0360-3199. DOI: 10.1016/J.IJHYDENE.2023.12.029. URL: https://www.sciencedirect.com/science/article/pii/S0360319923062675.

[98] *NIST Chemistry WebBook*. URL: https://webbook.nist.gov/chemistry/.

[99] Aliakbar Hassanpouryouzband et al. "Thermodynamic and transport properties of hydrogen containing streams". In: *Scientific Data* 7.1 (Dec. 2020), pp. 1–14. ISSN: 20524463. DOI: 10.1038/S41597-020-0568-6;SUBJMETA=4077,4079,4086,4088,4109,639,909;KWRD=HYDROGEN+ENERGY,UNDERGROUND+HYDROGEN+STORAGE. URL: https://www.nature.com/articles/s41597-020-0568-6.

[100] Salaheddine Chabab et al. "Measurements and predictive models of high-pressure H2 solubility in brine (H2O+NaCl) for underground hydrogen storage application". In: *International Journal of Hydrogen Energy* 45.56 (Nov. 2020), pp. 32206–32220. ISSN: 03603199. DOI: 10.1016/j.ijhydene.2020.08.192.

[101] Junfang Zhang et al. "Molecular dynamics and experimental study on the solubility and diffusivity of mixed hydrogen and methane in water". In: *International Journal of Hydrogen Energy* 109 (Mar. 2025), pp. 1372–1383. ISSN: 03603199. DOI: 10.1016/j.ijhydene.2025.02.170.

[102] *VP Metering Pumps: High-Accuracy, High-Pressure, Laboratory Metering Pumps - Vindum Engineering*. URL: https://vindum.com/products/vindum-metering-pumps.

[103] Chia Wei Kuo and Sally M. Benson. "Analytical Study of Effects of Flow Rate, Capillarity, and Gravity on CO2/Brine Multiphase-Flow System in Horizontal Corefloods". In: *SPE Journal* 18.04 (July 2013), pp. 708–720. ISSN: 1086-055X. DOI: 10.2118/153954-PA. URL: https://dx.doi.org/10.2118/153954-PA.

[104] D. Loggia et al. "Phase diagram of stable miscible displacements in layered porous media". In: *Europhysics Letters* 36.2 (Oct. 1996), p. 105. ISSN: 0295-5075. DOI: 10.1209/EPL/I1996-00194-Y. URL: https://iopscience.iop.org/article/10.1209/epl/i1996-00194-y%20https://iopscience.iop.org/article/10.1209/epl/i1996-00194-y/meta.

[105] Maksim Lysyy, Geir Ersland, and Martin Fernø. "Pore-scale dynamics for underground porous media hydrogen storage". In: *Advances in Water Resources* 163 (May 2022), p. 104167. ISSN: 0309-1708. DOI: 10.1016/J.ADVWATRES.2022.104167. URL: https://www.sciencedirect.com/science/article/pii/S0309170822000434?via%3Dihub#sec0025.

[106] Ilan Ben-Noah, Shmulik P. Friedman, and Brian Berkowitz. "Dynamics of Air Flow in Partially Water-Saturated Porous Media". In: *Reviews of Geophysics* 61.2 (June 2023), e2022RG000798. ISSN: 1944-9208. DOI: 10.1029/2022RG000798. URL: /doi/pdf/10.1029/2022RG000798%20https://onlinelibrary.wiley.com/doi/abs/10.1029/2022RG000798%20https://agupubs.onlinelibrary.wiley.com/doi/10.1029/2022RG000798.

[107] Qian Zhang et al. "Hydrogen and Cushion Gas Adsorption–Desorption Dynamics on Clay Minerals". In: *ACS Applied Materials & Interfaces* 16.40 (Oct. 2024), pp. 53994–54006. ISSN: 19448252. DOI: 10.1021/ACSAMI.4C12931. URL: /doi/pdf/10.1021/acsami.4c12931?ref=article_openPDF.

[108] R Lenormand, A Eisenzimmer, and Ph Delaplace. "1995: Improvements of the Semidynamic Method for Capillary Pressure Measurements". In: *SCA Confere,nce Paper Number* 953 (1995), p. 1.

[109] A. L. Herring et al. "Observations of nonwetting phase snap-off during drainage". In: *Advances in Water Resources* 121 (Nov. 2018), pp. 32–43. ISSN: 0309-1708. DOI: 10.1016/J.ADVWATRES.2018.07.016. URL: https://www.sciencedirect.com/science/article/pii/S0309170818302793#sec0013.

[110] D R Maloney, M M Honarpour, and A D Brlnkmeyer. *NIPER-441 (DE90000212) THE EFFECTS OF ROCK CHARACTERISTICS ON RELATIVE PERMEABILITY Topical Report so nor Micm COVER*. Tech. rep. 1990.

[111] Rikan Kareem, Pablo Cubillas, and Jon Gluyas. "Multi-technique Approach to the Petrophysical Characterization of Berea Sandstone Core Plugs 2 (Cleveland Quarries, USA)". In: ().

[112] Krzysztof Labus and Radosław Tarkowski. "Modeling hydrogen – rock – brine interactions for the Jurassic reservoir and cap rocks from Polish Lowlands". In: *International Journal of Hydrogen Energy* 47.20 (Mar. 2022), pp. 10947–10962. ISSN: 0360-3199. DOI: 10.1016/J.IJHYDENE.2022.01.134. URL: https://www.sciencedirect.com/science/article/pii/S0360319922002518.

[113] Sojwal Manoorkar et al. "From underground natural gas to hydrogen storage in fractured reservoir rock : comparing relative permeabilities for hydrogen versus methane and nitrogen". In: (Nov. 2024). URL: http://arxiv.org/abs/2411.14122.

[114] Alberto Boretti. "Phased transition from methane to hydrogen in internal combustion engines: Utilizing hythane and direct injection jet ignition for enhanced efficiency and reduced emissions". In: *International Journal of Hydrogen Energy* 80 (Aug. 2024), pp. 1255–1265. ISSN: 0360-3199. DOI: 10.1016/J.IJHYDENE.2024.07.251. URL: https://www.sciencedirect.com/science/article/abs/pii/S0360319924029252.

[115] Qianqian Xue et al. "Co-mixing hydrogen and methane may double the energy storage capacity". In: *Journal of Materials Chemistry A* 6.19 (May 2018), pp. 8916–8922. ISSN: 2050-7496. DOI: 10.1039/C8TA01909F. URL: https://pubs.rsc.org/en/content/articlehtml/2018/ta/c8ta01909f%20https://pubs.rsc.org/en/content/articlelanding/2018/ta/c8ta01909f.

[116] Vahideh Mirchi et al. "Effect of Cushion Gas on Hydrogen/Brine Flow Behavior in Oil-Wet Rocks with Application to Hydrogen Storage in Depleted Oil and Gas Reservoirs". In: *Energy & Fuels* 37.19 (Oct. 2023), pp. 15231–15243. ISSN: 15205029. DOI: 10.1021/ACS.ENERGYFUELS.3C02884. URL: https://pubs.acs.org/doi/abs/10.1021/acs.energyfuels.3c02884.

[117] Mingshan Zhang et al. "Molecular simulation on H2 adsorption in nanopores and effects of cushion gas: Implications for underground hydrogen storage in shale reservoirs". In: *Fuel* 361 (Apr. 2024), p. 130621. ISSN: 0016-2361. DOI: 10.1016/J.FUEL.2023.130621. URL: https://www.sciencedirect.com/science/article/pii/S0016236123032350#f0030.

A

Gas change procedure and error

Hydrogen to methane procedure

Flowing the hydrogen gas experiments, valve three was closed and the hydrogen cylinder was replaced with the methane cylinder. Valve 9 was connected to the fume hood with a tube. To effectively flush out the remaining hydrogen gas from the system, the brine pump was activated at a flow rate of 10 mL/min, the gas pump was switched off and closed, while valve 1 was carefully opened to allow pressure to build. After reaching a stable pressure, valve 1 was closed and the brine pump was turned off. Then valve 9 was opened to release gas to the fume hood. This process was repeated multiple times until no more hydrogen could be removed from the core in this way. The methane pump, now connected to the system, was turned on, then used to bring the pressure back to 100 bar, and the brine was re-equilibrated in the same way as with the pure hydrogen experiment.

Methane to Mixture procedure

A similar approach to the procedure above was used to establish the gas mixture after the conclusion of the methane experiment. When the methane experiment concluded, valve 3 is closed, and both pumps turned off. The methane cylinder is swapped with the hydrogen cylinder, connecting it to valve 3. To reduce the system pressure to 50 bar, valve 9 is connected to the fume hood with a tube, and opened, releasing methane from the core. Valve 9 is then closed to prevent more degassing. The brine pump is then turned on to displace methane from the core to the rest of the system. This allows for more efficient mixing with hydrogen when it is in the system. The brine pump is then turned off.

Valves 7 and 8 are then closed to bypass the core. Valve 3 is opened gradually to increase system pressure to 100 bar with hydrogen gas, and then closed again. The brine pump and the gas pump are both turned on, and both gas and brine are circulated through the system bypassing the core at a flow rate of 10 ml/min. The equilibration is let to proceed for 30 minutes, after which the gas pump is stopped, and valves 7 and 8 are opened, permitting brine to flood the core. Once the brine has saturated the core, the drainage experiment can begin following the procedures outlined in section Methodology.

Experimental Errors

Leakage and Adjustments

Gas leakage was encountered during the hydrogen drainage relative permeability experiments and capillary pressure measurements at flow rates of 7, 10, and 15 mL/min. An overnight pressure drop exceeding 11 bar was recorded. The source of the leak was eventually identified and repaired using Snoop.

When repairing the leak, the cores position inadvertently shifted within the CT scanner. As a result, the imaging had to be realigned, reducing the scan range slightly. The CT image stack was adjusted from 366 slices (used in earlier experiments) to 355 slices, with a 0.5 mm shift in position to account for the displacement.

Pressures

After the first two drainage measurements for the pure hydrogen experiment the pressure gauges were changed to ones with a higher (16 bar) pressure range. Initially instruments with a pressure range of 6 bar were used. For the first two drainage measurements at fractional as flow of $f_g = 0.2$ and $f_g = 0.3$ it was quickly seen that the pressure in the middle of the core, namely between 21.5 and 147.5 mm, exceeded the pressure gauges maximum measurement capability. Due to this, the pressure in the middle of the core for these two measurements was calculated by subtracting the measurements of the other differential pressure transducers from the pressure at the inlet. This lead to a higher kr when compared to the other readings.

It was observed that a pressure drift of 0.01 - 0.02 bar occurred in the differential pressure transducers, alongside a steady 0.1 bar pressure drop across the system between measurements. While seemingly small, it is imperative to recalibrate the pressure gauges to ensure as high a level of experimental accuracy. In this experiment, this was done before every new flow rate was set, while both pumps where switched off.

B

Gas Composition Considerations

Provided the absence of a mas spectrometer and other apparatus that may have directly measured the gas composition, this methodology establishes a 50-50% H_2/CH_4 molar ratio in the system using the general principles of the ideal gas law B.1, rather than through specific mass measurements:

$$PV = nRT \tag{B.1}$$

From the ideal gas law, if two gasses fill the same system volume at the same (partial) pressure, the system, at the same temperature, should contain an equal number of moles for both gasses. The assumption that both gasses occupy the same volume can be made as both gasses are miscible [114], and will both occupy the same free space in the system (where water is not) to form a single, uniform phase. Several factors could act to segregate the gases once in the core such as diffusivity, dispersion, gravitational effects/density differences, and improper/insufficient equilibration time. In regards to these points, research conducted at the molecular level shows that the impact of gravity segregation of H_2 and CH_4 in a UHS reservoir is insignificant [115], so they can be expected to continue acting as one gaseous phase. Furthermore, due to the negative charges on H atoms in H_2 and positive charges on CH_4, a shorter intermolecular distance and a larger binding energy (14 mev) compared to interactions between H_2 molecules (6mev) form between H_2 and CH_4 molecules, further indicating that H_2/CH_4 mixtures tend to coalesce rather than separate. Furthermore, diffusion, driven by concentration gradients in the mixture, will tend to re-equilibrate the mixture, which would counteract gravity segregation, helping to maintain a more homogeneous mixture [115]. Factors such as solubility, and adsorption would likely be more impactful. Solubility of both H_2 and CH_4 are similar under the specified conditions (Table 2.4), and literature has suggested that the effect of their slightly differing solubility will be negligible on gas composition [55]. However, it must be mentioned that several studies have shown that hydrogen dissolution can effect flow at the pore scale, leading to diverse flow behavior [105] [24]. In the core scale study of Boon et al. [24], hydrogen dissolution in water together with gravity segregation resulted in the formation of a preferential channel for the water phase along the bottom of the core. Consequently, a large proportion of hydrogen was trapped in their core. Despite extensively pre - equilibrating the brine, before injection in the core, gas dissolution still occurred, as evidence by the formation of viscous fingers. Similarly, Gao et al. [81] observed that dissolution will occur even in brine extensively saturated with gas when displacing hydrogen. The behavior is explained through ripening dynamics, where differences between bulk pressure of the fluid and the pore scale capillary pressure, result in the pre-equilibrated brine being under saturated compared to the pore pressure of the gas. Moreover, as the gas bubble dissolves, it shrinks, increasing the capillary pressure on the gas bubble, leading to a greater rate of dissolution. Mirchi et al [116] investigated the adsorption of H_2 and its 80 - 20% H_2 - CH_4 mixture in water wet sandstones. They found that hydrogen and the H_2 -CH_4 mixture adsorption on their sandstone sample under similar conditions (25 C, 100 bar) was very small, on the order of 10^1 cm^3/m. Considering the total core volume in this study, the maximum adsorption would be 0.01 ml - 0.1 ml for H_2 and CH_4 . This is a negligible amount. Furthermore, studies indicate that the level of hydrogen and

methane adsorption only becomes significant with high organic content in the porous medium [117]. Consequently, the ideal gas law may well provide a valid means to determine the gas composition given the negligible effects of the previously mentioned parameters to alter the mixture composition during the experiment.

C

Capillary pressure core regions

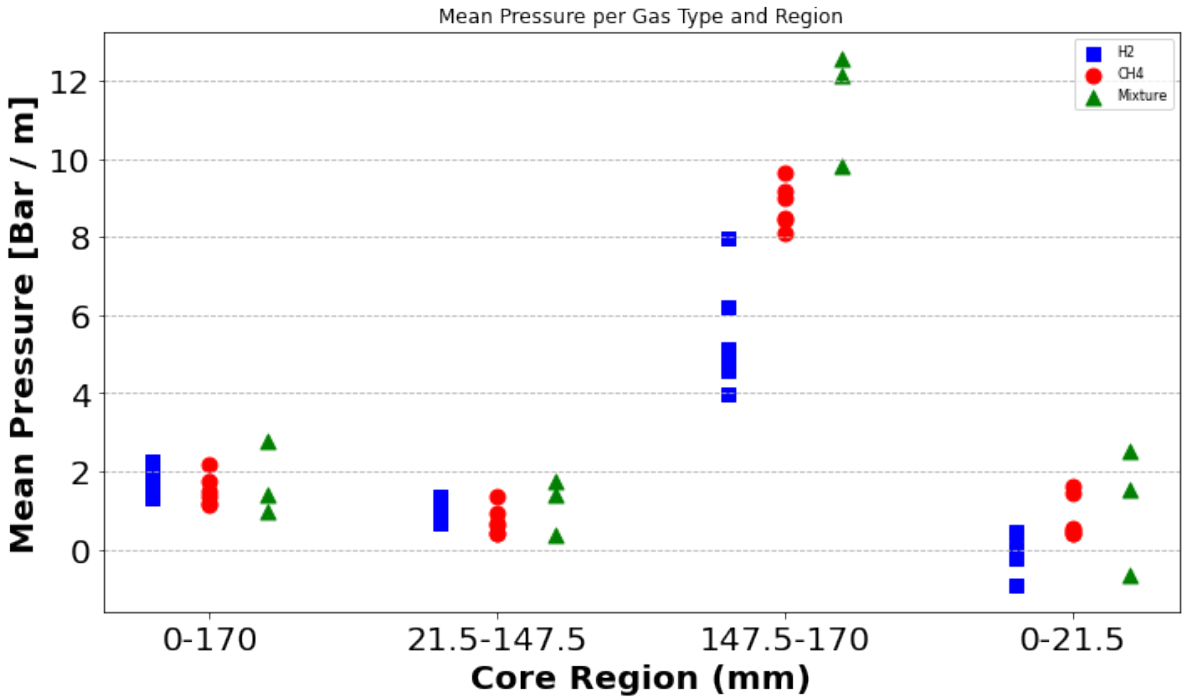

Figure C.1: Mean pressure drop per meter per gas type, across the core length (0 - 170 mm)

Figures C.1 and C.2 show the pressure drop per meter across the core regions in different areas of the core. Clearly the outlet region (147.5 - 170 mm) has a much higher pressure drop per unit length than any other region in the core. This is attributed to end effects, where water accumulates at the outlet of the core. These effects , visible in the saturation profiles for each gas towards the outlet of the core, are unrepresentative of the pressure drop in the core, hence can lead to errors in the calculated relative permeability, capillary pressure, and saturation values. For this reason the pressure drop measured for DP5 (the differential pressure transducer at the region 147.5 - 170 mm) is not considers. The capillary pressure of the outlet region was calculated by subtracting DP3, DP4 and P2 from P1, which had more representative pressure drops.

Capillary pressures at 21.5 mm are similar to those at the outlet (147.5 mm) when calculated this way (see FigureC.2). supporting the accuracy of the capillary pressure calculation.

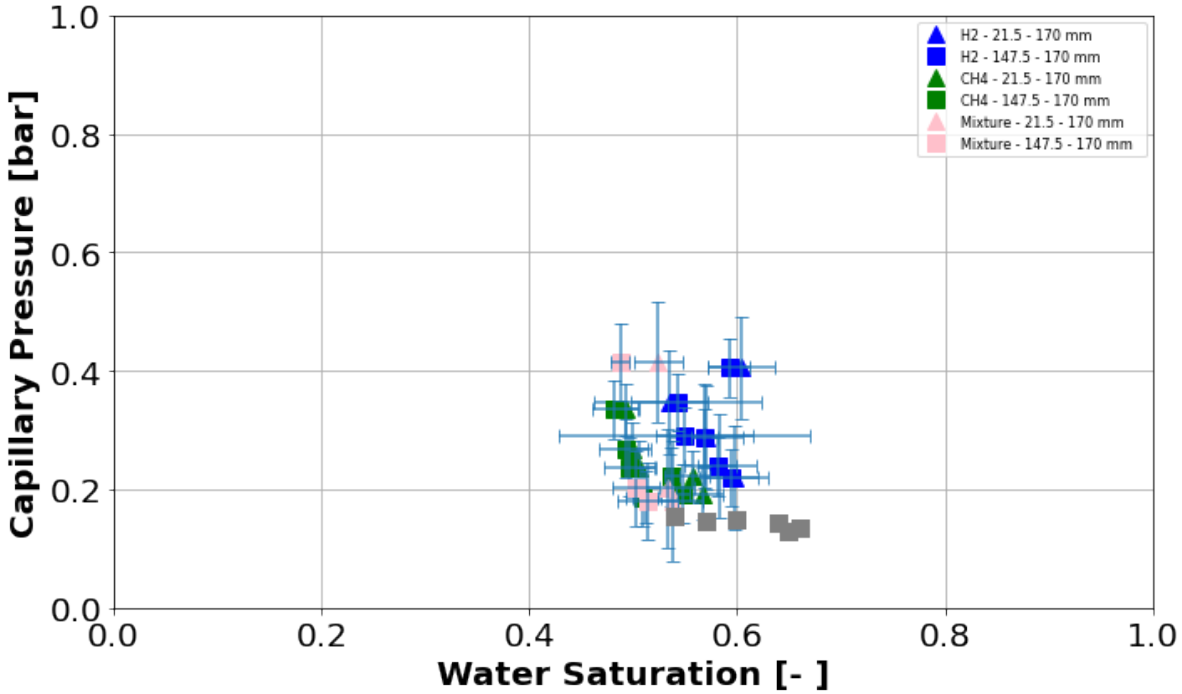

Figure C.2: Capillary pressures at 21.5 mm and at 147.5 mm of core

D

Pressure drop comparisons

f_{H_2}	ΔP (bar)		
	Rademaker et al. [13]	Boon et al. [24]	This study
0	–	–	–
0.2	–	0.61560	2.17
0.3	12.1	0.60210	1.96
0.4	–	0.62850	11.3
0.5	10.4	0.64750	11.4
0.7	7.04	0.60110	8.11
0.8	–	0.47820	6.10
0.9	1.04	0.42270	2.90
0.95	–	0.28020	1.66
0.99	–	0.28480	0.638
1	0.36	0.22750	0.385

Table D.1: Drainage relative permeability experiment pressure drop in hydrogen experiment between Boon et al. [24], Rademaker et al. [13] and this study. f_{H_2} is hydrogen fractional flow rate.